Antennas With Adaptively Varying Impedance Matching

Von der Fakultät Informatik, Elektrotechnik und Informationstechnik der Universität Stuttgart zur Erlangung der Würde eines Doktor-Ingenieurs (Dr.-Ing.) genehmigte Abhandlung

Vorgelegt von

Serafin Benedikt Fischer-Kennedy

aus Buchholz in der Nordheide

Hauptberichter:	Prof. Dr. sc. techn. Jan Hesselbarth
Mitberichter:	Prof. Dr.-Ing. habil. Stefan Lindenmeier
Tag der mündlichen Prüfung:	13 November 2023

Institut für Hochfrequenztechnik der Universität Stuttgart

2023

Danksagung

Zusammenfassung

In den letzten Jahren ist die Anzahl der drahtlosen Sensoren und Sender zur Identifikation, sogenannte *radio-frequency identification (RFID) tags* enorm gestiegen. Gewöhnlich kommunizieren diese Einheiten über eine Antenne mit einem Empfänger, um die gesammelten Sensordaten bzw. Identifikationsdaten zu übermitteln. Der Reifendrucksensor im Auto, der Beschleunigungssensor in einem Laufschuh und der *RFID tag* auf irgendeinem Objekt sind Beispiele dafür. Oftmals sind diese Einheiten in ihrem Leben unterschiedlichen Umgebungen ausgesetzt, was die Eigenschaften der Antenne, wie z.B. Impedanzanpassung, Abstrahlcharakteristik, Polarisation und Effizienz ändert und verschlechtern kann. Folglich wird auch dadurch die Performance des ganzen Übertragungssystem beeinflusst.

In dieser Arbeit werden vier Antennenkonzepte vorgestellt, die es erlauben Antennen so zu entwerfen, dass diese adaptiv bezüglich der Impedanzanpassung auf die Umgebungsänderung reagieren. Zwei von diesen Ansätzen sind rein passiv, also ohne aktive Schaltkomponenten, während die anderen zwei aktiv sind.

Das Prinzip des ersten, passiven Ansatzes ist es verschiedene Antennenstrukturen, die jede für sich für eine spezielle Umgebung optimal ist, zu einer Gesamtstruktur zusammenzufügen. Diese Gesamtstruktur kann dann mehrere Szenarien abdecken. In dem vorliegenden Beispiel wird eine koplanare Patchantenne mit einer Schlitzantenne kombiniert. Dabei deckt der Patchantennenanteil den Fall ab, wenn die Gesamtstruktur einer Metalloberfläche sehr nahekommt und der Schlitzantennenanteil, wenn diese im Freiraum platziert wird. Es zeigt sich, dass beide Fälle gut abgedeckt werden können und auch der Übergang zwischen diesen. Dies bedeutet, dass die Antenne gute Impedanzanpassung zu jedem Abstand größer als $4\,\mathrm{mm}$ zu einer Metalloberfläche aufweist. Dabei beträgt der Wert des gemessenen Reflexionskoeffizients bei der Arbeitsfrequenz von $4.85\,\mathrm{GHz}$ im schlechtesten Fall $-12\,\mathrm{dB}$.

vi

Das zweite, passive Konzept ist ein Leistungsteilernetzwerk, welches zwei Speisepunktimpedanzen einer dual gespeisten Antenne zu einer konstanten Quelle derart transformiert, dass für zwei unterschiedliche Umgebungen (Änderung der Speisepunktimpedanzen) die Antenne am Eingang des Netzwerks angepasst bleibt. Analytische Formeln werden hierfür hergeleitet und mit einem Prototyp verifiziert. Dieser besteht aus zwei unterschiedlich langen Monopolantennen, die sehr nahe, also stark gekoppelt zueinander platziert sind. Beide Monopole werden durch das Netzwerk zu einer Quelle verbunden. Messungen bei der Entwurfsfrequenz von $1\,\text{GHz}$ des Reflexionsfaktors zeigen, dass die Monopole im Freiraum als auch komplett eingetaucht in Butter perfekt (Wert kleiner als $-25\,\text{dB}$) zur Quelle angepasst sind.

Das dritte, aktive Konzept ist eine Antenne, deren Speisung örtlich variiert. Die Idee ist, dass mit Schaltern jener Speiseort ausgewählt wird, an dem die Antenne für eine bestimmte Umgebung Impedanzanpassung zur Quelle aufweist. So kann durch Schaltvorgänge die Antenne für verschiedene Szenarien adaptiv reagieren. Dieses Konzept wird auf eine differentielle dipolartige Antenne in hochflexibler Polymerfolie angewendet, die mit drei möglichen Speisepunkte drei verschiedene Szenarien abdecken kann. Dabei ist das erste Szenario der Freiraum, das zweite, wenn die Antenne auf Butter und das dritte, wenn auf Fleisch platziert wird. Messungen des Reflexionskoeffizient für all drei Szenarien an den entsprechenden Speisepunkten bei $5.5\,\text{GHz}$ zeigen gute Anpassung (Werte kleiner als $-20\,\text{dB}$). In einem weiteren Schritt wird diese Antenne mit einem HF-Chip verbunden, in dem auch die Schaltfunktionalität implementiert ist. Strahlungsdiagrammmessungen von HF-Chip mit Antenne für die Fälle; Butter und Fleisch werden in einer Antennenmesskammer ermittelt und zeigen die Funktionalität dieses Systems.

Der vierte, aktive Ansatz ist eine Theorie, in der die Antenne durch ein Mehrtor repräsentiert ist. Dabei können einige Tore zur simultanen Speisung verwendet werden, während jeweils die anderen mit einer Lastadmittanz abgeschlossen sind. Diese Theorie erlaubt es alle Werte für die Admittanzen an den Lasttoren zu bestimmen, sodass an den Speisetoren Impedanzanpassung herrscht. Durch geschicktes Schalten

können an verschiedenen Orten Lastadmittanzen aktiviert und oder deaktiviert werden. Sind nun für ein bestimmte Umgebungen einige Lastadmittanzen aktiv können diese deaktiviert und andere für ein andere Umgebung aktiviert werden, sodass stets an den Speisetoren Anpassung gewährleistet wird. Einige Beispiele werden präsentiert, um die Anwendung und Verifikation dieser Theorie zu demonstrieren.

ix

Abstract

In recent years the number of wireless sensors and radio-frequency identification (RFID) tags has increased tremendously. These devices communicate via an antenna with a receiver in order to provide their data. Examples are the tire pressure sensor in a car, the accelerometer of a running shoe, and an RFID tag on any object. These devices are oftentimes exposed to different environments, which change the antenna properties, like impedance matching, radiation characteristic, polarization, and efficiency. As a result, the overall performance of the whole wireless transmission system is degraded.

In this thesis, four antenna concepts are presented that allow antennas to be designed in such a way that they react adaptively to changes in the environment with regard to impedance matching. Two of these approaches are purely passive, i.e. without active switching components, while the other two are active.

The principle of the first, passive approach is to combine different antennas into a single structure. The antennas that are to be combined each cover a special environment, so that the merged structure reacts adaptively to all of them. In the present example, a coplanar patch antenna is combined with a slot antenna. The patch antenna part covers the case when the merged structure comes very close to a metal surface and the slot antenna part when it is placed in free space. It turns out that both cases can be covered well and also the transition between them. This means that the antenna has good impedance matching at any distance greater than $4\,\mathrm{mm}$ from a metal surface. In the worst case, the measured reflection coefficient shows a value of - 12 dB at the working frequency of $4.85\,\mathrm{GHz}$.

The second, passive concept is a power divider network, which transforms two feed point impedances of a dual-fed antenna to a constant source in such a way that the antenna at the input of the network remains matched for two different environments (change in the feed point impedances). Analytical formulae are derived for this and verified with a prototype. This consists of two monopole antennas of different lengths,

x

which are placed very close to each other, i.e. strongly coupled to each other. Both monopoles are connected to one source by the network. Measurements at the design frequency of $1\,\text{GHz}$ of the reflection coefficient show that the monopoles in free space as well as completely immersed in butter are perfectly (value less than - 25 dB) matched to the source.

The third, active concept is an antenna whose feed varies locally. The idea is that switches are used to select the feed location where the antenna is impedance matched to the source for a specific environment. In this way, the antenna can react adaptively to different scenarios through switching operations. This concept is applied to a differential dipole-like antenna in a highly flexible polymer foil, which can cover three different scenarios with three possible feed points. The first scenario is free space, the second is when the antenna is placed on butter, and the third is when it is placed on meat. Measurements of the reflection coefficient for all three scenarios at the corresponding feed points at $5.5\,\text{GHz}$ show good matching (values less than - 20 dB). In a further step, this antenna is connected to an RF-chip, in which the switching functionality is implemented. This system is then placed in an anechoic chamber, firstly, on butter and, secondly, on meat and its radiation patterns are measured. These show good functionality.

The fourth, active approach is a theory in which the antenna is represented by a multiport. In this case, some ports can be used for simultaneous feeding, while the others are each terminated with a load admittance. This theory makes it possible to determine all values for the admittances at the load ports, so that there is impedance matching at the feed ports. Load admittances can be activated and/or deactivated at different locations by clever switching. If some load admittances are now active for a certain environment, these can be deactivated and others can be activated for another environment, so that adaptation is always ensured at the feed ports. Some examples are presented to demonstrate the application and verification of this theory.

Contents

List of Figures

List of Tables

List of Abbreviations

1G	First Generation
2G	Second Generation
3G	Third Generation
4G	Fourth Generation
5G	Fifth Generation
BLE	Bluetooth Low Eenergy
DC	Direct Current
CAD	Computer-Aided Design
CR	Cognitive Radio
EBG	Electromagnetic Band Gap
EMMPS	ElectroMagnetic Multi Port System
ETSI	European Telecommunications Standards Institute
HIM	High Impedance Model
IMPM	Internal Multi Ports Method
IoT	Internet of Things
ITN	Impedance Transformation Network
LAN	Local Area Network
LoRaWAN	Long Range Wide Area Network
LPWAN	Low Power Wide Area Network
MAN	Metropolitan Area Network
MEMS	Micro Electro Mechanical Systems
MIM	Middle Impedance Model
MIMO	Multiple Iinput Multiple Output
MTL	Microstrip Transmission Line
NB-IoT	NarrowBand Internet of Things

NFC	Near Field **Communication**
PC	**P**ersonal **C**omputer
PCB	**P**rinted **C**ircuit **B**oard
PDN	**P**ower **D**ivider **N**etwork
PEC	**P**erfect **E**lectric **C**onductor
PIFA	**P**lanar **I**nverted **F** **A**ntenna
RF	**R**adio **F**requency
RFID	**R**adio **F**requency **ID**entification
SMD	**S**urface-**M**ounted **D**evice
TL	**T**ransmission **L**ine
TPMS	**T**ire **P**ressure **M**onitoring **S**ystem
UWB	**U**ltra **W**ide**b**and
VSWR	**V**oltage **S**tanding **W**ave **R**atio
WBAN	**W**ireless **B**ody **A**rea **N**etwork
WiFi	**W**ireless **Fi**delity
WiMAX	**W**orldwide **I**nteroperability for **M**icrowave **A**ccess
WRAN	**W**ireless **R**egional **A**rea **N**etwork
WirelessHART	**W**ireless **H**ighway **A**ddressable **R**emote **T**ransducer **P**rotocol
WLAN	**W**ireless **L**ocal **A**rea **N**etwork
WMAN	**W**ireless **M**etropolitan **A**rea **N**etwork
WPAN	**W**ireless **P**ersonal **A**rea **N**etwork
WWAN	**W**ireless **W**ide **A**rea **N**etwork

Chapter 1

Introduction

1.1 Motivation

Over the years, the mobile network has increased its capability significantly. While everything started with analogue voice calls in the first generation (1G) of the mobile network, we now find ourselves in the transition between the fourth (4G) and the fifth generation (5G). The 4G network works with frequency bandwidths in the low megahertz range, whereas the 5G network promises frequency bandwidths in the gigahertz range, enabling multi-gigabit peak data rates. This is made possible by using millimeter wavelengths. Not only the data rates but also other network properties like latency, reliability, and capacity are about to be enhanced tremendously. The goal to ensure an ultra-high density network with deep coverage enables the internet of things (IoT). This term describes what is meant very well. "Things" refers to the physical world and can be anything in it. "Internet" represents unlimited connectivity, meaning connection from any place at any time. As a result, a networked world is imagined that is intended to make everyday life easier. While recent active device connections, called non-IoT (including mobile phones, tablets, laptops, and PCs) are predicted to experience only a small growth, IoT active connections are expected to expand considerably as shown in Fig. 1.1. IoT active connections are, for example, consumer devices, connected cars, smart home devices, and connected industrial equipment.

In Fig. 1.2 the architectural overview of 5G IoT is depicted. The "physical" world is represented by smart sensors and devices in the sensor layer. All these communicate to the network layer, which itself communicates to the communication layer. The

Internet of Things (IoT) and non-IoT active device connections worldwide from 2010 to 2025
(in billions)
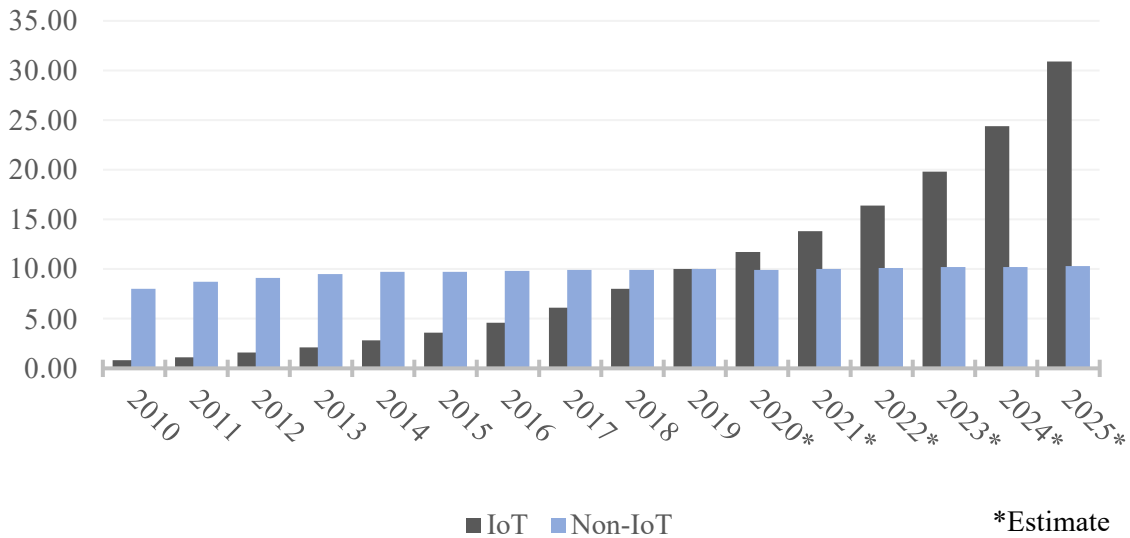
FIGURE 1.1: Internet of Things (IoT) and non-IoT active device connections worldwide
from 2010 to 2025 in billions [1].

communication layer "can be considered as the backbone of the IoT architecture because
it transfers the whole information within the layers", whereby the architecture layer is
"[...] the framework of IoT, where architectures, such as cloud computing and big data
analytics, are considered" [2]. Finally, the application layer maps all IoT application
areas, such as smart home, smart factories, smart cities, smart health, and many more.

All the wireless communications technologies for the IoT are implemented in the
network layer. In Fig. 1.3 these technologies are shown. The wider the ovals, the wider
a range can be covered. An example is near-field communication for cashless payments,
such as with a credit card. Even reading a radio frequency identification (RFID) tag,
e.g. on a packet, only requires a small distance. However, a smart watch requires
a connection to the smartphone over several meters and with sufficient bandwidth.
Bluetooth can be used in this case. This is very important for sensors that are not
easily rechargeable, such as in cars (e.g. tire-pressure monitoring system(TPMS)) and
in smart homes (e.g. coffee machine, heater, air-conditioner, alarm-system, etc.).
For smart factories (e.g. plant control), technologies for low power applications, like
Bluetooth Low Energy (BLE), ZigBee and Z-Wave are also suitable. As well, for mid-
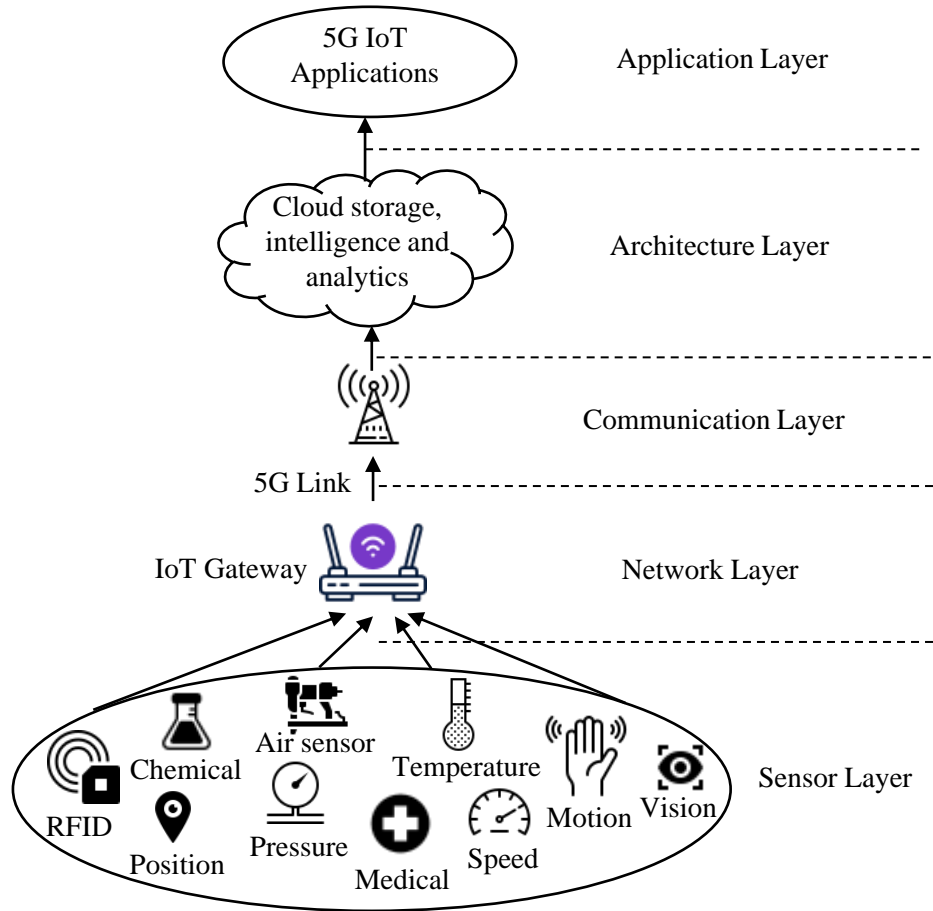
FIGURE 1.2: Overview of the 5G IoT architecture, adapted from [2].

and wide-range applications, a huge amount of technology exists that emphasizes the enormous potential of the IoT, not least because a communication technology that fits for the "thing" can always be found.

This thesis deals with the physical communication between the sensor and the network layer on the sensor layer side. To be more precise, it addresses the antenna structures which are subject to special requirements due to the diverse range of applications. While the receiver, i.e. the IoT gateway of the network layer, is positioned in a well-defined environment, the sensor (or IoT device) is exposed to different environments. Such a change has a significant impact on the antenna. Its performance in terms of radiation characteristic, impedance matching, and efficiency is strongly dependent on the surrounding materials, which have different dielectric and conductive properties. This fact opens up a new discipline in antenna technology, namely the design of
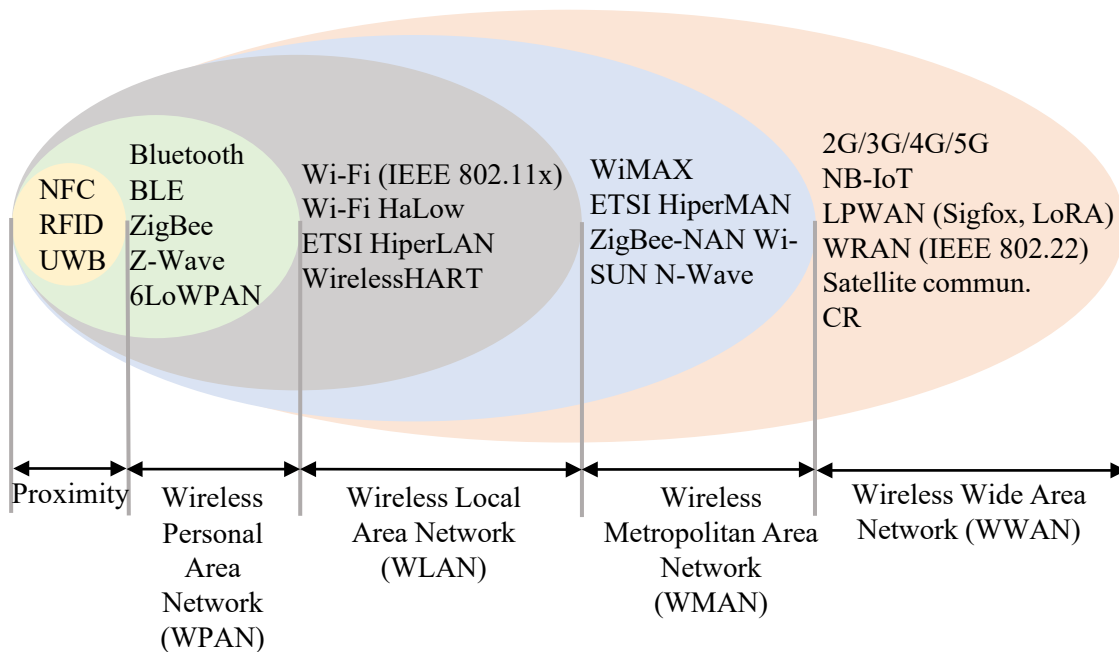
FIGURE 1.3: Wireless communication technologies for Internet of Things, adapted from [3].

antennas that can react adaptively to their environment so that system operation can be maintained even if the environment changes. Such antennas are the subject of the present work.

1.2 Outline

The first chapter contains the introduction to this work, in which the possible fields of application are presented.

Chapter 2 gives a comprehensive overview of the state of the art. The first section addresses the challenges arising when an antenna is exposed to different environments, while the second section presents approaches to overcome them. Here, the concepts presented in this thesis are put into this context.

Two main threads to make an antenna adaptive to a changing environment are presented in Chapter 3 and 4. In Chapter 3, two fully passive approaches are introduced. These concepts do not require active components such as diodes or transistors, contrary to the two approaches presented in Chapter 4.

The fifth and last Chapter consists of a conclusion and a short outlook.

Chapter 2

State Of The Art

This chapter contains two sections. In the first section, the challenges and their preliminary investigations are presented, while the second section introduces approaches from the research community that have the potential to address these challenges.

2.1 Challenges

As presented in Chapter 1, this work deals with antennas that can be used under different environmental conditions. In other words, these antennas should respond adaptively to different environments and ensure proper operation at all time. In order to identify possible approaches, it is necessary to consider the effects on the antenna caused by changes in the environment. Following effects are taken into account:

- Change of antenna input impedance

- Change of antenna radiation pattern

- Change of antenna polarization

- Change of antenna efficiency

Basically, every device with wireless data transmission capability comprises an antenna with a chip connected to it. This chip is a constant source from the point of view of the antenna, therefore impedance variation causes mismatch between chip and antenna. This, in turn, reduces system performance significantly. A change of radiation characteristics, polarization, and deterioration of the antenna efficiency can reduce
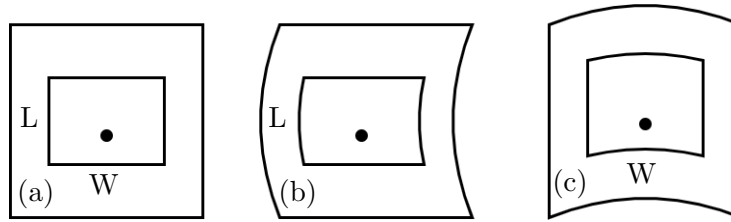
FIGURE 2.1: A patch antenna (a), that is bent along the length (b) and along the width (c). The black dot indicates a possible coaxial feed from the backside.

system performance as well. Now that the effects on the antenna have been highlighted, it is interesting to look at what causes them. Effects on the antenna caused by:

- Bending

- Stretching

- Surrounding materials

- Close proximity to metal surface

have been widely explored. The first two points are mostly studied in conjunction with textile antennas, since these antennas are usually made of highly flexible and stretchable materials, while points three and four are frequently investigated within the area of RFID.

Bending: Various types of antennas under bending stress have been investigated in the literature. Conventional patch antennas usually assume two different bending directions, one lengthwise and the other widthwise, as shown in Fig. 2.1. The degree of bending is indicated by the bending radius, which is the radius of a fictitious cylinder on which the antenna is placed. Consequently, the smaller the radius the more the antenna is bent. When the radius approaches infinity, the antenna is flat. In [4–10] the effects on a patch antenna when bent is studied. Most of these works show that the resonant frequency changes significantly more when bent along the length than along the width. While the 3-dB beamwidth increases with decreasing bending radius the gain decreases. In order to have a quantitative example, the work of Song *et al.* in [5] is used, whose results can be classified well with those of the other works. In Fig. 2.2, the normalized frequency shift due to bending along the length (E-plane) of the patch
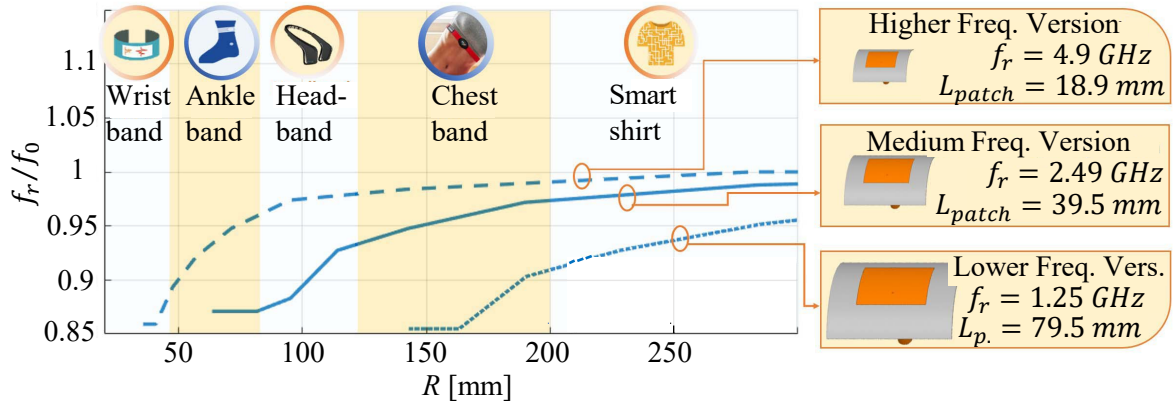
FIGURE 2.2: Normalized frequency shift with respect to bending radius R, targeting at various potential wearable applications, adapted from [5].

antenna with its wearable applications is shown. For the medium frequency version of the presented patch antenna, the normalized (normalized to the resonant frequency in flat-condition) frequency shift is about 0.87 at the minimum bending radius of about $0.5\lambda_0$ (60 mm), where λ_0 is the free-space wavelength at the resonant frequency. At this very same bending radius, the measured 3-dB beamwidth (in E-plane) is about $72°$ and the cross-polarisation about -9.7 dB, while in flat-condition the 3-dB beamwidth is $55°$ and the cross-polarisation about -42.1 dB.

Other studies deal with the behavior of monopole and dipole antennas under bending stress. It is intuitively clear that bending along the length of the mono- or dipole has more impact than in the case of bending along the width, not least because the structure expansion widthwise is negligibly small in comparison to lengthwise. In [11] a resonant frequency shift from 2.5 GHz for flat operation to 2.8 GHz when the two dipole arms are $90°$ to each other is reported. For the same angle, the radiation pattern in the E-plane shifts about $45°$ if compared to the radiation pattern of the straight dipole, while the maximum normalized radiated power is reduced by 2 dB. Another study [12] on a bent dipole concludes: "*Generally, a decrease in impedance and maximum gain happened when an increase in bend angle was implemented.*". A wideband planar monopole under bending conditions is investigated in [13], showing an impedance variation. This variation leads to a notable impedance mismatch. As well, more directive antennas like a planar two-dipole antenna [14] (two dipoles in parallel, fed simultaneously), or a Yagi-Uda antenna [15] are subjects of investigation. In these cases also bending along

the axis perpendicular to the dipole has a huge impact on the directivity. With the two-dipole antenna, the maximum gain drops from $7\,\mathrm{dBi}$ to $5.1\,\mathrm{dBi}$ at $28\,\mathrm{GHz}$ when the antenna is bent the most. The performance behaviour of a transmitting system, such as in RFID, when the tag with a dipole antenna is bent, is also interesting. In [16] it is shown that in the worst case (two dipole arms are perpendicular to each other), the performance of the RFID system degrades by around $37\,\%$. A reduction of the read range of a RFID system by $9.7\,\%$ (concave) and $7.3\,\%$ (convex) respectively, is reported in [17]. Some other works on differently-bent antennas such as a split ring based implanted antenna [18], a co-planar antenna [19], and a split-ring, and bar slotted antenna [20] have been published .

Stretching: The elasticity of an antenna is strongly dependent on the material. Every material will break at a certain elongation strain and change its behaviour during multiple stretching events. For an ordinary antenna, stretching leads to damage, which is the reason why stretching effects are considered for antennas that use special ductile materials. Most of these antennas comprise a substrate and a conductive radiating structure. While there are many stretchable materials available for the substrates, it is difficult to find stretchable ones that are good conductors, in particular because the conductivity significantly determines the antenna efficiency. In most approaches, liquid metals (such as an alloy, composed of gallium, indium, and tin, known as Galinstan), conductive ink, or nanomaterials (e.g., graphite) are used. Structural approaches like conductive fabrics, serpentine, and meandered patterns are also found. The performance of antennas in terms of input impedance, resonant frequency, directivity, and polarization is always determined by their geometries. If the geometry changes, which is the case for stretching, it is obvious that all these parameters will alter as well. In Fig. 2.3 the resonance frequency of a dipole antenna as a function of the tensile strain is depicted.

It is interesting to know how the antenna efficiency changes when the antenna is stretched. In [22] the efficiency of a patch antenna made out of Galinstan decreases with stretching from $80\,\%$ to $66\,\%$ for $100\,\%$ stretching. Another work [23] describes a meandered patch out of flexible copper tapes on a polyimide substrate. This patch changes its resonant frequency by about $0.9\,\%$ when a $0.09\,\%$ strain is applied. A strain
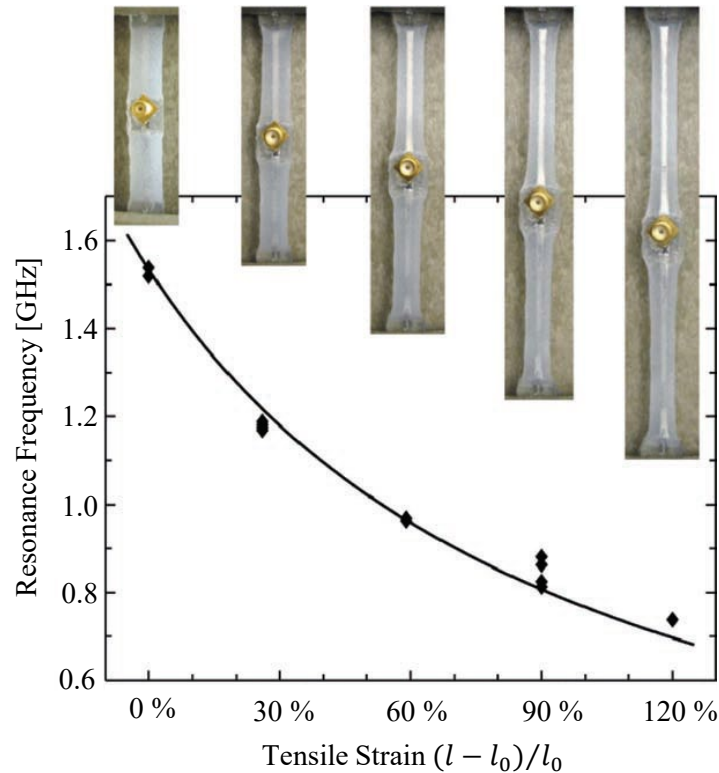
FIGURE 2.3: The resonance frequency of the antenna as a function of the tensile strain. The antenna was stretched from l_0 (non-stretched length) to $l = 2.20l_0$. Measurement under each value of strain was repeated five times; and the data points are shown as individual diamonds (♦) in the plot, adapted from [21].

over $0.09\,\%$ leads to cohesive or adhesive failure of copper tape. Other works such as [24, 25] have also examined patch antennas under tensile stress. Differential and dipole-like antennas have also been widely studied [26, 27] since these are often deployed in RFID tags and in applications such as in wireless body area networks (WBAN). Conductive fabric dipoles for RFID tags and system performance under recurrent stretching is studied in [28–30]. It is shown that the read range does not notably decrease when the antenna has been stretched fewer than 200 times. An electrical small micromesh antenna is described in [31], which is able to be stretched about $40\,\%$, whereby the gain is decreased due to a slight decrease of effective conductivity. The reduction of gain is also observed in [32], in which a split-ring antenna is used. An overview of stretchable antennas is given in [33] and [34].

Surrounding materials: In the far-field of the antenna, the electromagnetic field, i.e. propagating wave, is fully detached. Consequently, if a material is placed in the

far-field, there are no notable retroactive effects. This is not the case in the near-field of the antenna, since non-radiating field components form in the immediate vicinity and thus in the surrounding materials. A practical example is given in [35], where the losses for handheld phones due to the presence of a human body are investigated. Four factors are mentioned as degrading the transmission performance: absorption in the body, mis-tuning, change of radiation direction, and change of polarization. The absorption in the body shows the greatest degradation, whereas mis-tuning contributes at most to $2\,\mathrm{dB}$. An average absorption (around 40 test persons) for a patch antenna is $3.4\,\mathrm{dB}$ and for a helix antenna $9.7\,\mathrm{dB}$. Relating to that, in [36] the effect of the hand of a mobile phone user on the input impedance of a planar inverted F antenna (PIFA) is studied. Further, the head of a phone user can reduce the antenna (monopole) efficiency from $77\,\%$ to $60\,\%$ in a distance to the head of $3\,\mathrm{cm}$ and $1.5\,\mathrm{cm}$ respectively, as shown in [37]. In [38], environmental effects on RFID tag antennas are studied ([39]). A measured read range as a function of the distance to a plastic water-filled bottle is shown as approaching zero for small distances. For example, if the tag is placed at a distance of around $2\,\mathrm{mm}$, the read range is reduced to less than $10\,\%$ of the read range achieved in an open area. This behavior is understandable because, an antenna placed close to a lossy medium with a high dielectric constant tends to radiate more into that same medium. At the same time, the gain is reduced [40, 41]. An input impedance study of an RFID tag antenna (dipole) placed on a half space material with varying dielectric constant is given in [42]. A large change in the input impedance changes the resonant frequency from $915\,\mathrm{MHz}$ with a dielectric constant of 1 to $680\,\mathrm{MHz}$ with a dielectric constant of 10. Antenna and RFID tag performances on other materials like paper, cardboard, and clothes [43], or on an acrylic slab, pine plywood, ground beef, and ethylene glycol [44] are investigated. As well, the impact of dryness, humidity, frozen and half-frozen water [45] , even snow [46] is studied. A more theoretical approach for dielectric-covered microstrip patch antennas is shown in [47–49] and for a printed dipole in [50]. Theoretical investigations on dielectric-covered slot antennas in a waveguide are done by Bailey *et al.* in [51, 52]. In [53], the alteration of the impedance as a function of dielectric constant, dielectric losses and dielectric thickness is given.
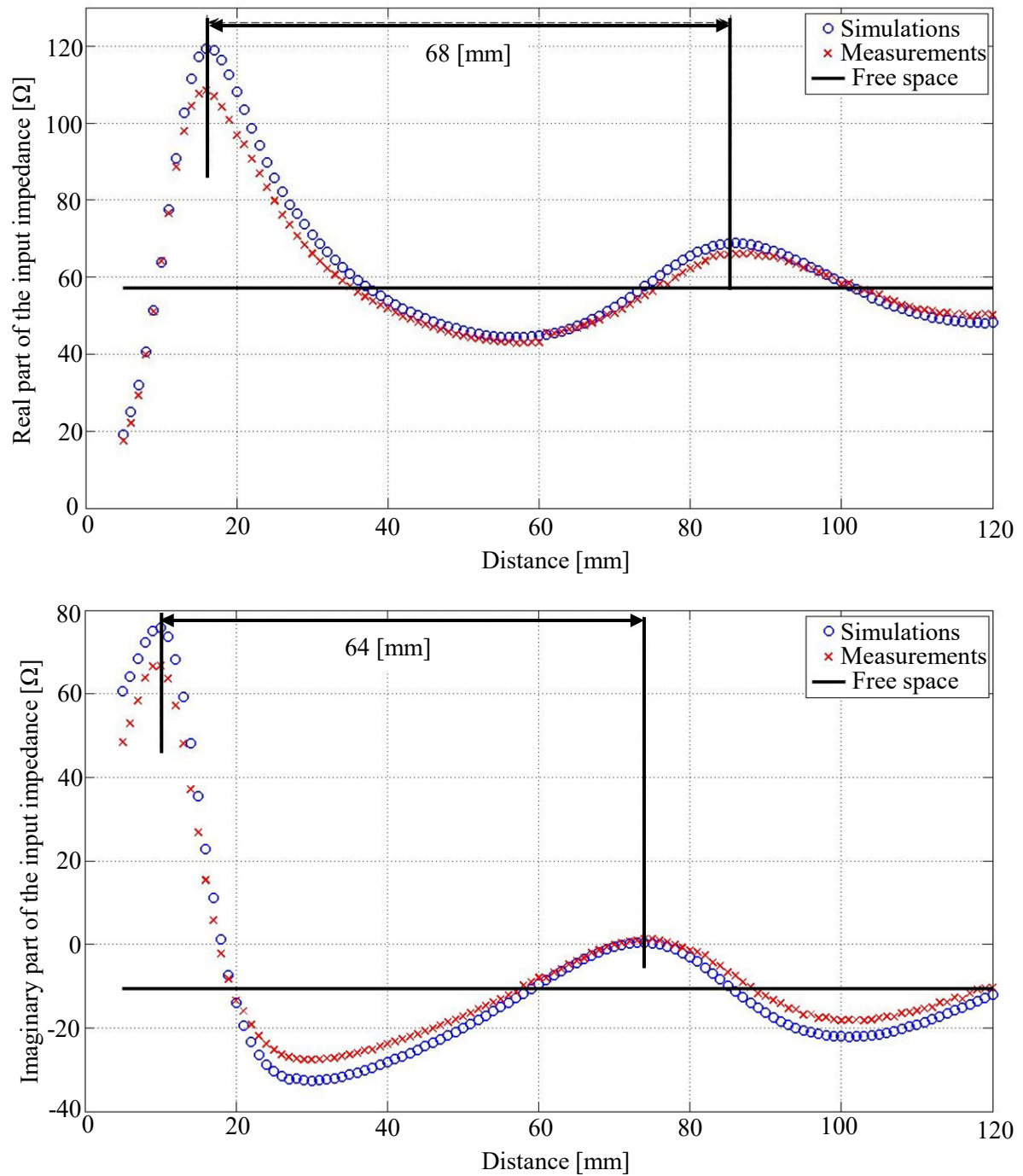
FIGURE 2.4: The simulated and measured input impedance versus the distance between the antenna and the metal plate, adapted from [54]. The upper graph shows the real part and lower on the imaginary part.

Close proximity to metal surface: When a conventional antenna approaches a metal surface, the input impedance starts to change. The closer the antenna gets to the metal surface, the more severe the change becomes. Such behaviour is shown

in the graphs of Fig. 2.4, where the measured real and imaginary part of the input impedance of a PIFA in comparison to the input impedance in free-space is given. The same behaviour for a folded dipole antenna is found in [55–58]. Also, a huge impact on radiation characteristics is reported. In some cases, it might enhance and in some others it worsens the directivity. An example is a dipole. When it is placed a quarter wavelength above a metal plate, the maximum directivity will enhance by a factor of around two. This is reflected in [59, 60], where the measured read ranges of a closed loop and meandered RFID antenna as a function of the distance is investigated. For short distances, the read range approaches zero, while for the distance of around a quarter wavelength, the read range is much larger (around $8\,\mathrm{m}$) than the free space read range (around $6\,\mathrm{m}$). In the previous considerations, the metal surface is parallel to the antenna, which is the constellation in which the antenna suffers the most, as shown in [61, 62] for a slot and a loop antenna.

2.2   Approaches

In the previous subsection, studies of the effects on the performance of different antennas due to bending, stretching, and changing environments were briefly described. This subsection will present research activities on how to reduce, avoid, or compensate for such effects. Two approaches are distinguished: passive and active. The passive approach simply means that contrary to the active approach, the antenna does not use any active components, like diodes, switches, or transistors.

Passive Approach: The easiest way to make an antenna robust against bending is to reduce the size of the antenna. The bending angle is given as the ratio between the antenna dimension (length or width) and the bending radius, which is the radius of an imaginary cylinder on which the antenna is placed. For one particular scenario, e.g. when the antenna is placed on the wrist, the bending radius as well as the bending angle are constant, unless the antenna size is reduced. In [63], a wearable antenna with a size of $90 \times 47\,\mathrm{mm}^2$ is reduced to $70 \times 25\,\mathrm{mm}^2$. While for the large antenna the measured frequency shift (bending radius is $55\,\mathrm{mm}$) is $32.5\,\mathrm{MHz}$, for the reduced one it is $7.5\,\mathrm{MHz}$ at a working frequency of around $2.45\,\mathrm{GHz}$. Another straightforward
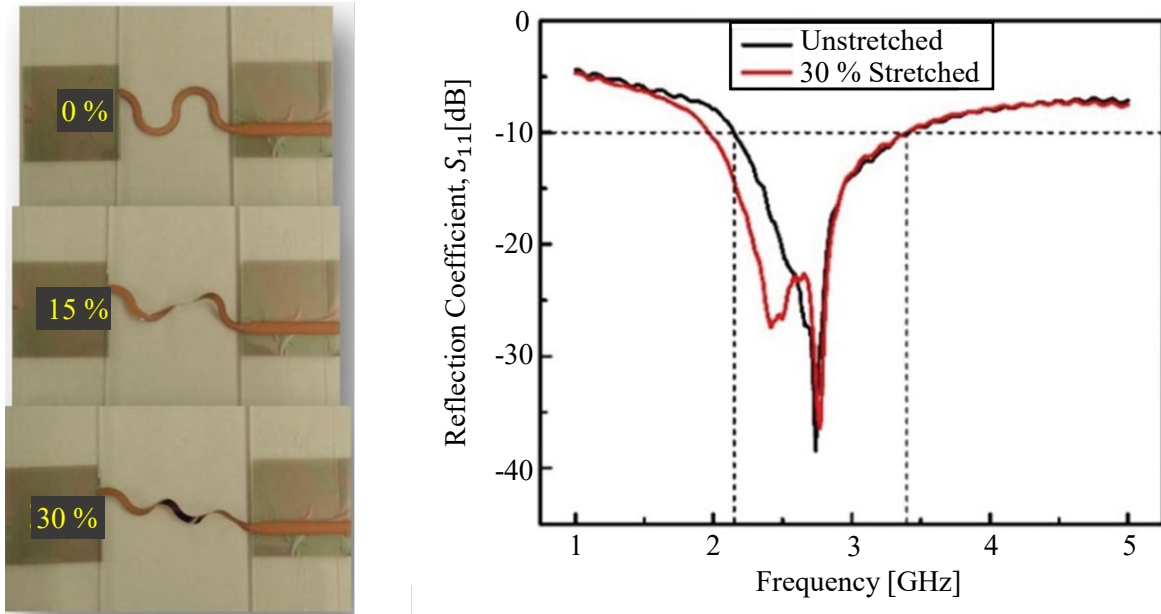
FIGURE 2.5: A monopole that ensures good operation during stretching (adapted from [66]). The left photographs show different states of the stretched monopole and the right graph the reflection coefficients in dB for the unstretched (black curve) case and if the antenna is 30 % stretched (red curve).

approach to having an antenna robust against bending and stretching is to use a wideband antenna. Since the frequency change is limited to a certain extent, the resonance(s) will only change within the operation bandwidth. Examples for such antennas are given in [64] (inverted cone antenna) and [65] (loop antenna). Figure 2.5 shows a semicircular spring as monopole that does not physically change the length, ensuring operation at 2.45 GHz for up to a strain of $30\,\%$.

Other approaches of an antenna design being robust against a changing environment have been discussed. An intuitive method is to use an antenna, which has a ground plane, like ordinary patch antennas, but also flexible textile antennas as in [67]. The idea is that only the ground plane has contact to the changing surrounding material. In this case the size of the ground plane plays a significant role, so that the whole structure might become bulky to ensure good isolation from the surroundings. Quite a similar thought is to bring well-defined materials as a spacer around the antenna to reduce the influence of the changing electromagnetic environment as shown in [46, 68]. In [69], design rules are given for when bio compatible sub- and superstrate are used. For a microstrip antenna the relative permittivity of the sub- and superstrate should be

as large as possible while having low conductivity; they should also be rather thick than thin. For a certain range of materials where the properties do not differ drastically, it is sufficient to use a broadband antenna as given in [70]. In [71], where a cellphone hand-immune metal rim antenna with multiple feeding ports is presented. The idea is to use those characteristic modes of the radiating structures, which are not strongly disrupted by the hand of the user. In addition, the cluster technique is applied to enhance the antenna efficiency by means of reducing the coupling between the ports. This technique is given in [72, 73]. It weights the excitation of a multi-port antenna to enhance the efficiency while ensuring good matching. At this point, reference is made to part of the present work, which is also published in [74] and is presented in more detail in Chapter 3, "Adaptivity by Power Divider Network". A fully passive power divider network design is presented that is connected to a dual-fed antenna. The divider covers two arbitrary scenarios (largely different electromagnetic environments) perfectly, which distinguishes this work from most other works in the literature.

A quite comprehensive study on RFID tags mountable on conductive surfaces is given in [75]. Antenna with ground such as like microstrip patch antennas, planar inverted-F antennas and antennas integrating EBG structures and antenna without ground, like dipole antennas, are considered. The former use the principle to isolate the antenna from the metal surface, while the latter use a certain space to the metallic surface to ensure similar performance. An example is given in [76], where a planar-meandered dipole antenna on a substrate is presented. This antenna is able to work in free space but also on metallic objects. A specific design approach that contains two steps is introduced. Firstly, the antenna is constructed on a large metallic plate. Secondly, the metallic plate is removed and a ground layer is added beneath the substrate, which is the same size as the antenna. Then a slotting technique is used to optimize the performance in air. Another approach for a dipole [77] and a monopole [78] is to use multiple-wires instead of one solid strip. It has been shown that this technique increases the antenna efficiency close-by a metal surface and makes the antenna more robust in terms of impedance variation. Another interesting work is presented in [79], in which a U-shaped folded monopole antenna is used. This antenna is made resilient against a metal-plate by using a higher input impedance
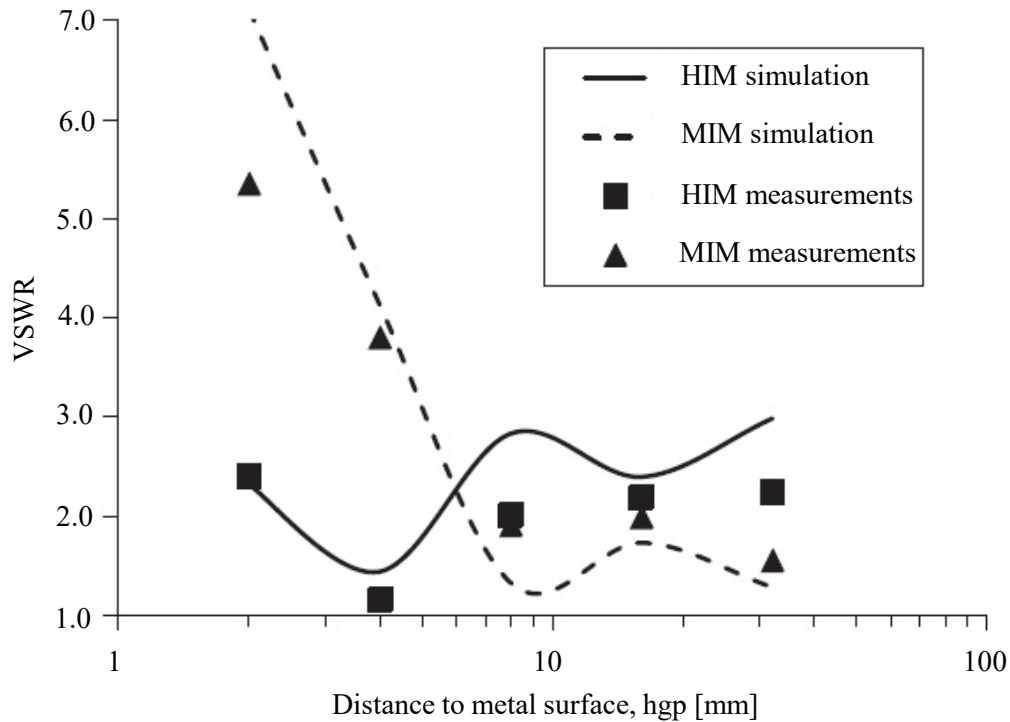
FIGURE 2.6: The voltage standing wave ratio (VSWR) at $2.4\,\text{GHz}$ of an U-shaped folded monopole antenna as a function of the distance (hgp) to a metal surface, adapted from [79]. A comparison of the middle impedance model (MIM) and the high impedance model (HIM) is shown.

TABLE 2.1: Comparison of this work with another work, both covering the same scenarios. Firstly, when the antenna is placed in air, and secondly, when placed close to a metallic surface.

closest point to metal	matching	frequency	work
0, but two layers	$< -8\,\text{dB}$	$867\,\text{MHz}$	[76]
$\approx 0.065\lambda$	$< -12\,\text{dB}$	$4.85\,\text{GHz}$	this work [80]

of the antenna (instead of $37\,\Omega$, $126\,\Omega$ is used). Figure 2.6 shows the voltage standing wave ratio (VSWR) at $2.4\,\text{GHz}$ as a function of the distance (hgp) to a metal surface. A comparison of the middle impedance model (MIM) and the high impedance model (HIM) is shown. The small change in the VSWR of the HIM compared to the MIM is evident. Note that the bandwidth of the HIM is narrower than in the case of the MIM. A part of the present work, Chapter 3, "Inherent Adaptivity by Geometric Modelling" [80] deals with the very same problem. To make the single layer antenna adaptive to the metal surface, two resonant modes are used for the two scenarios (in air and close

to the metal). The mode over the metal is called patch mode and in air, slot mode. Not only the two scenarios (in air and close to the metal), but also all distances to the metal are covered. A comparison with another work is shown in Table 2.1.

Active Approach: Substantial research has been done, in which the radiating elements are manipulated with active circuit components. Most of this are found in the field of reconfigurable antennas. Comprehensive reviews are given in [81–86]. There are various antenna reconfigurations as can be seen in Fig. 2.7. Frequency reconfiguration means that the operating frequency can be changed during operation with components like diodes, micro-electro-mechanical systems (MEMS), but also with materials that change its properties by applying a DC voltage, e.g. graphene. An example application is cognitive radio (CR), where a broad spectrum is observed using a broad band antenna. When the communication device detects an unused frequency band, the antenna is reconfigured in such a way that communication can be established in the very same band. Thus, the spectrum is dynamically exploited, and the frequency bands are used more efficiently. Pattern and polarization reconfiguration alter the radiation and polarization characteristic by using active components, which is useful in multiple input multiple output (MIMO) systems. Finally, all possible combinations between these three reconfigurations are possible. It is conceivable that reconfiguration presents a similar problem as adapting an antenna to external influences. For example, in the former case the technique is used to change the operating frequency, and in the latter case it is used to compensate for the effect on the antenna caused by the change of environment. In either scenario the same strategies can be used.

In Fig. 2.8, an example of a frequency reconfigurable antenna is depicted. An E-shaped patch antenna is used to provide broadband operation. Due to the shape, two resonant modes can be excited, one ordinary patch mode, in which the current flows along the length of the patch and another, where the current flows along the slots. This is reflected in the two resonant frequencies of the blue curve in the graph of Fig. 2.8. To reconfigure the resonant frequency of the antenna, RF-MEMS switches are incorporated in such a way that the current path along the slot reduces its length, resulting in higher resonant frequencies.

In the following, various techniques for antenna reconfiguration are presented
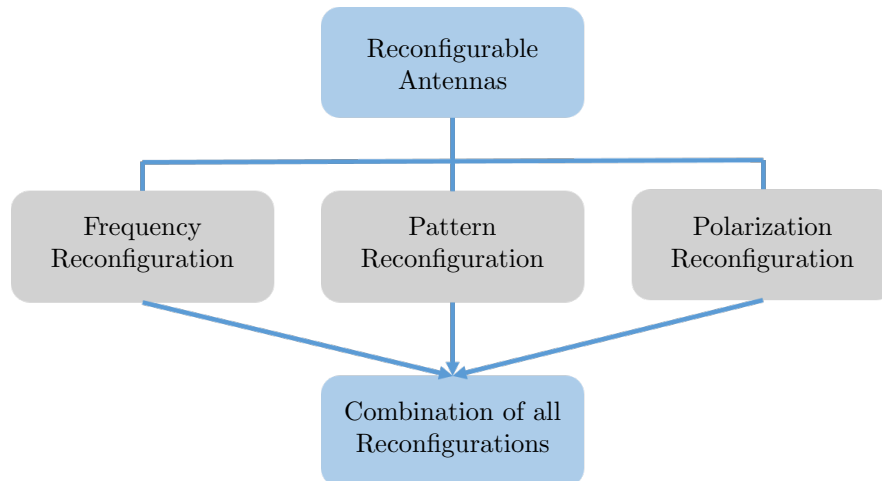
FIGURE 2.7: Different types of reconfigurations.
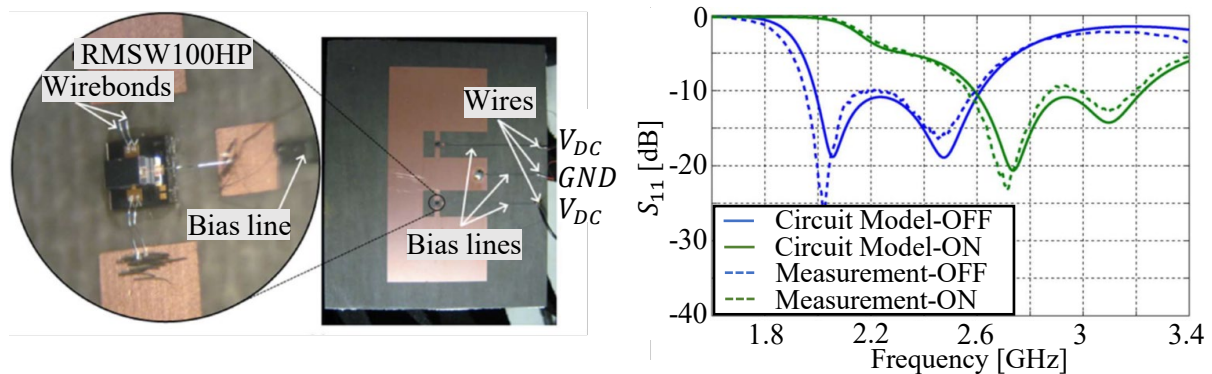
FIGURE 2.8: Frequency reconfigurable E-shaped patch antenna using MEMS and the reflection coefficient measurement, adapted from [87].

that are suitable for the use in adaptive antennas. Here, frequency reconfiguration is emphasized since this work deals mainly with the impedance variation of an antenna caused by the change in the environment. Frequency reconfiguration can be realized by using:

- Diodes or varactors:

  - Wide band antennas, in which the narrow band operation can be tuned by linking or de-linking radiating structure parts in such a way that different modes are excited [88–92].

- Wide band antennas, in which structure parts can be linked or de-linked to filter some bands [93, 94].

- Two antennas, one wide band antenna and the other a narrow band antenna. The narrow band antenna is tuned to achieve narrow band operation [95–98].

- A narrow band antenna that is frequency-tuned by diodes or varactors [99–103].

- An antenna that has switches in the radiating structure [104–108].

- A wide band antenna and a tunable filter right before the antenna for narrow band operation [109–116].

- A wide band antenna and a tunable filter right before the antenna for rejection band operation [117].

- A wide band antenna combined with resonant filter structure [118, 119].

- A wide band antenna and a defected microstrip structure (for narrow band operation) [120].

- Slot antenna with multiple feed positions. Eight feeds are simultaneously used for millimeter wave operation and only one feed for $2.05\,\text{GHz}$ to $2.7\,\text{GHz}$ operation. A varactor tunes the antenna [121].

- MEMS:

  - Frequency adjustment by linking or de-linking radiation parts of the radiating structure [122–124].

  - Frequency adjustment by tuning the antenna with MEMS-capacitance [125].

  - Frequency adjustment by loading the antenna with MEMS-switches [126–128].

  - Switching different feeds of the antenna [129].

- Photo diodes:

  - Frequency adjustment by linking or de-linking radiation parts of the radiating structure [130–132].

– Wide band antenna, where resonant structures can be linked or de-linked to filter some bands [133].

– The microstrip feed line of a slot antenna, tuned with a photo detector [134].

– Two antennas, one for sensing purpose, the other is reconfigurable by optical switches [135].

- Materials:

  – Instead of a copper patch antenna, a graphene patch is used. The resonant frequency changes with the chemical potential of graphene because the surface conductivity of graphene is dependent on the chemical potential. The chemical potential can be changed either by doping or by applying an external voltage [136]. (Only simulation and design approach).

  – A circular patch antenna with a stack of alumina and graphene as vias to ground is used. Upon the chemical potential, the resonant frequency can be changed [137] (simulation only).

  – A plasmonic dual band dipole using bi-layer graphene is presented in [138]. The conductivity by chemical potential is changed in such a way that the resonant frequency changes as well.

  – A patch antenna on a transparent liquid crystal substrate is used. The dielectric behaviour of this material changes when a static electric field is applied. This makes frequency reconfiguration possible [139].

  – A patch antenna on top of a graphene layer is used. With a DC voltage, the layer's conductivity is changed resulting in a frequency shift, depending on the DC voltage [140].

- Mechanical techniques:

  – Two antennas, one wide band antenna and the other a rotatable antenna. The feed remains at the same position while the radiation structure rotates [141–143].

– A monopole Sierpinski gasket, in which the feeding point is swept by a motor [144].

– A patch antenna on a substrate over (with an air gap) a ground plane that can be tilted mechanically is subject of [145].

– A patch antenna on top of a meta surface structure that can be rotated is shown in [146–148]. Upon the rotation angle the frequency can be reconfigured.

– A helix antenna is presented in [149]. The frequency can be adjusted by changing the height with a motor, similar to a screw.

- Feeds:

    – A narrow band antenna integrated into wide band antenna and feed independently [150, 151].

    – A 4 port antenna merged together: 3 loop antennas for narrow band operations, where each antenna covers a different frequency band and one UWB coplanar waveguide antenna [152].

    – At this point, reference is made to [153], which is the subject of this thesis and is dealt with in Chapter 4, "Adaptivity by Changing Feed Positions Along A Wire Antenna". A differential dipole-like antenna in a flexible foil with three ports is developed there. This antenna is adaptive to three largely different environments. Depending upon the environment, one port always acts as the feeding port, ensuring impedance matching while the other ones are short circuited. Depending upon the environment, the matched port is chosen. To the best of the author's knowledge, no comparable work has been carried out.

In Table 2.2 research works of pattern, polarization and all combinations of reconfigurations are listed. The techniques are similar to the ones used for frequency reconfigurations.

Active tuning is another method that can be used to make an antenna adaptive. Thereby, the impedance variation caused by the changing environment is compensated

TABLE 2.2: Summary of research works of pattern and polarization reconfiguration as well as combinations of all types of reconfigurations.

Type of reconfig.	Used components	Type of antenna	References
Pattern	Diodes	Monopole	[154]
Pattern	Diodes	Differential feed	[155–157]
Pattern	Diodes	Cubic slot	[158]
Pattern	Diodes	Reconfig. parasitic layer	[159]
Pattern	Diodes	Fractal	[160]
Pattern	Varactors	Impedance surface	[161]
Pattern	Diodes	Impedance surface	[162]
Pattern	MEMS	Square spiral microstrip	[163]
Pattern	MEMS	Planar dipole	[164]
Pattern	Graphene	V-shaped dipole	[165]
Pattern	Mechanical	U-gap	[166]
Pattern	Mechanical	Impedance surface	[167]
Polarization	Diodes	Slot	[168, 169]
Polarization	Diodes	Microstrip	[170–174]
Polarization	Diodes	Impedance surface	[175, 176]
Polarization	Diodes	Monopole	[177]
Polarization	MEMS	Patch	[178]
Polarization	MEMS	Monopole	[179]
Freq.+Polar.	Diodes	Microstrip	[180–182]
Freq.+Patt.	Diodes+Varact.	Monopole	[183]
Freq.+Patt.	Diodes	Slot	[184]
Freq.+Patt.	Diodes	Patch	[185]
Freq.+Patt.	Diodes	Pixel	[186]
Freq.+Patt.	MEMS	Patch	[187]
Polar.+Patt.	Diodes	Patch	[188]
Freq.+Polar.+Patt.	Diodes	Patch	[189]
Freq.+Polar.+Patt.	Diodes+Varact.	Circular patch	[190]
Freq.+Polar.+Patt.	Diodes	Pixel	[191]

by an electronically tuned impedance-matching network, mostly an ordinary ladder network. A typical functional block diagram is given in Fig. 2.9. The incident and reflected signal at the input of the impedance tuner is decoupled by a coupler and then the reflection coefficient is measured. Depending on the reflection coefficient, the biasing circuit changes the bias voltages of the tuning elements in the matching network, such that impedance matching is obtained. In [192], a helical antenna with an automatic impedance matching network is presented. This network compensates the impedance variation caused by the human operator in varying distances to the antenna.
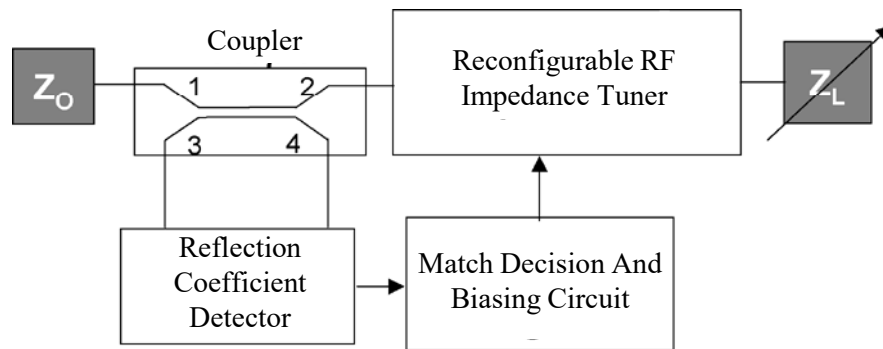
FIGURE 2.9: Functional block diagram of an automatic match control system, adapted from [197].

Similar works for mobile communication are presented in [193] and [194]. Instead of using a coupler, a measurement of the voltage at three points along a transmission line can be used to measure the input impedance of the antenna [195]. In [196], a tuned impedance-matching network adaptively corrects the impedance variation of the antenna in variable distances to a metal plate.

Another powerful method should be mentioned, which is used in pixel antennas. One example is depicted in Fig. 2.10. It comprises many metallic pixels (square patches), which are connected at the edges to the neighbouring pixels. Depending on the states of the switches, the antenna alters its properties, such as operation frequency or radiation. The states of all the switches for one particular goal are found by applying genetic algorithms as reviewed in [198]. In [199] an example of a pixel aperture irradiated by a horn antenna is given. Recently, the so-called internal multi-ports method (IMPM) has been successfully applied in pixel-antenna design, as shown in [200–203] and a similar method in [204].

In Fig. 2.11 the schematic of the IMPM is shown. There, one or more external ports excite the whole electromagnetic structure. The structure without any interconnections is described by the impedance matrix, whereby the interconnections, i.e. the switches, are represented by the internal ports terminated by circuit elements. The advantage of this method is that a full-wave field simulation must be done only once (to find the impedance matrix), where the states of the switches are determined with the help of an algorithm. In this thesis a theory is presented (in Chapter 4, "Adaptivity by Switched
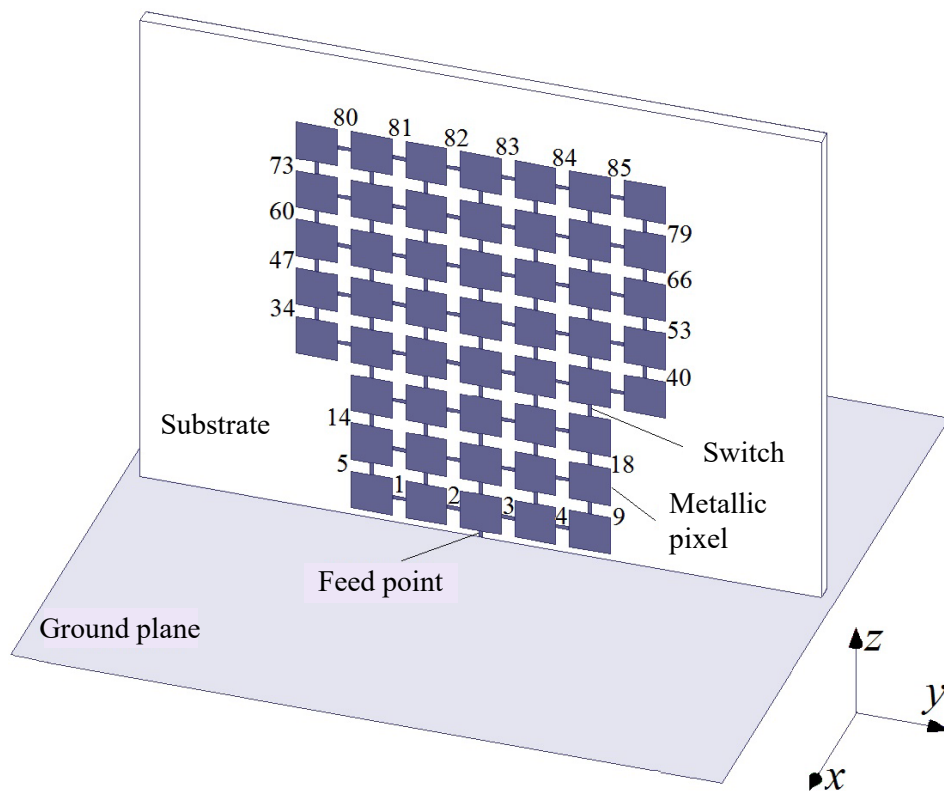
FIGURE 2.10: A typical pixel antenna given in [205].
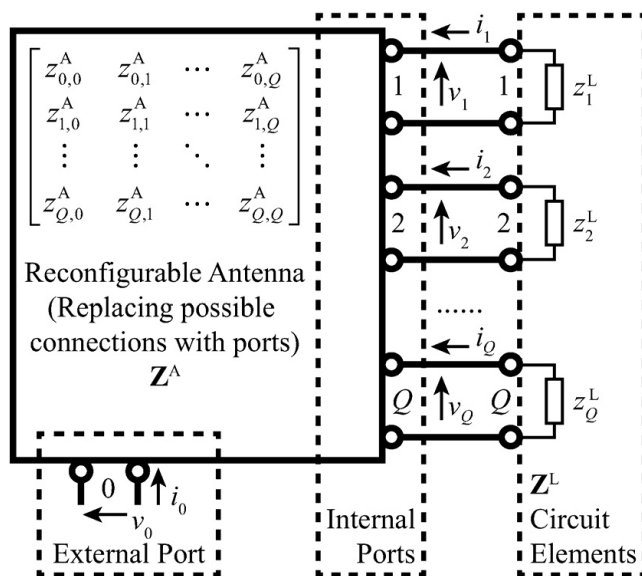
FIGURE 2.11: Illustration of the internal multi-ports method [206].

Load Admittances or Circuits") that allows calculations of the load impedances of internal ports to be carried out, thus ensuring impedance matching at all external ports at freely selectable frequencies. To the best of the author's knowledge, there is no work published that presents an equation from which the load impedance values can be calculated. This technique can be used for antenna reconfiguration and for evaluation to find a suitable load port position. In addition, it gives an alternative to the conventional impedance-matching network that is placed right before the impedance to be matched.

Chapter 3

Passively Adaptive Antennas

3.1   Introduction

Two concepts of passively adaptive antennas are introduced in this chapter. These do not require any active components such as diodes or transistors and are therefore very reliable. When the environment of the antenna alters, which is defined prior to the design process, the antennas of these concepts are inherently impedance matched to those changes.

The second section shows a concept that is applied in two different environments, namely, when the antenna is placed in free space and when it is placed close to a metal surface. In the third section a power divider network is presented that can adapt a dual-fed antenna to two different environments. Thereby, the first environment is free space while the second one is butter - as an organic example - in which the antenna is placed.

3.2   Resonant Mode Matching[1]

Usually, there are various types of antennas for different applications. Patch antennas always have a substrate and a ground plane, and are therefore, easily integrable into printed circuit boards (PCB) with other electronic components. On the other hand dipole like antennas are differential structures without a ground plane (if not placed in a well-defined distance, e.g. quarter wavelength), their applications are mostly seen in

---

[1]Most of the text and pictures presented in this section are extracted (or are modified versions) from [80]. The author is the main contributor to publication [80].

exposed locations, such as roofs or masts. There are many other examples for antennas that fit well in their specific applications. In some cases, an antenna is moved between two or multiple applications, e.g. when used in an RFID-tag. The very same antenna might not be usable anymore for all the different scenarios. To solve this problem the resonant mode matching can be used.

Every type of resonant antenna has its own current distribution at the resonant frequency, the so-called mode. The idea of resonant mode matching is to merge two or more different antennas within one structure, so that all their application scenarios are covered. Then, the geometric structure is manipulated, such, that for either scenario the resonant modes appear at the same frequency. Consequently, the antenna stays matched for all the scenarios, meaning it is adaptive for them. In the following an antenna design is presented that uses the mode matching method for two scenarios; firstly, when the antenna is placed in free space, and, secondly, when placed close to a metal surface.

3.2.1   Single-Layer Planar Antenna: The Concept

The proposed antenna is a single-layer planar structure and a combination of a slot antenna and a coplanar waveguide patch antenna (where for the latter, the close-by metal ground acts as ground for the patch). The operation of a coplanar waveguide patch antenna is reported in [207]. Fig. 3.1 shows the layout of the proposed antenna with all dimensions, with the values of these dimensions listed in Table 3.1. The elongated rectangular patch in combination with the surrounding ground plane (Fig. 3.2 (a)) is the basic resonant element of the antenna. This patch is fed with a coplanar waveguide at a position, where impedance match is achieved as it is usually done in patch antenna design. However, this feed line has an impedance not equal to $50\,\Omega$, otherwise, the dimensions would become critical (too small gap) for the etching process. A matching slot is added, as part of impedance matching network. This matching slot is also functional for radiation, where it tunes the resonance frequency suitably, as discussed below.
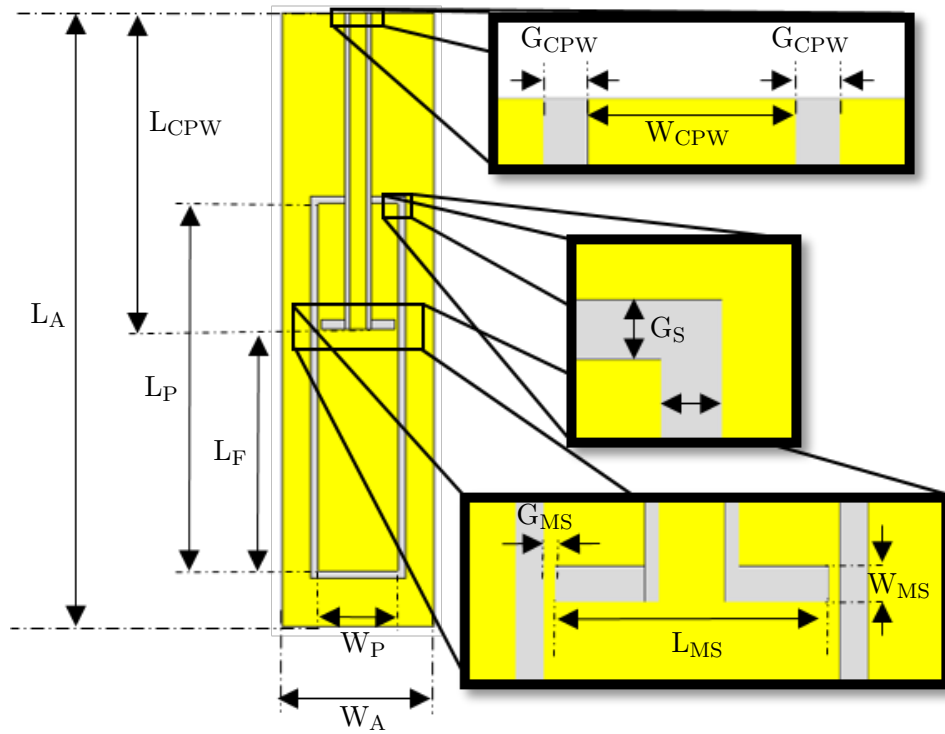
FIGURE 3.1: Layout and dimensions of the single layer antenna [80].

Placing a ground plane just below, the proposed antenna shows similar behaviour to a conventional patch antenna. In the following, this is called the patch mode. If the proposed antenna is in free space, it behaves like a slot antenna with according field distribution, which is called the slot mode. These two cases are discussed in the following and form the basic principle to make the antenna unaffected by a close-by metal surface. For all other cases, in which the ground plane distance is in-between these two extreme cases, the measurements (see subsection "Measurements") show that a weighted superposition of the two modes result in only minor variation of feed impedance. The latter can be explained by the fact that both the slot mode and the patch mode have rather similar distributions of resonant currents and fields.

A. Patch Mode

Fig. 3.2 (a) depicts the top view of the antenna. Additionally, the solid black line in Fig. 3.2 (a) indicates the cut plane, in which the electric field shown in Figs. 3.2 (b)

TABLE 3.1: The dimensions of the single layer antenna.

Label	Value [mm]	Label	Value [mm]
L_P	24.5	G_S	0.5
W_P	5.26	G_{MS}	0.2
L_F	16.1	L_{MS}	4.87
G_{CPW}	0.25	W_{MS}	0.65
W_{CPW}	1.17	L_A	41
L_{CPW}	28.85	W_A	10
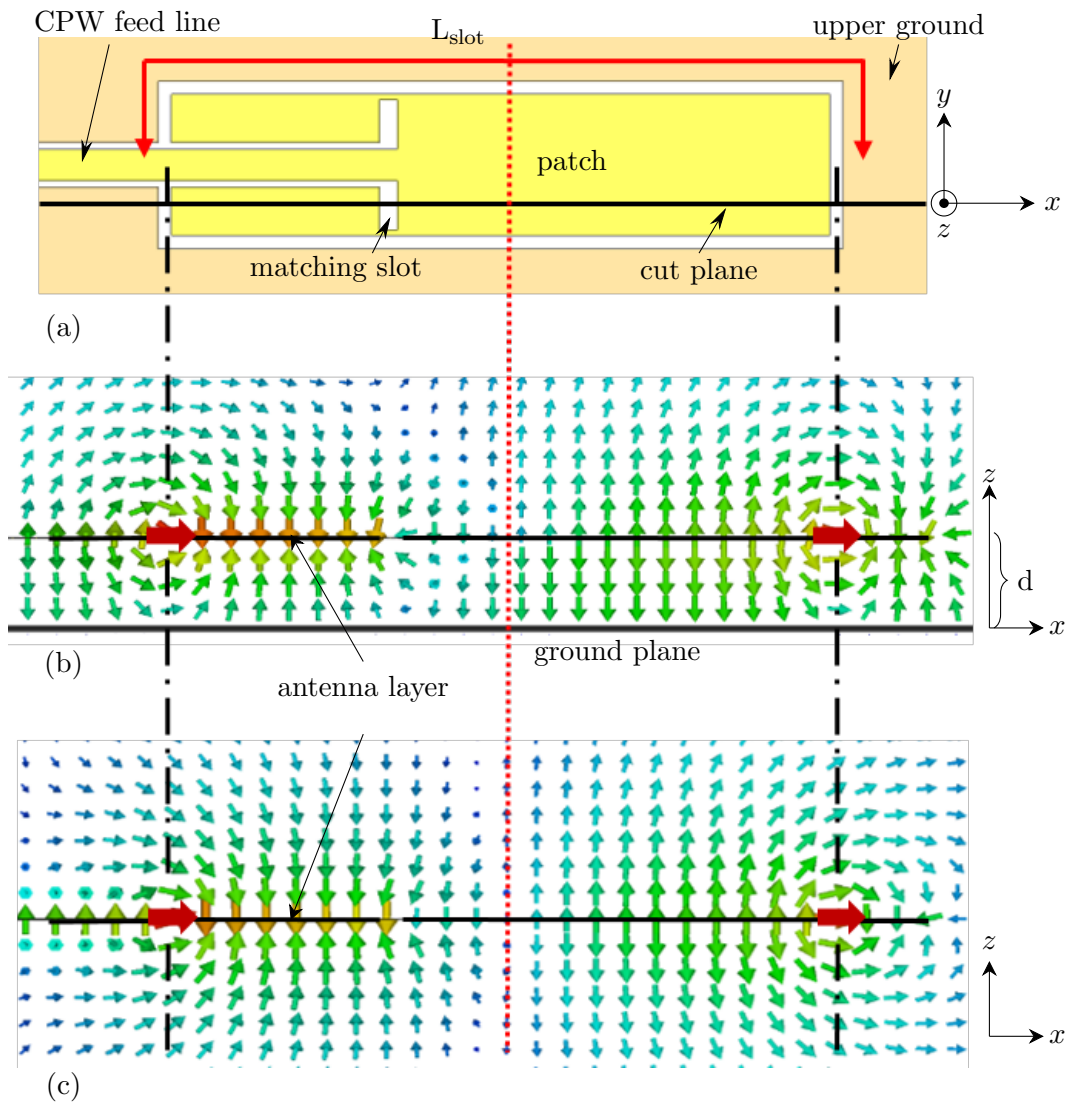
FIGURE 3.2: Top view of the antenna (a) and the respective electric field in patch-mode (b) and slot-mode (c) [80].

and 3.2 (c) is considered. Fig. 3.2 (b) shows the electric field for a distance d between the antenna and the ground plane of d = $4\,\text{mm}$. The black dot-dashed line in the field plots marks the patch edges, parallel to the y-axis. Along these edges, the electric field magnitude is large. On the right edge of the patch, the electric field closes, between the patch and the lower and upper ground plane, in a way such that a positive potential exists on the patch side and a negative potential on side of the ground plane. On the left edge of the patch, it is the other way around. Thus, the surface current on the patch is directed from the left edge to the right edge. Fig. 3.3 (a) shows the surface current at the same time on the ground plane. Right under the patch, the current floats from the right side to the left side. Consequently, the surface current on the patch faces in the opposite direction as that on the ground plane. This, as well as the field distribution directly below the patch show the similarity to the conventional patch antenna. Due to the two ground planes (bottom and top), the fringing fields are rather weak compared to the conventional patch antenna, which is also reflected in the narrow bandwidth of the antenna. It is striking that the electric field in the middle under the patch (position of the red dotted line) does not become zero. Instead the zero appears only left offset from the centre. The reason for this is the matching slot, which increases the electrical length of the patch in the patch mode and allows to bring the patch to the same resonance frequency as the antenna in slot mode.

B. Slot Mode

Fig. 3.2 (c) shows the electric field distribution in the cut plane for the case in which the antenna is located in free space (without ground). In principle, the field distribution is very similar to the patch mode and thus allows good adaptation for both cases and all cases in which the ground plane varies in the distance to the antenna. Since there is no longer any ground plane on which a current can flow across the slot, located parallel to the y-axis, the current must flow along the outer and inner edges. Thus, this length determines the resonance frequency for the slot mode case. The length L_{slot} is the mean length of inner and outer edge (red double arrow in Fig. 3.2 (a)) and is given

(a)

(b)
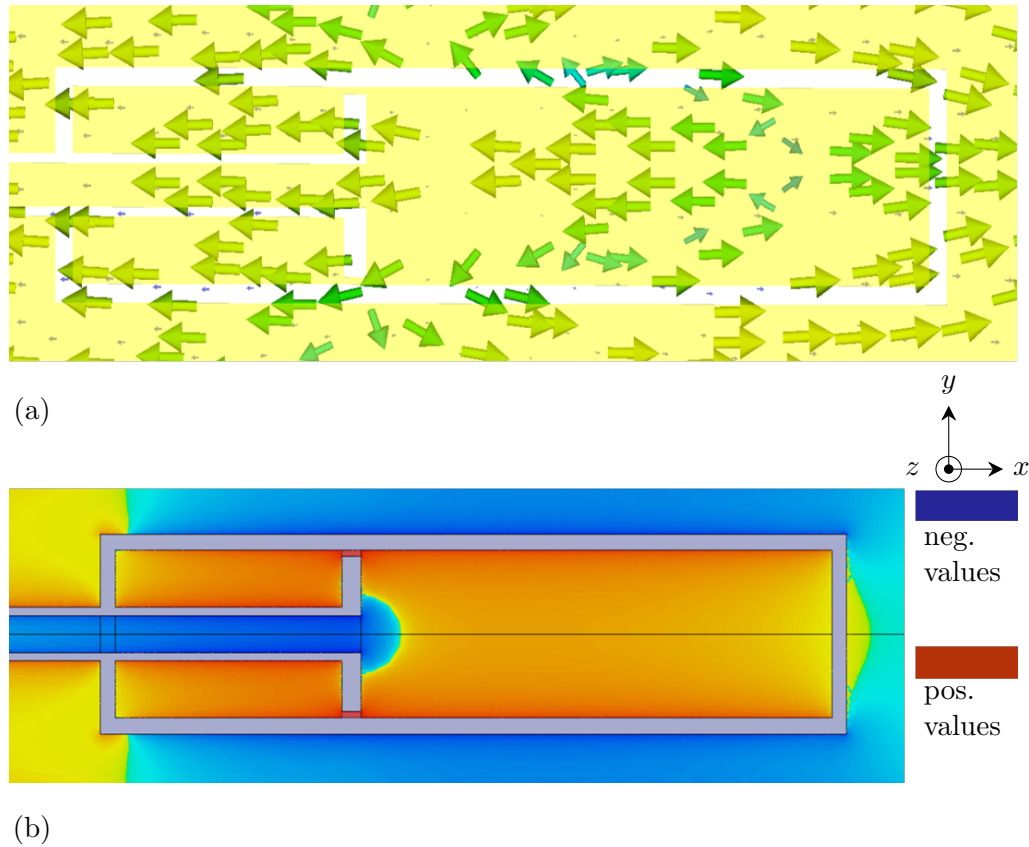
FIGURE 3.3: Surface current (a) vectors on the ground plane in patch mode and (b) the logarithmic x-component of the surface current in slot-mode [80].

as:

$$L_{\text{slot}} = W_P + L_P + 2G_S \approx \frac{\lambda_0}{2} \tag{3.1}$$

Fig. 3.3 (b) shows the logarithmic x-component of the surface current of the antenna in slot-mode. Here, the blue colour stands for negative values, that corresponds to a current floating from the right-side to the left-side. Accordingly, the red colour, i.e. positive values corresponds to the opposite direction. Again, this behaviour of the surface current is very similar to the patch mode.

3.2.2 Single-Layer Planar Antenna: Measurements

According to the layout from Fig. 3.1, a printed circuit board is manufactured. The physical stability is provided by a polymer substrate (liquid crystal polymer,

(a) (b)
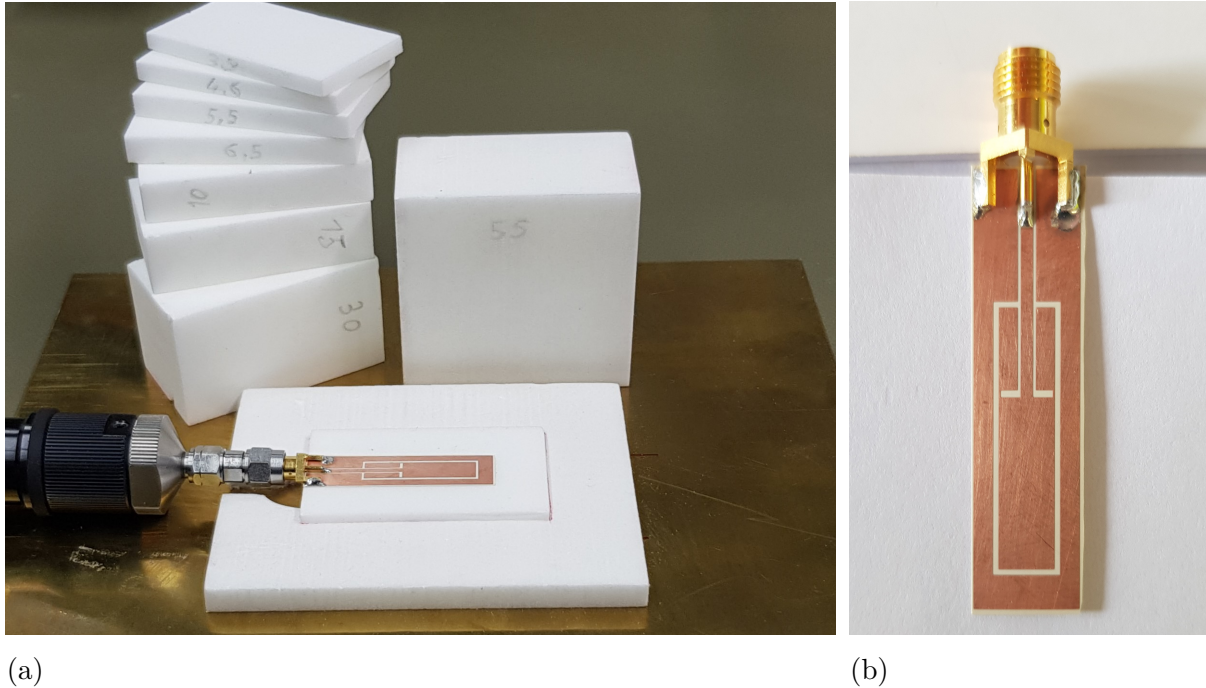
FIGURE 3.4: (a) Photograph of the measurement setup for measuring the reflection coefficient for different distances between metal ground plane and antenna [80] and (b) a front view photograph of the antenna.

LCP, Rogers ULTRALAM 3850) of $0.1\,\mathrm{mm}$ thickness. In Fig. 3.4 (a), a picture of the measurement setup for measuring the reflection coefficient is shown. Figure 3.4 (b) shows a photograph of the antenna in the front view. The antenna optionally placed on top of foam (ROHACELL 51 HF) blocks with different heights ranging from $4\,\mathrm{mm}$ to $250\,\mathrm{mm}$. This material is electromagnetically transparent and ensures a precise measurement on top of the $200 \times 200\,\mathrm{mm}^2$ metal ground plane.

Fig. 3.5 shows the measurements of the antenna feed reflection coefficient magnitude (in dB) over frequency for varying distance d. Each one of the black curves corresponds to a specific distance d between the antenna and the metal ground plane. Generally, the resonance frequency decreases if distance d increases. In addition, the simulated reflection coefficient for the patch mode (blue dashed line) and slot mode (red dotted line) are shown in the graph.

Comparing simulation and measurements, a certain frequency shift is obvious. This can be explained by imprecise manufacturing, in particular, poor etching accuracy. Specifically, some of the layout dimensions are close to the resolution limit, and some
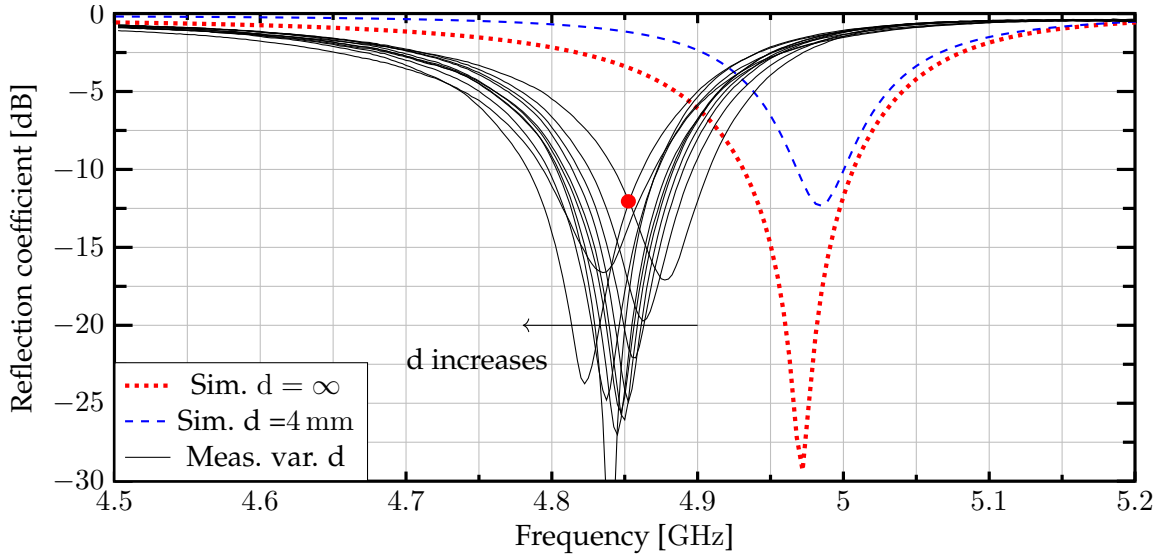
FIGURE 3.5: Measured reflection coefficient magnitude (in dB) over frequency for different distances d between antenna and metal ground plane [80].

metal edges are very sensitive as they are carrying high currents. To verify this, the sensitive edges and corners are rounded (radius of $100\,\mu m$) and varied by $\pm 80\,\mu m$ in a modified simulation model, resulting in a maximum frequency shift of about $178\,MHz$ between $4.861\,GHz$ and $5.038\,GHz$ considering the two extreme cases (patch and slot mode). Since the dimensions of the connector are large compared to the antenna, the connector is included in simulation as well. From Fig. 3.5 it can be seen that the resonant frequency variation over the distance d becomes somewhat blurred. Therefore, the working frequency is defined as the frequency point, where minimum reflection occurs by considering all distances. This point is at $4.855\,GHz$ and is marked with a red dot in the graph of Fig. 3.5. Note that the bandwidth of the antenna increases, when d increases. This is to be expected since a patch antenna typically has smaller bandwidth than a dipole (or, slot) antenna.

Fig. 3.6 shows the measured feed impedance variation as a function of distance d, where d is ranging from $4\,mm$ to $250\,mm$. The frequency is chosen as $4.855\,GHz$. For means of comparison, the feed impedance variation of a coax-fed monopole antenna at distance d over ground, is simulated and the results are added to Fig. 3.6. Figure 3.7 shows the geometry of this simulated monopole. The coplanar waveguide of this monopole has the same dimensions as for the proposed antenna. Referring to Fig. 3.6,
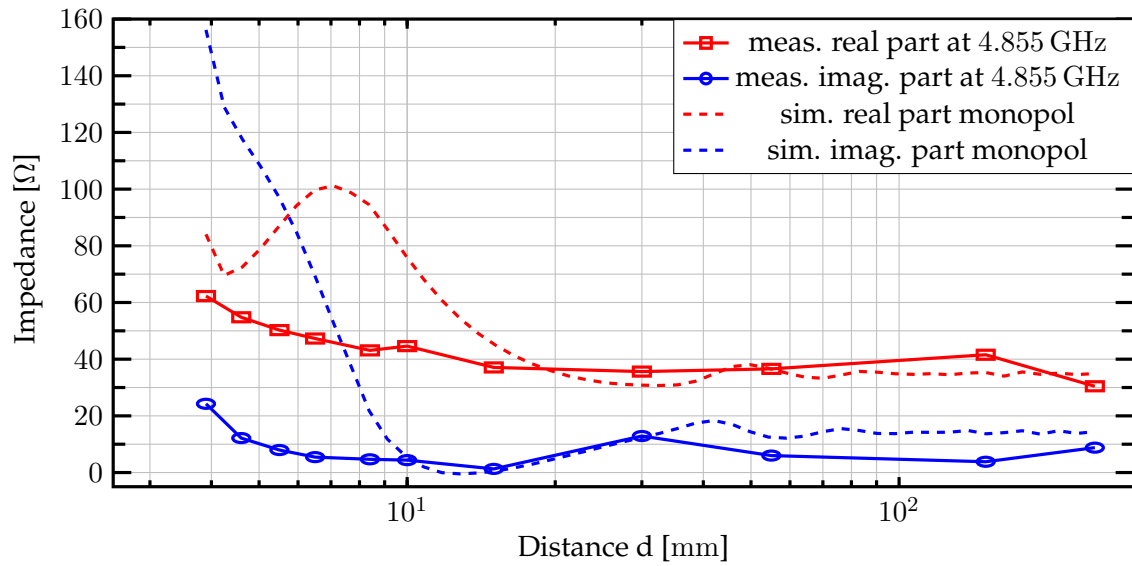
FIGURE 3.6: Measured input impedance variation over the distance between ground plane and antenna in comparison with a monopole [80].
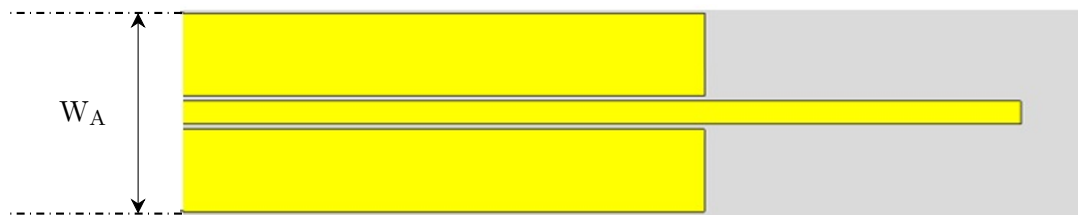
FIGURE 3.7: Layout of the monopole ($W_A = 10\,\text{mm}$) [80].

the impedance variation of the monopole due to the close-by metal surface is large (in line with literature, e.g., [54]) and the variation of the feed impedance of the proposed antenna is quite small.

Fig. 3.8 shows a polar plot of the radiation pattern in H plane (zy-plane in Fig. 3.2 (a)) at $4.855\,\text{GHz}$. The peak directivity, is obtained by integration of the measured 3D radiation pattern in a spherical scanner, measured in the far-field. Two curves are depicted. The blue curve is corresponding to the slot mode, i.e. in free space, and the red curve is related to the patch mode with a distance between ground plane and antenna of $d = 4\,\text{mm}$. The red curve shows the typical behaviour of a patch antenna and the blue one like a dipole. The measured peak directivity in H-plane has a value of 7.1 dBi for the patch mode.
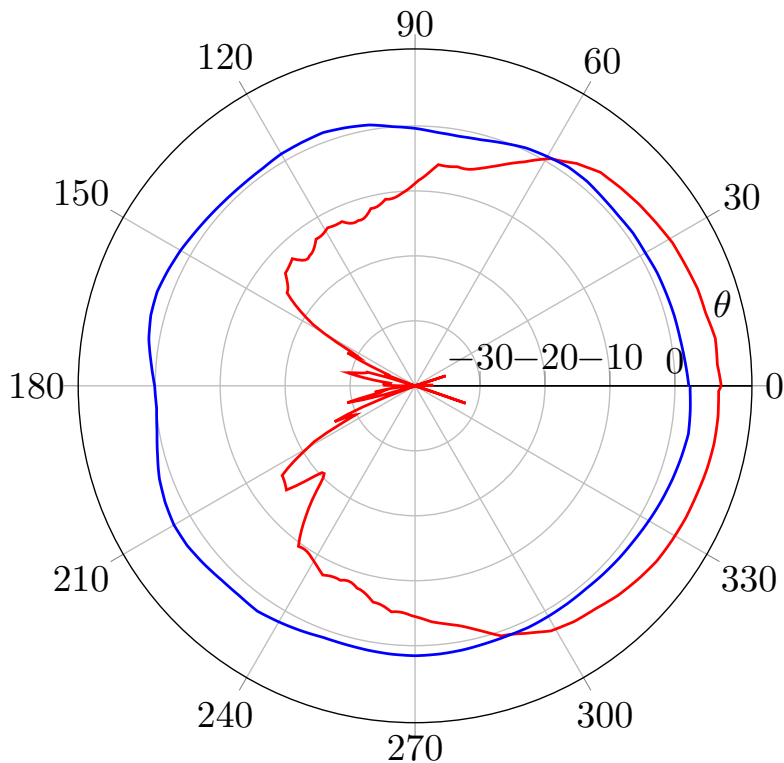
FIGURE 3.8: Measured directivity in dBi over theta in H-plane. The blue line corresponds to slot-mode and the red line to patch-mode [80].

3.2.3 Discussion

This chapter gives one possible solution to the question how a passive adaptive antenna design can be made using mode matching method. This method is based on different resonant antennas, which are then merged into one single structure. Ideally, the merged structure shows as many modes as antennas are merged. Each mode corresponds to one antenna and therefore to one scenario (since one antenna covers one scenario). Then the structure is manipulated in such a way that all the resonant modes occur at the same frequency.

An antenna concept is presented that demonstrates the mode matching method for two scenarios, namely, when the antenna is placed in free space and when placed close to a metal surface. It is also shown that not only both scenarios are well covered, but also a transition between them, meaning all distances greater than $4\,\mathrm{mm}$ from the metal surface. Over all these distances a feed match better than -12 dB is measured at the

frequency of $4.85\,$GHz. Further, the far-field directivity is measured in H-plane for the case of free-space and for the metal surface at a distance of $4\,$mm. For the first case the directivity shows approximate omnidirectional behaviour as known from a dipole and the second case shows a behaviour as it is known from a patch-antenna. The measured main lobe achieves a directivity of 7.1 dBi.

These results verify the concept. On the one hand, the measurements correspond to the predictions of the simulations, and, on the other hand, the far-field pattern can be clearly assigned to the respective mode and the related antenna type (mode matching method).

Nevertheless, this method may not be applicable for all antenna types, because not all of them and their modes are mergeable. In fact, this work is not intended to be a universal approach but an approach for a possible realisation. In addition, the manipulation of the merged structure may result in degradation of the performance when compared to the unmerged antennas, e.g. the slot antenna narrows the bandwidth of the patch antenna. In relation to this, effort can still be expended to increase the bandwidth if this should be desired in the application. Further investigations can be made based on this work. For example, more than two scenarios can be covered if more than two antenna structures are merged together. Also, it is quite possible that other modes may occur that can be used in addition to those that are clearly associated with an antenna. Finally, an approach is presented here that shows how a passive adaptive antenna can be designed using the mode matching method. This approach has been verified by a prototype.

3.3   Adaptivity by Power Divider Network[2]

When placing an antenna in different electromagnetic environments, so-called scenarios, i.e. varying dielectric properties and losses in the surrounding materials the input impedance will change. Consequently, a multiply-fed, or, as in the following case, a doubly-fed antenna shows different feed impedances at different feed points

---

[2]Some of the text and pictures presented in this section are extracted (or are modified versions) from [74]. The author is the main contributor to publication [74].
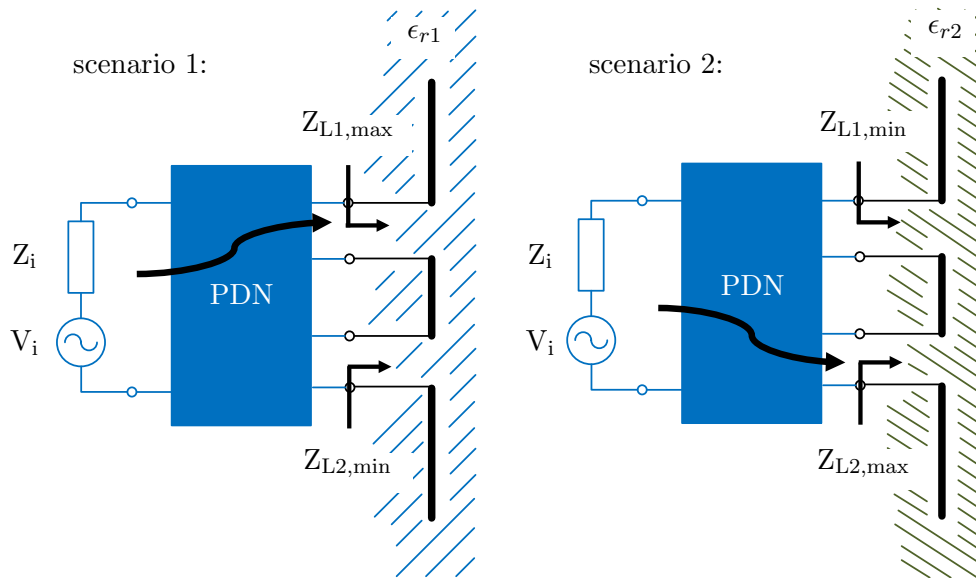
FIGURE 3.9: Concept of matching a dual-fed antenna to a source by a power divider network (PDN). Varying antenna feed impedances due to environmental (near-field) changes to the antenna cause the power flow to change from connecting feed one with the source in the first scenario, while connecting feed two with the source in the second scenario [74].

of different scenarios. This fact is exploited in the following power divider network (PDN). In the first scenario, "scenario 1", one of the two feed points is chosen to be the port, in which most of the power from the source is transferred, while the other port should receive as less as possible of the source power. In the second scenario, "scenario 2", it is the other way around. In Fig. 3.9 the principle is depicted. The bent arrows indicate the main power flow.

Most simplified case: The circuit of Fig. 3.10 (a), i.e., just two resistors R_1 and R_2, in parallel with source voltage V_i and source resistor R_i, is considered. There are two scenarios assumed, where R_1 and R_2 have different values, while R_i remains constant. For a particular valueset of R_1 and R_2, which is scenario 1, matching between the source, and the two resistors are obtained. In scenario 2 the values of R_1 and R_2 are interchanged in such a way that the source is still matched to the load. In Fig. 3.10 (b) the normalized (to the maximum available power of the source) power dissipated in R_1 (red dashed line "p_1") and in R_2 (blue dotted line "p_2") are shown. Thereby, the value R_1 varies from $10\,\Omega$ to $450\,\Omega$ while R_2 varies from $450\,\Omega$ to $10\,\Omega$ as indicated by
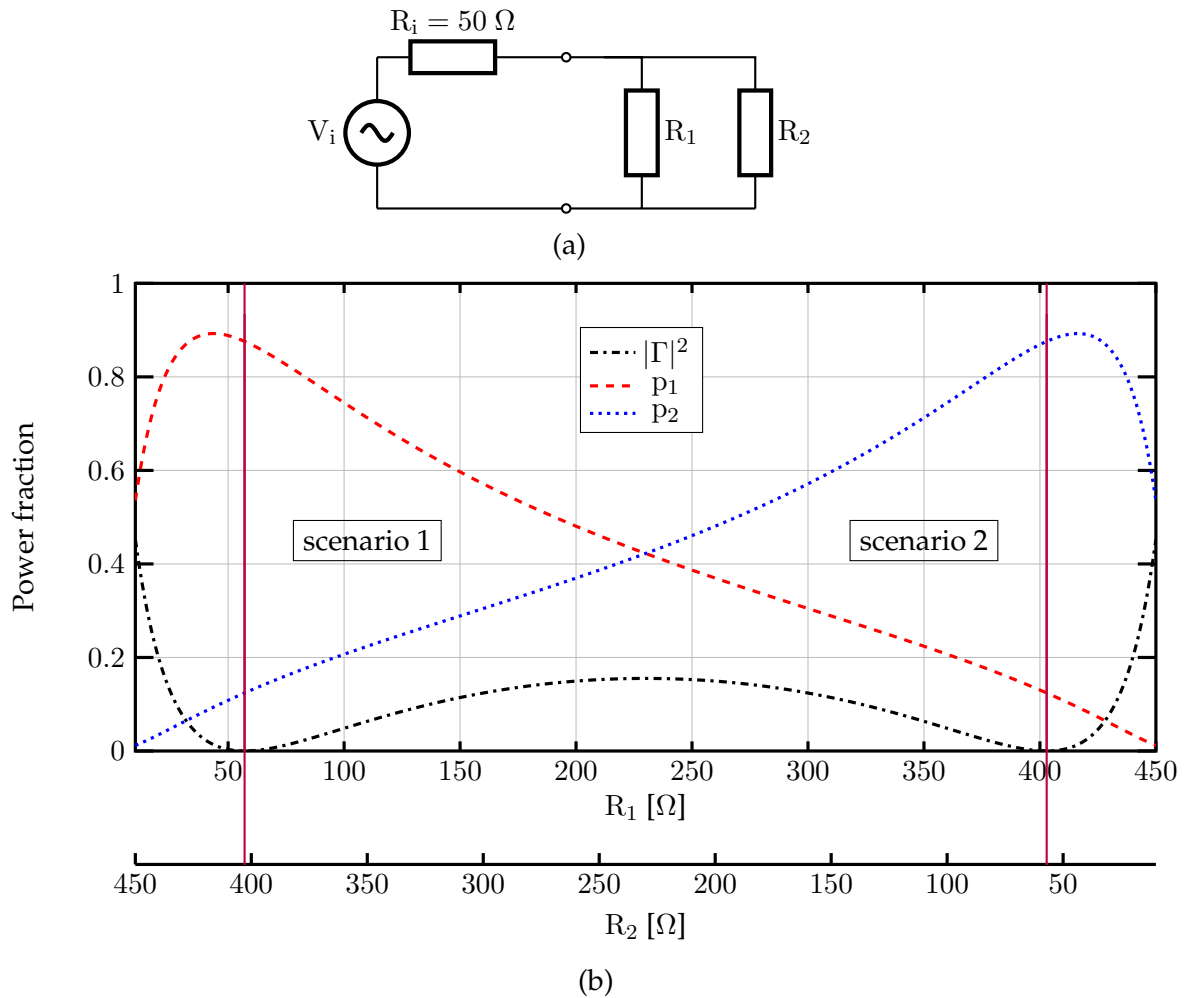
FIGURE 3.10: (a) Two resistors in parallel and (b) portions of the maximum power, which the source can deliver: Reflected power $|\Gamma|^2$ (black dash-dotted line), the power dissipated in R_1 (p_1 red dashed line) and the power dissipated in R_2 (p_2 blue dotted line) [74].

the two x-axes. The two vertical solid lines indicate the two scenarios. In addition, the reflected power (black dash-dotted line) is plotted. In these scenarios, the reflected power is zero. In scenario 1 the dissipated power in $R_1 = R_{1,max}$ ($\approx 57\,\Omega$) is $87.6\,\%$ of the maximum power that the source can deliver. Then, the dissipated power in $R_2 = R_{2,min}$ ($\approx 403\,\Omega$) is $12.4\,\%$. In scenario 2 it is the other way around, as can be seen in Fig. 3.10 (b). Consequently, this behaviour can be seen as a natural power switch that flips in dependency on the load. It is also clear that, for a particular scenario, one of the resistors should have a value that is as close as possible to the value of the source resistance. If this is the case, the value of the other resistor must be very high in order

to achieve matching.

A power divider network based on transmission lines is developed which trans-
forms (for both scenarios) two impedances in such a way that for scenario 1 most of the
power is transferred to the first complex impedance and for scenario 2 to the second
complex impedance. Therefore, it is important to note that in the general case, the
four complex loads can be chosen arbitrarily (contrary to the aforementioned most
simplified case).

3.3.1   Concept

The PDN consists of two parallel arms, which in turn consist of an impedance
transformation network (ITN), which is composed of two transmission line sections in
series. To include the transmission lines (TLs) properly within the circuit analysis and
theoretical consideration a TL model is developed comprising lumped elements.

3.3.1.1   Transmission Line Model

The approach is based on the well-known equivalent circuit for a transmission
line as given in [208]. This lumped-element equivalent circuit of a small length of
a transmission line is continued periodically leading, again to a lumped-element
equivalent circuit. In Fig. 3.11 (a) the TL model is depicted. The dotted lines indicate
the periodically continuation of the components

$$Z'_s = R'_s + j\omega L' \tag{3.2a}$$

$$Y'_p = G'_p + j\omega C'. \tag{3.2b}$$

Thereby, the apostrophe shows the unit per length, e.g. Z'_s has the unit $\Omega\,\mathrm{m}^{-1}$ and Y'_p,
$\mathrm{S\,m}^{-1}$. Further, $\omega = 2\pi f$ is the angular frequency, f the frequency and j the imaginary
unit. The TL is terminated with the load impedance Z_L. Now, Z'_s and Y'_p are referred to
small line length $\Delta l = {}^L/_N$ and

$$Z_s = Z'_s \Delta l \tag{3.3a}$$
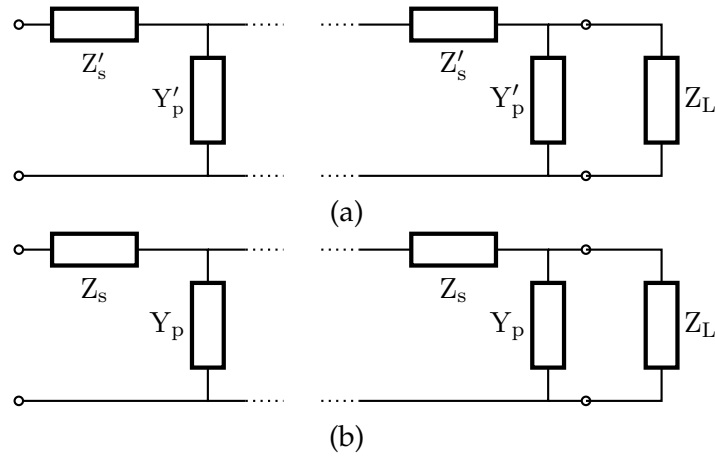
FIGURE 3.11: Periodically continued ladder network with (a) the line constants of a small line length of the TL and (b), where the line constants are referred to a small line length.

$$Y_p = Y'_p \Delta l = \frac{1}{Z_p} \tag{3.3b}$$

is obtained. L is the total length of the TL and N the number of periods. The corresponding equivalent circuit is shown in Fig. 3.11 (b). For $N = 1$ the input impedance of the network is

$$Z_1 = \frac{Z_s Z_p + (Z_s + Z_p) Z_L}{Z_p + Z_L}. \tag{3.4}$$

Further calculations of following periods and the recognition of the pattern of this equation type allows to obtain the input impedance for N periods

$$Z_N = Z_s \frac{Z_p f_a(N, x) + Z_L f_b(N, x)}{Z_p f_c(N, x) + Z_L f_a(N, x)} \tag{3.5}$$

with

$$f_a(N, x) = \sum_{k=0}^{N-1} \binom{2N - k - 1}{k} x^k = \frac{\left(a_1{}^N - a_2{}^N\right)}{2^N \sqrt{4x + 1}}, \tag{3.6a}$$

$$f_b(N, x) = \sum_{k=0}^{N} \binom{2N - k}{k} x^k = \frac{\left(\left(\sqrt{4x + 1} + 1\right) a_1{}^N + \left(\sqrt{4x + 1} - 1\right) a_2{}^N\right)}{2^{N+1} \sqrt{4x + 1}}, \tag{3.6b}$$

$$f_c(N, x) = f_b(N - 1, x), \tag{3.6c}$$

$$a_1 = \left(1 + 2x + \sqrt{4x + 1}\right), \tag{3.6d}$$

$$a_2 = \left(1 + 2x - \sqrt{4x + 1}\right), \tag{3.6e}$$

and $x = Z_p/Z_s$. Here, the term in brackets within the sum is the fitted binomial coefficient. The goal is to obtain a simple network, e.g. as it is for $N = 1$ ((3.4)). Multiplying a parameter p and rearranging change (3.5) to

$$Z_N = \frac{pZ_sZ_p + Z_s\frac{f_b(N,x)}{f_a(N,x)}pZ_L}{p\frac{f_c(N,x)}{f_a(N,x)}Z_p + pZ_L}. \tag{3.7}$$

If following substitutions

$$\tilde{Z}_s\tilde{Z}_p = uZ_sZ_p \tag{3.8a}$$

$$\tilde{Z}_s + \tilde{Z}_p = Z_s\frac{f_b(N,x)}{f_a(N,x)} \tag{3.8b}$$

$$\tilde{Z}_p = p\frac{f_c(N,x)}{f_a(N,x)}Z_p. \tag{3.8c}$$

are applied, (3.7) takes the form of (3.4), except of parameter p as product with the load impedance Z_L. This parameter appears to be related to an ideal transformers' turn ratio, as will become clear later on. Solving (3.8) leads to

$$\tilde{Z}_s = A\sqrt{Z_sZ_p} \tag{3.9a}$$

$$\tilde{Z}_p = \frac{B - A^2}{A}\sqrt{Z_sZ_p} \tag{3.9b}$$

$$p = B - A^2. \tag{3.9c}$$

with

$$A = \sqrt{\frac{Z_s}{Z_p}\frac{f_a(N,x)}{f_c(N,x)}} = \frac{1}{\sqrt{x}}\frac{f_a(N,x)}{f_c(N,x)} \tag{3.10a}$$

$$B = \frac{Z_s}{Z_p}\frac{f_b(N,x)}{f_c(N,x)} = \frac{1}{x}\frac{f_b(N,x)}{f_c(N,x)}. \tag{3.10b}$$

With

$$x = \frac{Z_p}{Z_s} = \frac{Z'_p}{Z'_s}\frac{1}{(\Delta L)^2} = \frac{Z'_p}{Z'_s}\frac{N^2}{L^2} = \frac{N^2}{(\gamma L)^2}. \tag{3.11}$$

and (3.6), it can be shown that for an infinity number of periods:

$$\lim_{N\to\infty} A = \tanh(\gamma L) \tag{3.12a}$$

$$\lim_{N\to\infty} B = 1. \tag{3.12b}$$

Where $\gamma = \alpha + j\beta$ is the propagation constant of the TL, α the attenuation constant and β the phase constant. Finally, it is stated:

$$\tilde{Z}_s = \tanh(\gamma L)\sqrt{Z_s Z_p} \tag{3.13a}$$

$$\tilde{Z}_p = \frac{1 - \tanh(\gamma L)^2}{\tanh(\gamma L)}\sqrt{Z_s Z_p} \tag{3.13b}$$

$$p = 1 - \tanh(\gamma L)^2. \tag{3.13c}$$

$$u = \pm\sqrt{p} \tag{3.13d}$$

The factor u has two solutions by root extraction. In terms of circuitry, the solution with the positive sign is correct for line lengths between 0 and $\lambda/4$ and between $3\lambda/4$ and λ. The other interval where the negative sign is valid is between $\lambda/4$ and $3\lambda/4$. Now, considering the input impedance of the network with $N \to \infty$

$$Z_\infty = \frac{\tilde{Z}_s\tilde{Z}_p + (\tilde{Z}_s + \tilde{Z}_p)u^2 Z_L}{\tilde{Z}_p + u^2 Z_L}. \tag{3.14}$$

As can be seen it has the same form as in case of $N = 1$, except of u^2. Although, this parameter can be seen as turn ratio of an ideal transformer. If so, a circuit after Fig. 3.12 (a) can be found that fits the formulae. In Fig. 3.12 (b) the parallel impedance $\tilde{Z}_p$ at the primary side is transformed to the secondary side. Following formulae are then obtained

$$\tilde{Z}_s = \tanh(\gamma L)\sqrt{Z_s Z_p} \tag{3.15a}$$

$$\tilde{\tilde{Z}}_p = \frac{\sqrt{Z_s Z_p}}{\tanh(\gamma L)} \tag{3.15b}$$

$$p = 1 - \tanh(\gamma L)^2 = 1 - \frac{\tilde{Z}_s}{\tilde{\tilde{Z}}_p}. \tag{3.15c}$$
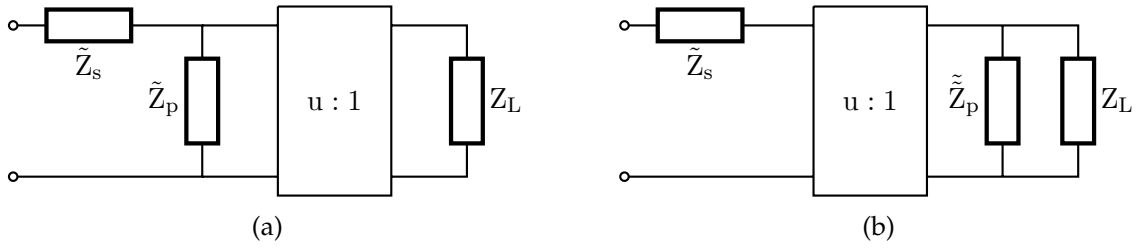
FIGURE 3.12: Two variants of the derived transmission line model.

$$u = \pm\sqrt{p}. \tag{3.15d}$$

Also, following relation shoud be noted:

$$\sqrt{Z_s Z_p} = \sqrt{Z_s' Z_p'} = Z_0. \tag{3.16}$$

Where, Z_0 is the characteristic impedance of the line.

3.3.1.2 Impedance Transformation Network

Two TL models, as derived in the previous subsection, are combined in series and form the ITN. In Fig. 3.13 a circuit model of the ITN is depicted. According to the labels and assuming lossless transmission lines the model formulae read:

$$Z_{s,i} = j\tan(\beta L_i)Z_0 = jX_{s,i} \tag{3.17a}$$

$$Z_{p,i} = -j\cot(\beta L_i)Z_0 = jX_{p,i} \tag{3.17b}$$

$$u_i = \text{sgn}\left(\cos(\beta L_i)\right)\sqrt{1 + \tan(\beta L_i)^2} \tag{3.17c}$$
$$= \text{sgn}\left(\cos(\beta L_i)\right)\sqrt{1 - \frac{X_{s,i}}{X_{p,i}}}.$$

Where $i = 1, 2$ indicates the first and the second line with the lengths L_1 and L_2, respectively. With nodal analysis
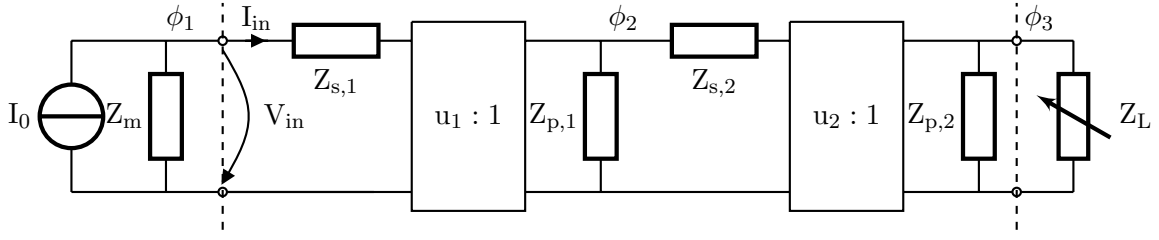
FIGURE 3.13: Circuit model of a two-step transmission line-based impedance transformer with source and load impedance.

$$\begin{pmatrix} \frac{1}{Z_{s,1}} & -\frac{u_1}{Z_{s,1}} & 0 \\ -\frac{u_1}{Z_{s,1}} & \frac{u_1^2}{Z_{s,1}} + \frac{1}{Z_{p,1}} + \frac{1}{Z_{p,2}} & -\frac{u_2}{Z_{s,2}} \\ 0 & -\frac{u_2}{Z_{s,2}} & \frac{u_2^2}{Z_{s,2}} + \frac{1}{Z_{p,2}} + \frac{1}{Z_L} \end{pmatrix} \begin{pmatrix} \phi_1 \\ \phi_2 \\ \phi_3 \end{pmatrix} = \begin{pmatrix} I_0 \\ 0 \\ 0 \end{pmatrix}, \tag{3.18}$$

the input voltage

$$V_{in} = \phi_1 \tag{3.19}$$

and the input current

$$I_e = \left(\frac{u_1^2}{Z_{s,1}} + \frac{1}{Z_{p,1}} \right) \phi_1 - \frac{u_1}{Z_{s,1}} \phi_2 \tag{3.20}$$

the input impedance can be calculated to

$$Z_{in} = \frac{Z_{p,1} \left(Z_L Z_{p,2} + Z_L Z_{s,1} + Z_{p,2} Z_{s,1} + Z_{p,2} Z_{s,2} \right)}{Z_L Z_{p,1} + Z_L Z_{p,2} + Z_{p,1} Z_{p,2} + Z_{p,2} Z_{s,2}}. \tag{3.21}$$

The load impedance Z_L (i.e., antenna feed impedance) can take two different values, as indicated in Fig. 3.13 as variable impedance. The ITN has the following properties: (i) Maximum power transfer through the ITN, with respect to the source impedance Z_m, for the load impedance $Z_L = Z_{L,max}$. (ii) Minimum power transfer through the ITN, with respect to the source impedance Z_m, for the load impedance $Z_L = Z_{L,min}$. In the first case, if $Z_L = Z_{L,max}$, the ITN provides conjugate-complex match

$$Z_{in}|_{Z_L=Z_{L,max}} = Z_m^* \tag{3.22}$$

for maximum power transfer. Considering (3.21), then (3.22) leads to

$$X_{p,1} = x \tag{3.23a}$$

$$X_{p,2} = y \tag{3.23b}$$

$$X_{s,1} = \frac{N_1}{x D} \tag{3.23c}$$

$$X_{s,2} = \frac{N_2}{y D} \tag{3.23d}$$

with

$$N_1 = \mathrm{Re}\{Z_m - Z_{L,max}\}x^2 y - 2\mathrm{Im}\{Z_m\}\mathrm{Re}\{Z_{L,max}\}xy$$
$$- \mathrm{Im}\{Z_m Z_{L,max}^*\}x^2 - \mathrm{Re}\{Z_{L,max}\}|Z_m|^2\,(x+y)$$

$$N_2 = \mathrm{Re}\{Z_{L,max} - Z_m\}xy^2 - 2\mathrm{Im}\{Z_{L,max}\}\mathrm{Re}\{Z_m\}xy$$
$$+ \mathrm{Im}\{Z_m Z_{L,max}^*\}y^2 - \mathrm{Re}\{Z_m\}|Z_{L,max}|^2\,(x+y)$$

$$D = \mathrm{Re}\{Z_{L,max}\}x + \mathrm{Re}\{Z_m\}y + \mathrm{Im}\{Z_m Z_{L,max}\}$$

Since (3.22) leads to two equations (if split in real and imaginary part), but the network itself comprises four parameters, two of them are freely selectable indicated by x and y (with the unit ohm).

It is stated that the input impedance Z_{in} for $Z_L = Z_{L,min}$ (i.e. $Z_{in}|_{Z_L=Z_{L,min}}$) must be as high as possible to minimize the power in $Z_{L,min}$. From here, the real part of Z_{in} is considered only, because the imaginary part will be compensated when two ITNs are combined forming the power divider (see the following subsection). The Fig. 3.14 (a) colourmap shows the real part of Z_{in} if the ITN is terminated in $Z_{L,min}$ for different values of x and y. Dark red gives the maximum value, whereas dark blue indicates a low value with the unit ohm. Here, example values for $Z_{L,min}$ and $Z_{L,max}$ are chosen deliberately. It is calculated with (3.23) and consequently fulfils (3.22). To find the

maximum values, following equation must be met

$$\nabla_{x,y}(\mathrm{Re}\{Z_{\mathrm{in}}|_{Z_{\mathrm{L}}=Z_{\mathrm{L,min}}}\}) = 0. \tag{3.24}$$

$\nabla_{x,y}$ indicates the gradient with respect to x and y. Both resulting equations are fulfilled for a certain dependency between x and y

$$x = \frac{\mathrm{T}_1 y^2 + \mathrm{T}_2 y + \mathrm{T}_3}{\mathrm{T}_4 y^2 + \mathrm{T}_5 y + \mathrm{T}_6} \tag{3.25}$$

where:

$$\mathrm{T}_1 = \mathrm{Re}\{Z_{\mathrm{m}}\}\left(\mathrm{Re}\{Z_{\mathrm{L,min}}\}^2 - \mathrm{Re}\{Z_{\mathrm{L,max}}\}^2 + \left(\mathrm{Im}\{Z_{\mathrm{L,min}}\} - \mathrm{Im}\{Z_{\mathrm{L,max}}\}\right)^2 + \sqrt{\mathrm{A}}\right)$$

$$+ 2\mathrm{Im}\{Z_{\mathrm{m}}\}\mathrm{Re}\{Z_{\mathrm{L,max}}\}\left(\mathrm{Im}\{Z_{\mathrm{L,min}}\} - \mathrm{Im}\{Z_{\mathrm{L,max}}\}\right) \tag{3.26a}$$

$$\mathrm{T}_2 = 2|Z_{\mathrm{L,max}}|^2\left(\mathrm{Im}\{Z_{\mathrm{L,max}}Z_{\mathrm{m}}^*\} - 2\mathrm{Re}\{Z_{\mathrm{m}}\}\mathrm{Im}\{Z_{\mathrm{L,min}}\}\right) \tag{3.26b}$$

$$+ 2|Z_{\mathrm{L,min}}|^2\mathrm{Im}\{Z_{\mathrm{m}}Z_{\mathrm{L,max}}\} + 2\mathrm{Im}\{Z_{\mathrm{L,max}}\}\mathrm{Re}\{Z_{\mathrm{m}}\}\sqrt{\mathrm{A}}$$

$$\mathrm{T}_3 = \mathrm{Re}\{Z_{\mathrm{m}}\}|Z_{\mathrm{L,max}}|^4 - \mathrm{Re}\{Z_{\mathrm{m}}\}\mathrm{Re}\{Z_{\mathrm{L,max}}^2\}|Z_{\mathrm{L,min}}|^2 + \mathrm{Re}\{Z_{\mathrm{m}}\}\sqrt{\mathrm{A}}|Z_{\mathrm{L,max}}|^2 \tag{3.26c}$$

$$- 2\mathrm{Re}\{Z_{\mathrm{m}}\}\mathrm{Im}\{Z_{\mathrm{L,min}}\}\mathrm{Im}\{Z_{\mathrm{L,max}}\}|Z_{\mathrm{L,max}}|^2$$

$$- 2\mathrm{Im}\{Z_{\mathrm{m}}\}\mathrm{Re}\{Z_{\mathrm{L,max}}\}\left(\mathrm{Im}\{Z_{\mathrm{L,min}}\}|Z_{\mathrm{L,max}}|^2 - \mathrm{Im}\{Z_{\mathrm{L,max}}\}|Z_{\mathrm{L,min}}|^2\right)$$

$$\mathrm{T}_4 = 2\mathrm{Re}\{Z_{\mathrm{L,max}}\}\left(\mathrm{Im}\{Z_{\mathrm{L,max}}\} - \mathrm{Im}\{Z_{\mathrm{L,min}}\}\right) \tag{3.26d}$$

$$\mathrm{T}_5 = 2\mathrm{Re}\{Z_{\mathrm{L,max}}\}\left(|Z_{\mathrm{L,max}}|^2 - |Z_{\mathrm{L,min}}|^2\right) \tag{3.26e}$$
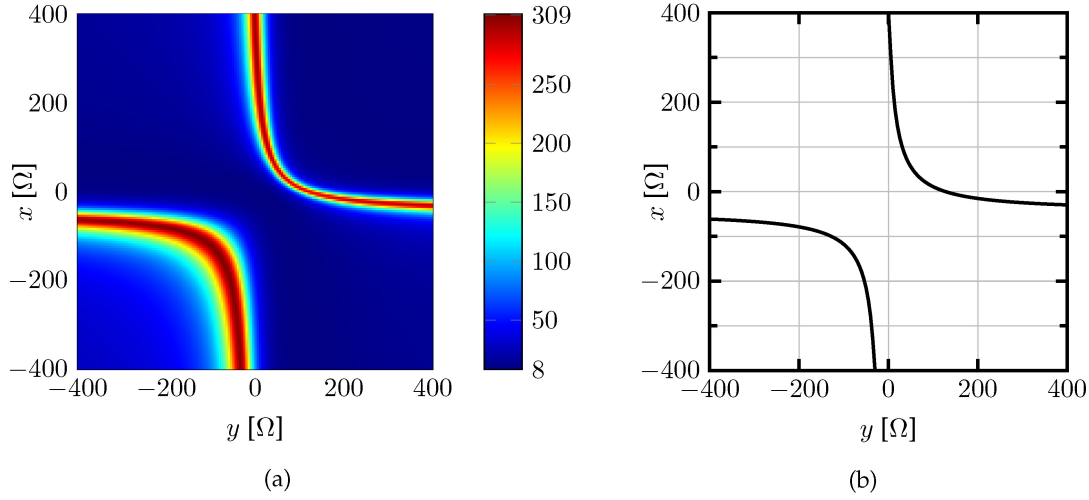
FIGURE 3.14:   (a) colourmap of $\mathrm{Re}\{Z_{\mathrm{in}}|_{Z_{\mathrm{L}}=Z_{\mathrm{L,min}}}\}$ over x and y (see (3.23)) with $Z_{\mathrm{L,min}} = 20 + \mathrm{j}10$ [Ω] and $Z_{\mathrm{L,max}} = 70 - \mathrm{j}50$ [Ω] arbitrarily chosen. This map is calculated with (3.23). Dark red indicates the maximum value while dark blue gives the minimum value in [Ω]. It should be noted that for $Z_{\mathrm{in}}|_{Z_{\mathrm{L}}=Z_{\mathrm{L,max}}}$ (3.22) is fulfilled for all values of x and y.
(b) plotted function of (3.25) for the same example as in (a). This curve gives the relation between x and y to obtain the highest possible value of the real part of $Z_{\mathrm{in}}|_{Z_{\mathrm{L}}=Z_{\mathrm{L,min}}}$. At the same time (3.23) for $Z_{\mathrm{in}}|_{Z_{\mathrm{L}}=Z_{\mathrm{L,max}}}$ is fulfilled. This curve can be recognized as the maxima of the colourmap in (a) [74].

$$\mathrm{T}_6 = 2\mathrm{Re}\{Z_{\mathrm{L,max}}\}\left(\mathrm{Im}\{Z_{\mathrm{L,min}}\}|Z_{\mathrm{L,max}}|^2 - \mathrm{Im}\{Z_{\mathrm{L,max}}\}|Z_{\mathrm{L,min}}|^2\right) \tag{3.26f}$$

with

$$\mathrm{A} = \left(\mathrm{Im}\{Z_{\mathrm{L,min}}\} - \mathrm{Im}\{Z_{\mathrm{L,max}}\}\right)^4 + \left(\mathrm{Re}\{Z_{\mathrm{L,min}}\}^2 - \mathrm{Re}\{Z_{\mathrm{L,max}}\}^2\right)^2$$
$$+ 2\left(\mathrm{Re}\{Z_{\mathrm{L,min}}\}^2 + \mathrm{Re}\{Z_{\mathrm{L,max}}\}^2\right)\left(\mathrm{Im}\{Z_{\mathrm{L,min}}\} - \mathrm{Im}\{Z_{\mathrm{L,max}}\}\right)^2$$

Inserting (3.25) into (3.23) gives the solution that fulfils the aforementioned properties of the ITN. For the same example of Fig. 3.14 (a) the relation between x and y of (3.25) is plotted in Fig. 3.14 (b). The curve can be recognized in Fig. 3.14 (a) as the maxima. Furthermore, by using (3.17), the characteristic impedances as well as the electrical lengths of the two TLs, which form the ITN, can be obtained.
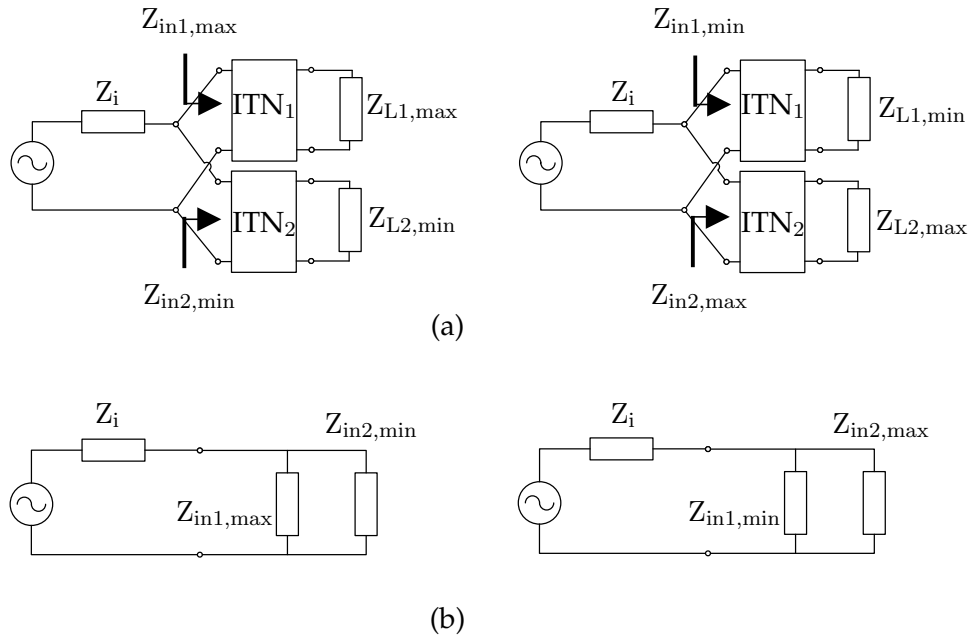
FIGURE 3.15: The scheme of the power divider network (PDN). (a) An illustration of the PDN comprising two impedance transformation networks (ITN) in parallel with its two scenarios. (b) The equivalent circuit of the PDN with its two scenarios [74].

3.3.1.3 Power Divider Network

Two of the ITN described above form a three-port power divider network (PDN). As shown in Fig. 3.15 (a), the two scenarios (with source and PDN unchanged) have different loads, Z_{L1} and Z_{L2}. These loads are transformed through the ITNs, and the simplified circuits of Fig. 3.15 (b) are obtained. Here, the subscript "max" indicates the load where the dissipated power is maximized, and the subscript "min" indicates the load where the dissipated power is minimized. For example, $Z_{in,max}$ denotes the input impedance of the ITN connected to the load $Z_L = Z_{L,max}$ for the scenario where the maximum power should be delivered to this load. From the circuits of Fig. 3.15 (b), conjugate-complex match to the source impedance Z_i gives

$$Z_i^* = \frac{Z_{in1,max} Z_{in2,min}}{Z_{in1,max} + Z_{in2,min}} \tag{3.27a}$$

$$Z_i^* = \frac{Z_{in1,min} Z_{in2,max}}{Z_{in1,min} + Z_{in2,max}} \tag{3.27b}$$

which can be written as

$$Z_{\text{in1,max}} = Z_{\text{m1}}^* = \frac{Z_i^* Z_{\text{in2,min}}}{Z_{\text{in2,min}} - Z_i^*} \tag{3.28a}$$

$$Z_{\text{in2,max}} = Z_{\text{m2}}^* = \frac{Z_i^* Z_{\text{in1,min}}}{Z_{\text{in1,min}} - Z_i^*} \tag{3.28b}$$

The two equations of (3.28) have unknowns $Z_{\text{in1,max}}$, $Z_{\text{in2,max}}$, $Z_{\text{in1,min}}$, $Z_{\text{in2,min}}$. In addition, (3.22) and (3.24) relate $Z_{\text{in,max}}$ and $Z_{\text{in,min}}$ for each of the two ITNs. Therefore, this system of equations can be solved numerically and parameters of the TLs can be calculated.

The PDN presented here is a way of solving the problem of two different environments around an antenna. Intuitively, an alternative approach would be to use only one feed point of the antenna which is then matched with only one ITN for two load impedances (two different environments). However, the design of such a network is not straightforward due to the impedance matching domain problem as discussed in [209] for LC ladder networks. Thus, this single-feed approach is not suitable for a generalized case. On the other hand, the proposed dual-fed approach is straightforward, as shown in the following example.

3.3.2   Example

The procedure developed in the previous subsections is applied to a practical example of an adaptive antenna. The idea is to use the PDN to feed two monopoles (diameter of $2\,\text{mm}$) of different length, very close to each other ($\approx \lambda/15$) at $1\,\text{GHz}$ (Fig. 3.16 (a)). Here, "M1" indicates monopole 1 (length $72\,\text{mm} \approx \lambda/4$) and "M2" monopole 2 (length $35\,\text{mm} \approx 0.116\lambda$). In the first scenario, the monopoles are placed in free space. In the second scenario, the monopoles are fully immersed in a lossy organic material (namely, butter). This example setup of the two coupled monopole antenna was chosen because it allows for an easy and clear separation of the electromagnetic environment of the antenna (namely, "air" versus "butter") from the PDN (the microstrip circuit in the opposite side of the antenna ground plane). The PDN matches the monopoles, in both

(a)   (b)
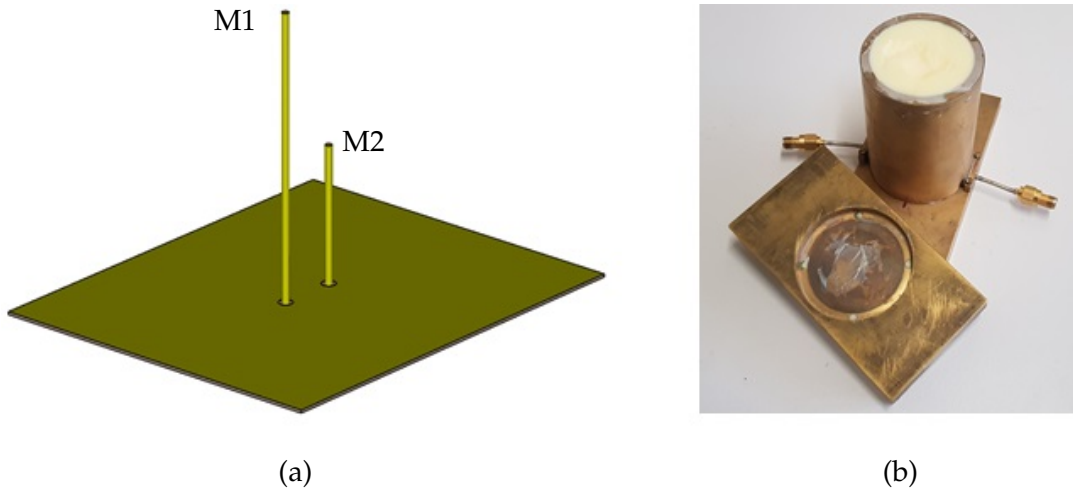
FIGURE 3.16: (a) Two monopoles of different length next to each other forming the dual-fed adaptive antenna. (b) Photo of the butter-filled cylindrical resonator (opened for clarity) for determination of the material properties of butter [74]

TABLE 3.2: Simulated input impedances of the monopoles [74].

Scenario 1	Free-space	
Notation	$Z_{L1,max}$ [Ω]	$Z_{L2,min}$[Ω]
1st simulation	$24.1 + j1.2$	$2.6 - j113$
converged	$25 + j1.7$	$-35.5 - j162.1$
Scenario 2	Butter	
Notation	$Z_{L1,min}$ [Ω]	$Z_{L2,max}$[Ω]
1st simulation	$56.9 - j102.1$	$12.3 + j8.9$
converged	$-33.4 - j53.6$	$14.9 + j8.4$

scenarios, to a single $50\,\Omega$ source. From inspection of field simulation field plots, it can be noted that in the first scenario (free space), most of the power is radiated via the first monopole, while in the second scenario (butter), mostly the second monopole radiates.

The dielectric properties of butter are measured. Transmission through a cylindrical cavity resonator, at first air-filled and then filled with butter (Fig. 3.16 (b)) is measured and modeled in a field simulator, allowing to obtain permittivity and loss tangent by fitting. Permittivity $\epsilon_{r,butter} = 4.13$ and $\tan \delta_{butter} = 0.04$ is found at $1\,\text{GHz}$.
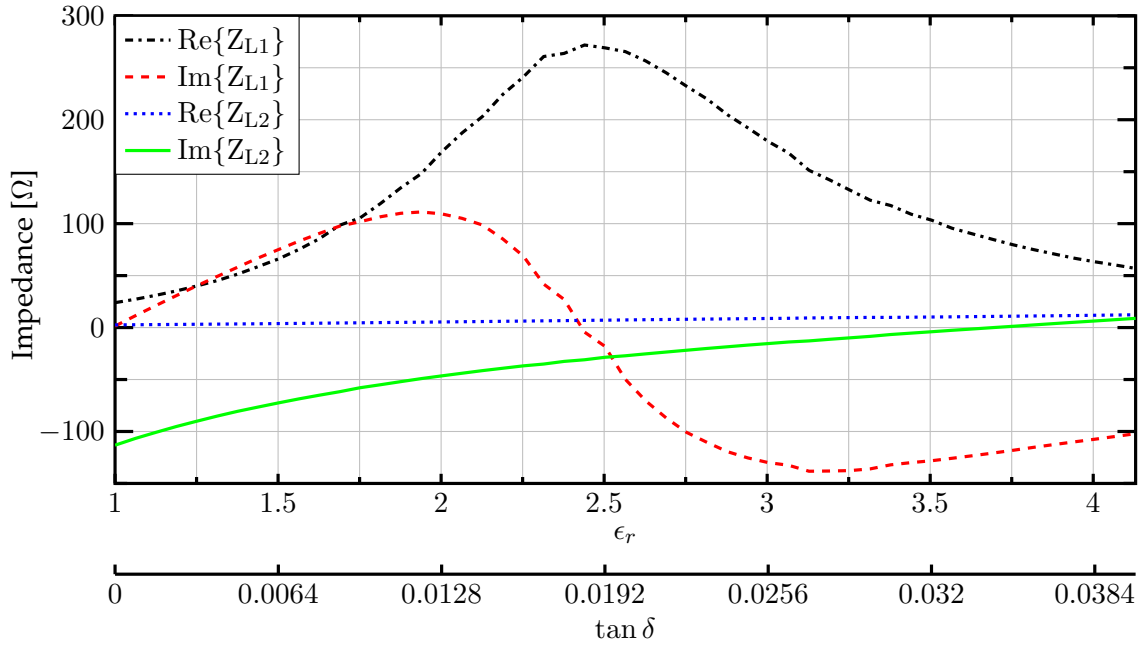
FIGURE 3.17: Simulated input impedance of the two monopoles when assuming a linear transition of the relative permittivity and loss tangent from the scenario with air to the one with butter. It holds $Z_{L1}(\epsilon_r = 1, \tan\delta = 0) = Z_{L1,max}$, $Z_{L2}(1,0) = Z_{L1,min}$, $Z_{L1}(4.13, 0.04) = Z_{L1,min}$ and $Z_{L2}(4.13, 0.04) = Z_{L2,max}$ [74]

TABLE 3.3: Characteristic impedances and electrical lengths of the PDN transmission lines for $y = -5\,\Omega$ [74].

Z_{11}	Z_{12}	Z_{21}	Z_{22}	Φ_{11}	Φ_{12}	Φ_{21}	Φ_{22}
			1st simulation				
	[Ω]				[°]		
41.3	28.5	125.8	58	88.4	80	79.3	85
			converged				
	[Ω]				[°]		
46.7	33.3	96.9	56.5	77.8	81.5	82.0	84.8

Field simulation provides the respective input impedances for the two monopoles M1, M2 for the two scenarios, as listed in Table 3.2 under notation "1st simulation". The indices are chosen such that M1 is primarily fed to radiate in the free-space scenario, whereas M2 is primarily fed to radiate in the "butter scenario". For illustration, Fig. 3.17 shows plots of the variation of the monopole input impedances while linearly varying permittivity and loss tangent from the values of the first scenario to their values of the second scenario.

It should be noted that strong coupling between the two monopoles (also expected for most dual-fed antenna structures) leads to some change of feed impedance of one monopole while the other monopole's feed is connected to a varying load (active impedance). The PDN is derived from the impedances, which in turn are obtained from a field simulation assuming simple, e.g., $50\,\Omega$, port impedance. This PDN, however, then provides different impedances to the antenna, changing the active impedances of the antenna network at its ports. In an iterative procedure, these updated antenna impedances allow to derive an updated PDN. This process converges quickly as can be seen in Fig. 3.18. (a) and (b) shows the input impedances of both monopoles over the iterations, which are the load impedances of the PDN. The TL parameters over the iterations is given in (c) and (d). Note that additional field simulations are not required, as the scattering parameter matrix (or impedance matrix) of the antenna (for each scenario) needs to be obtained only at the beginning.

Table 3.2 lists under notation "converged" the respective input impedances of the two monopoles M1, M2 for the two scenarios. Using the input impedances of Table 3.2, equations $(3.17)-(3.28)$ permit the calculation of impedances and electrical lengths of the TLs forming the ITNs (Fig. 3.19, Table 3.3). These calculations are executed with Matlab. For each ITN, a remaining degree of freedom allows to select one parameter. In this example, the parameter $y = -5\,\Omega$ is chosen for each ITN (this choice is governed by the resulting, "realizable" TL impedances).

Table 3.3 lists the obtained parameters of the TLs of the PDN. The values for the PDN of the first iteration (notation "1st simulation") do not differ much from the values obtained from the converged iterative design process (notation "converged"). In particular, in a practical realization of the PDN in microstrip technology, the differences

(a) Real part

(b) Imaginary part

(c) Characteristic impedance
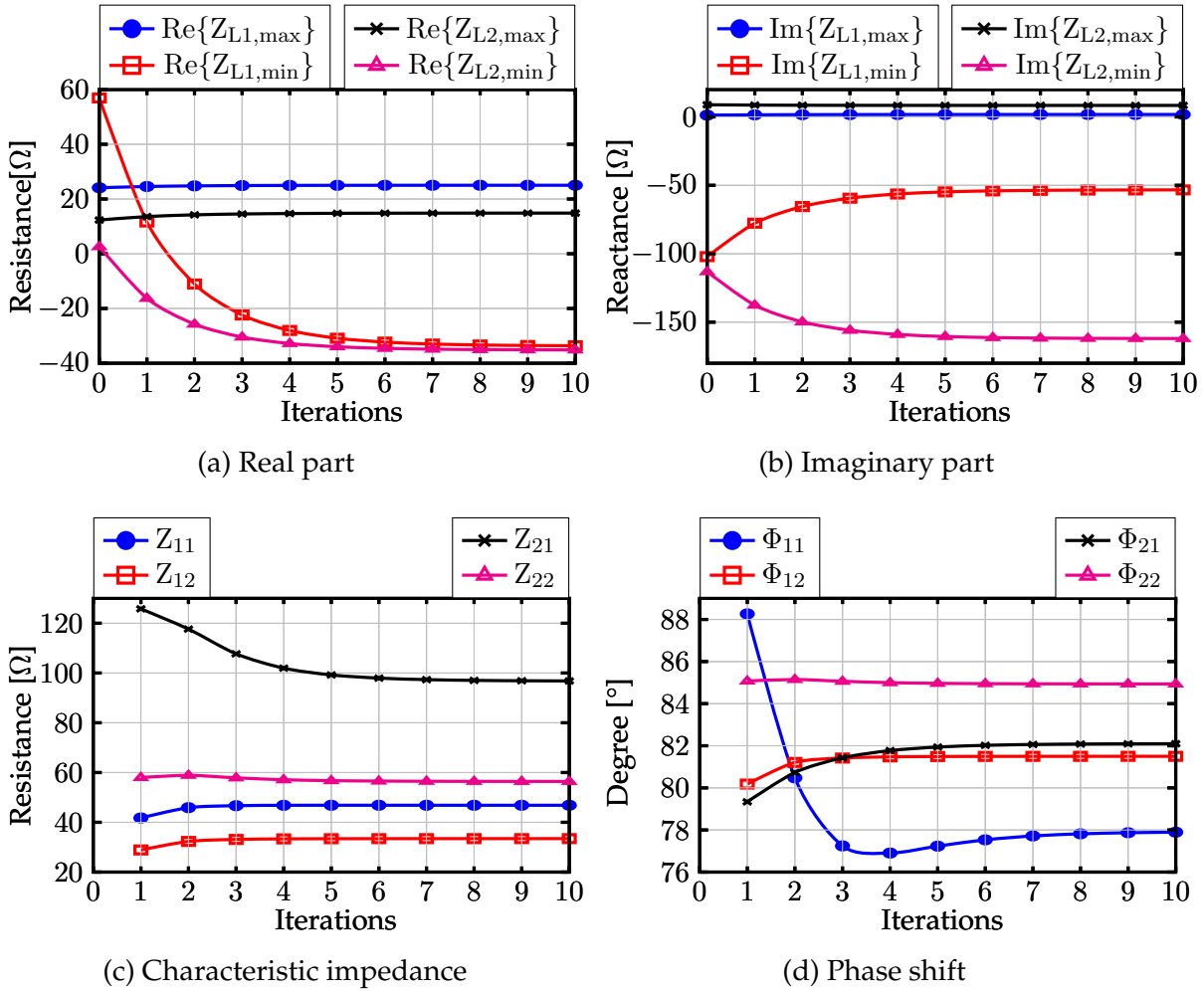
(d) Phase shift

FIGURE 3.18: The behaviour of the input impedances of the monopoles ((a) real and (b) imaginary part) and the characteristic impedance (c) and phase shift (d) of the TLs of the PDN over the iteration steps.

will be negligible. However, for an even-stronger coupling between the ports of the dual-fed antenna, the changes during the iterative design procedure may become larger.

In Fig. 3.20 the simulated (here, TLs are lossless) portions of the maximum power that can be delivered from the source of the reflected power $|\Gamma|^2$ (black dash-dotted line), the power dissipated in $\mathrm{Re}\{Z_{L1}\}$ (p_1 red dashed line) and the dissipated power in $\mathrm{Re}\{Z_{L2}\}$ (p_2 blue dotted line) are plotted. Thereby, the input impedance changes over the relative pemittivity and the loss tagent is considered (see Fig. 3.17). In the air-scenario, 99.8 % of the maximum power is consumed by monopole M1, while only 0.2 % is dissipated in monopole M2. If the monopoles are exposed in butter, the
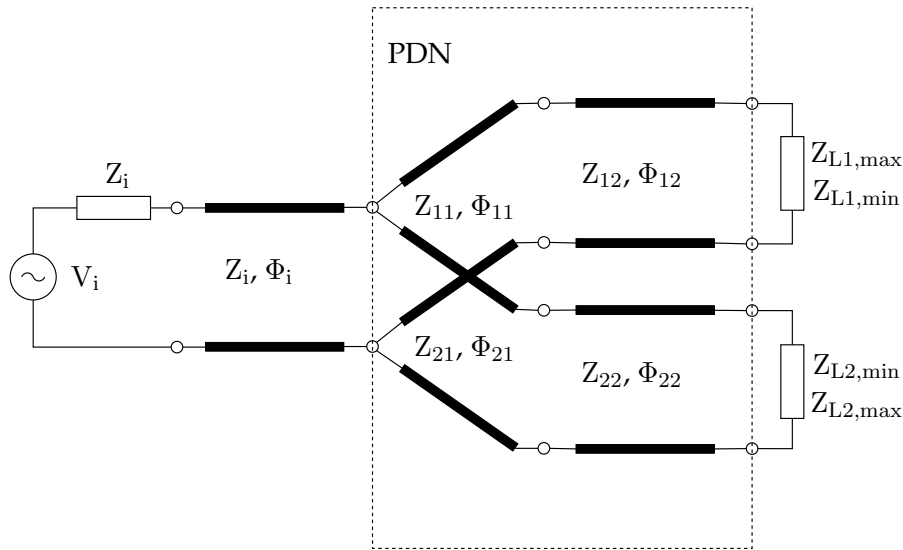
FIGURE 3.19: Equivalent circuit of the PDN with TL parameters [74].

reflected power is about 0.2 %, the power in M1 is 9.5 % and in M2 is 90.3 %.

So far, optimum operation was required at two different scenarios, as illustrated in Fig. 3.20, showing the reflected power at source becoming zero for $\epsilon_r = 1$ and $\epsilon_r = 4.13$. A modification of the use-case may require good performance (that is, small reflected power) over a range of dielectric property of the electromagnetic environment. Such use-case may represent somewhat varying material property and/or varying geometry of the environment of the antenna, as it can be expected for many RFID-like applications.

Exposing the pair of coupled monopole radiators to three other pairs of environmental dielectric scenarios, Fig. 3.21 illustrates the simulated resulting reflection coefficient magnitude. The four permittivity-pairs related to Fig. 3.21 are: (i) $\epsilon_r = \{1, 4.13\}$, (ii) $\epsilon_r = \{1.5, 3.5\}$, (iii) $\epsilon_r = \{2, 3\}$, (iv) $\epsilon_r = \{2.25, 2.75\}$. Obviously, the dielectric property of the electromagnetic environment can always vary by a small amount, without resulting in large mismatch. Once the two "optimally matched" permittivity values are close-enough to each other (as in cases (iii) and (iv)), a range of electromagnetic environment, leading well-matched input impedance, is obtained. Similar behavior is common to any impedance-transformation network.
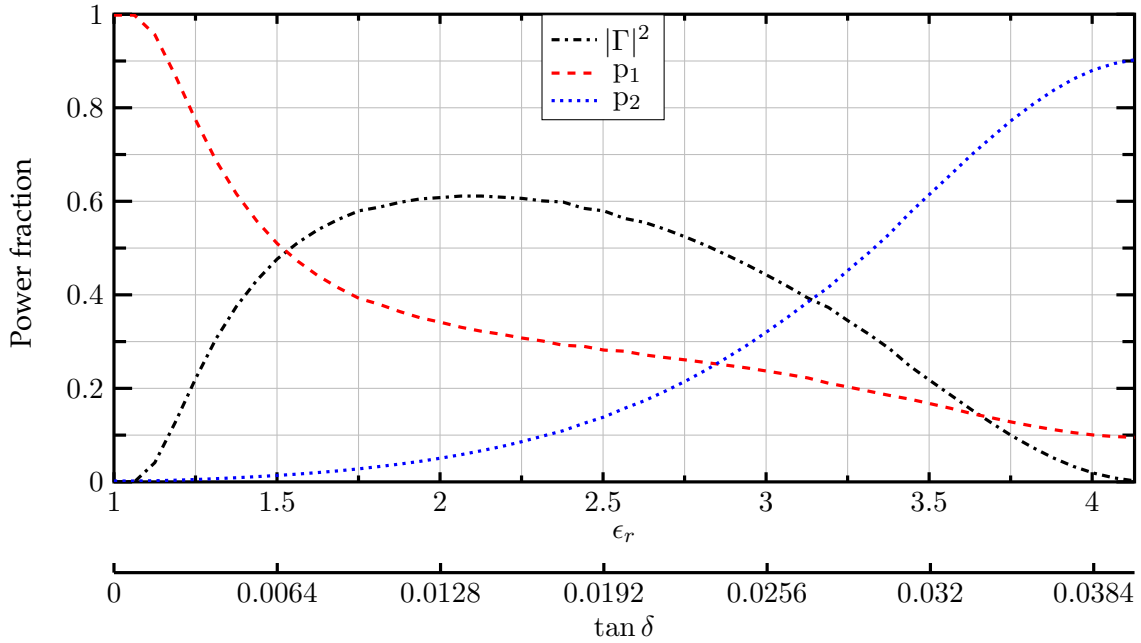
FIGURE 3.20: Simulated portions of the maximum power of the reflected power $|\Gamma|^2$ (black dash-dotted line), the power dissipated in $\mathrm{Re}\{Z_{L1}\}$ (p_1, red dashed line) and dissipated power in $\mathrm{Re}\{Z_{L2}\}$ (p_2, blue dotted line) over different valuesets of the relative permittivity and the loss tagent. In the scenario where the monopoles are placed in air ($\epsilon_r = 1$, $\tan\delta = 0$) the reflected power is zero and the dissipated power p_1 in $\mathrm{Re}\{Z_{L1}\}$ is about 99.8 % of the maximum power that can be delivered from the source. Then the power p_2 in $\mathrm{Re}\{Z_{L2}\}$ is 0.2 %. In the scenario of butter ($\epsilon_r = 4.13$, $\tan\delta = 0.04$) $|\Gamma|^2$ is 0.2 %, p_1 is 90.3 % and p_2 is 9.5 % [74].

The microstrip line parameters are readily found for the circuit realized on Rogers RT6002 substrate (thickness $0.762\,\mathrm{mm}$, $\epsilon_{\mathrm{rel}} = 2.94$, $\tan\delta = 0.0012$). Figure 3.22 shows the realization of the two monopole radiators and the PDN on a microstrip circuit board. The ground layer has openings of $4\,\mathrm{mm}$ diameter for the monopoles. The monopole metal rods pass through the board and are soldered to the microstrip traces. The feed reflection magnitude at the coax connector, measured for the two scenarios, is shown in Fig. 3.23. Good match is achieved for both scenarios (free-space and butter). Furthermore, the measured curves are in good agreement with the field simulations. Figure 3.24 shows a photograph of the reflection coefficient measurement setup when the monopoles are immersed into butter.
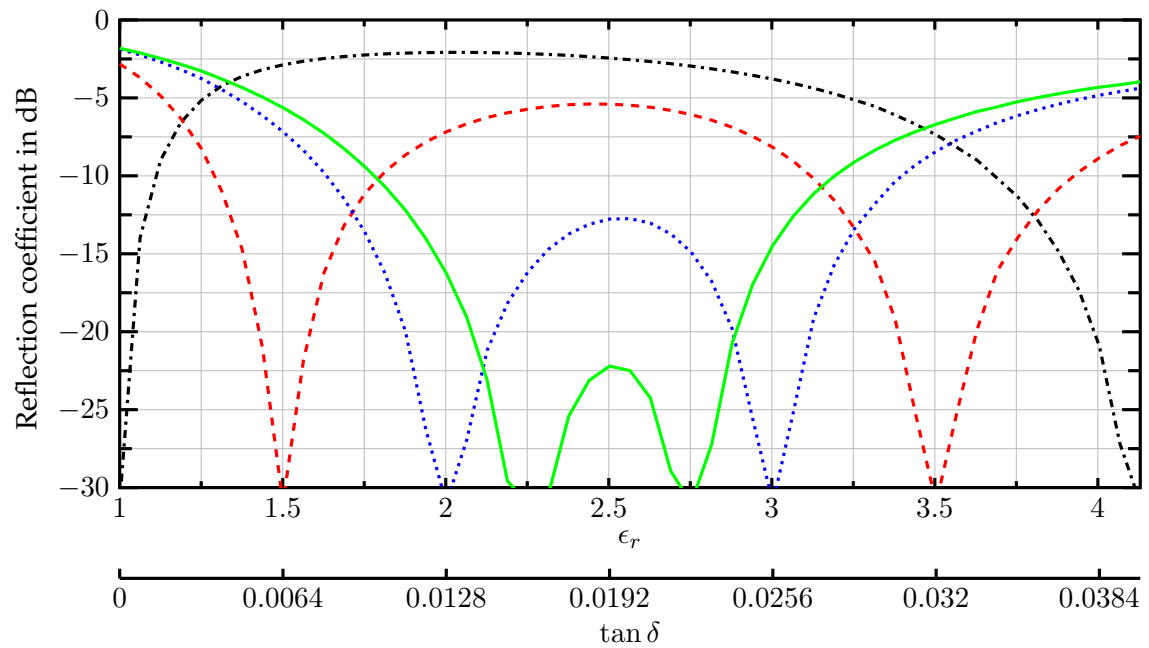
FIGURE 3.21: Simulated reflection coefficient $|\Gamma|$ in dB for the two-monopole-antenna with four different PDNs, corresponding to four pairs of scenarios to the antenna. Case (i): $\epsilon_r = \{1, 4.13\}$ in black dash-dotted line. Case (ii): $\epsilon_r = \{1.5, 3.5\}$ in red dashed line. Case (iii): $\epsilon_r = \{2, 3\}$ in blue dotted line. Case (iv): $\epsilon_r = \{2.25, 2.75\}$ in green solid line. The associated loss tangent ($\tan \delta$) values are scaled proportionally [74].
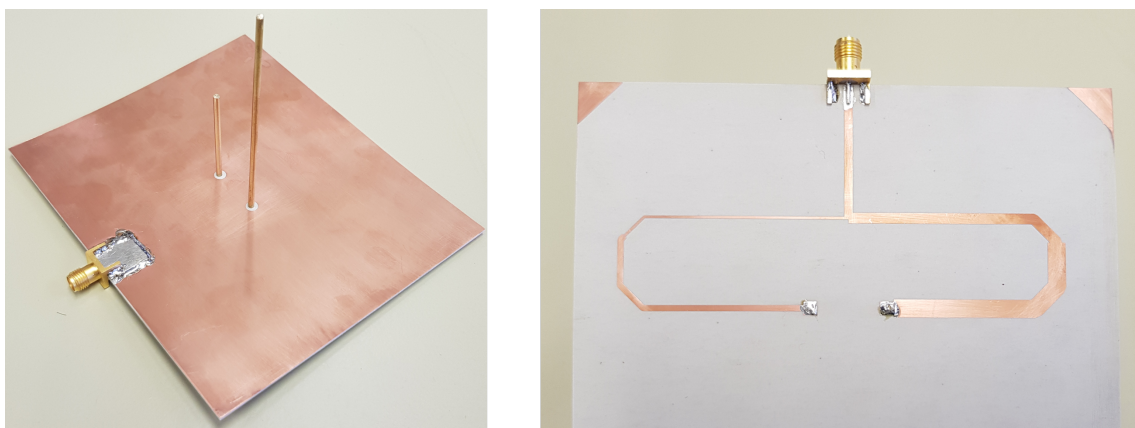
FIGURE 3.22: Photograph of the prototype: Left: The two monopoles over ground plane. Right: The PDN.
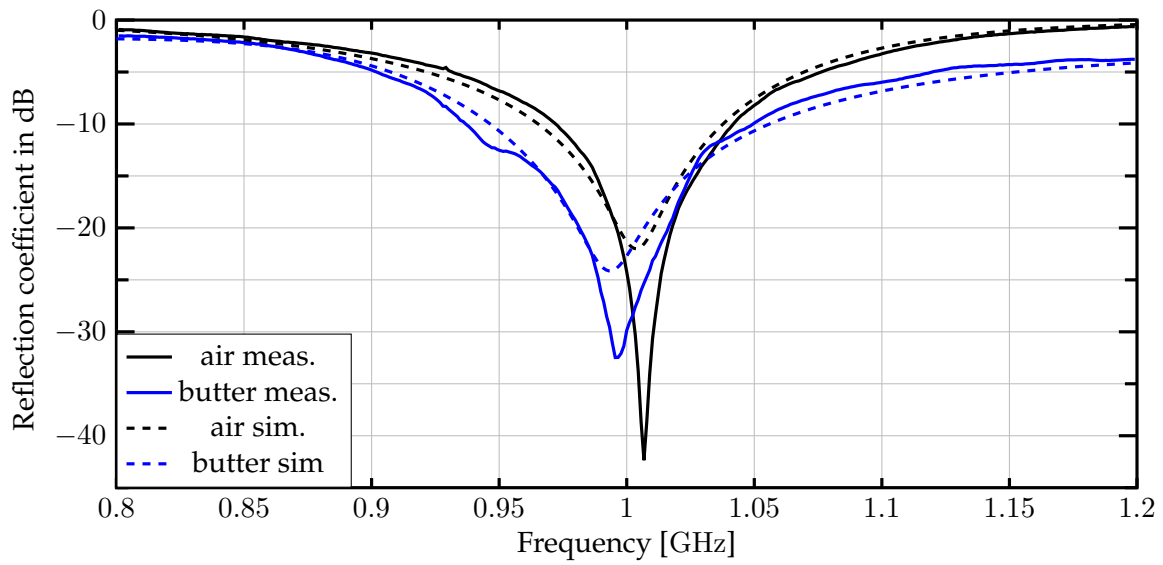
FIGURE 3.23: Measured and simulated reflection coefficient of the adaptive antenna for both scenarios (air and butter) [74].
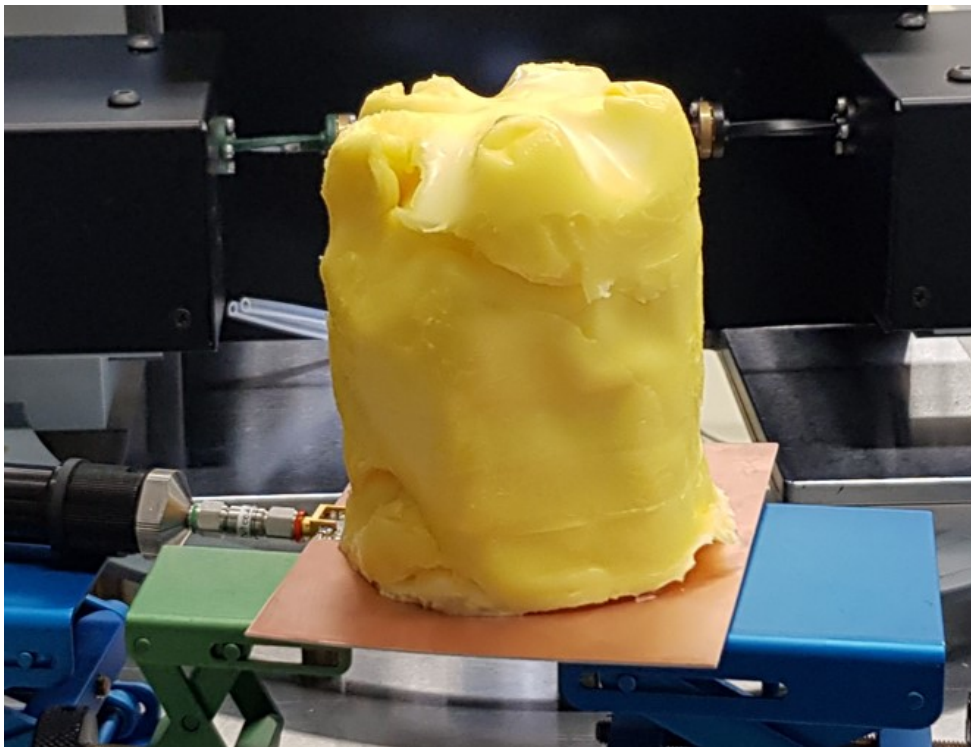
FIGURE 3.24: Photograph of the measurement setup when the monopoles are immersed into butter.

3.3.3 Discussion

Analytical formulae for a power divider feed network for a dual-fed antenna are presented. If the antenna operates in two electromagnetically different environments, called scenarios, its feed impedances will change. The proposed power divider feed network directs the power from a matched source to the first antenna feed in the first scenario, and to the second antenna feed in the second scenario. The proposed power divider feed network is passive and assumed lossless. In a practical demonstration, two strongly coupled monopole radiators of largely different length are fed by an accordingly designed power divider feed network. This structure radiates with perfect source match (50 ohm) into free space, but also when completely immersed into butter ($\epsilon_{\mathrm{r,butter}} = 4.13$, $\tan \delta_{\mathrm{butter}} = 0.04$). The measurements confirm the derived theoretical formulae.

The presented power divider network can be used with RFID tags to adapt the antenna to two different environments. It ensures an energy-efficient operation of the RFID tag without much power being reflected at the antenna input.

From a theoretical point of view, the number different environmental scenarios, as well as the number of antenna feed points, can both be increased to a number larger than two. If N scenarios shall be covered with an antenna having N feed points, then the extension of the approach discussed in this paper (here N = 2) shows that each of the N arms of the power divider requires N sections of transmission line to realize the appropriate impedance transformation. However, already for N = 3, these 9 lines contribute to loss and increase the physical size of the circuit likely beyond a practical limit.

Chapter 4

Actively Adaptive Antennas

4.1   Introduction

Two concepts of actively adaptive antennas are introduced in this chapter. These
do require active components such as diodes or transistors. When the environment
changes, switching events are triggered by a DC voltage that changes the radiating
structure in such a way that impedance matching to the source(s) is maintained.
The second section shows a concept that alters the feed location along a differential
antenna upon the scenario. Thereby, the feed location where impedance matching
prevails is selected with the help of switches. In the third section, a theory of a radiation
structure, represented by a multi port with an arbitrary number of feed and load ports
is introduced. At each load port, an admittance can be activated using a switch to
obtain impedance matching at all feed ports. This can only be the case if the admittance
has a certain value, which is provided by this theory.

4.2   Adaptivity by Changing Feed Positions Along A Wire Antenna[1]

In the following approach the variation of the input impedance along a wire antenna
is exploited. It is assumed that the antenna is placed on different materials over time.

---

[1]Some of the text and pictures presented in this section are extracted (or are modified versions) from
[153, 210]. The author is the main contributor to publication [153, 210].
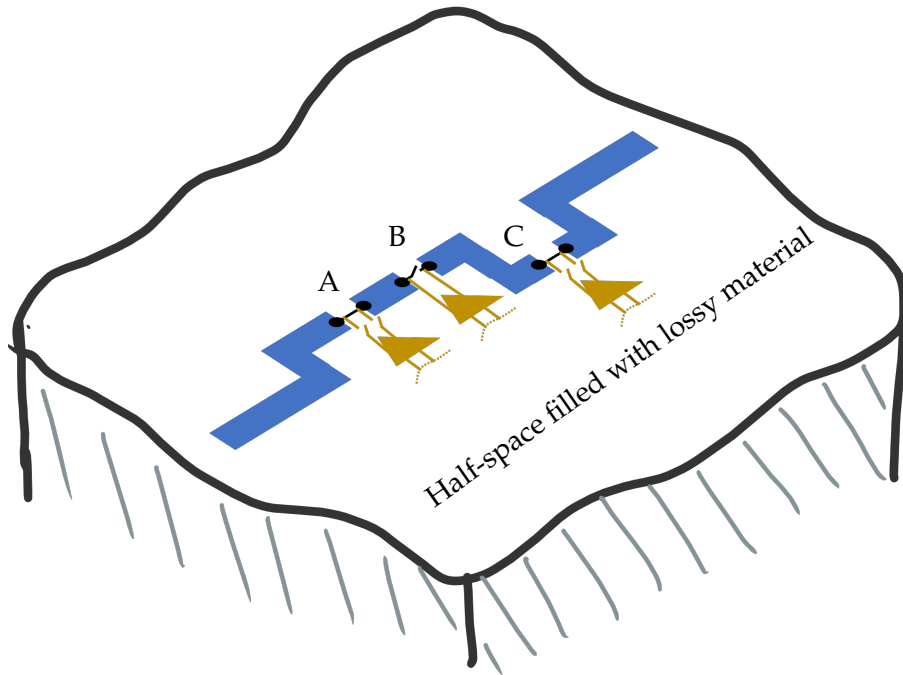
FIGURE 4.1: Planar wire antenna with arbitrary shape and three different feed positions (A, B and C) on a half-space filled with lossy material.

Thereby, the antenna is laid on a half-space made of said materials while the other half-space always consists of air. A specific time with a specific material is called a scenario. For each scenario there is a specific input impedance distribution along the antenna. The idea is to find the feed position where complex conjugate impedance matching to the source is achieved. If the scenario changes now, the suitable feed position will change as well. Consequently, for a certain number of scenarios different feed positions can be found. By incorporating switches the appropriate feed position per scenario can be selected. In Fig. 4.1 a sketch of a planar wire antenna with arbitrary shape and three different feed positions (A, B and C) on a half-space filled with an arbitrary material is depicted. This has three transceivers of which one per scenario connects to the antenna, while the other ones are excluded by switches from the radiating structure. Thus, an antenna can be designed that is adaptive to different scenarios, even if the materials show largely different properties like losses and dielectric constants.

4.2.1   Differential Feed Structures

In [211] numerical investigations on a multiple fed dipole antenna are conducted in order to show the proof of concept. Indeed, it has been shown that a certain range of the dielectric constants can be covered with two switches. Thereby, the reflection coefficient at the respective feed always stays below a certain limit (e.g. -8.5 dB). If it comes to the realization of a prototype antenna that is connected to an RF-chip, in which the switching functionality is implemented two problems appear:

The first one is the radiation of the feed line. This radiation occurs if the feed position is not in the symmetric plane of the wire antenna. This effect was described as early as 1950 [212], where it is stated: "*Most important is the fact that a transmission line feeding the antenna [. . .] is not in a neutral plane and is unbalanced by the different lengths of conductor attached to its ends. As a result, the transmission line is an important part of the radiating systems since the co-directional components of current contribute significantly to the far-zone electromagnetic field.*"

The second problem that occurs is the small area of the RF-chip in comparison to the antenna dimensions. Different from as shown in Fig. 4.1, in a prototype the feeds are not distributed as it would be necessary for the feed positions. Rather, these are bundled next to each other in the small RF-chip area.

4.2.2   3-Port Antenna on Flexible Polymer Foil

In this subsection a planar single layer dipole-like antenna with three feeds is presented. The antenna is designed to be connected to an RF-chip, which are then embedded into a flexible polymer foil. The technique with a single feed bow-tie antenna has been demonstrated in [213–217]. Since the three antenna ports of the RF-chip are co-located within a $1.4\,\mathrm{mm}$ distance this prototype must overcome the aforementioned problems. The RF-chip operates at a center frequency of $5.5\,\mathrm{GHz}$ with a bandwidth of about $800\,\mathrm{MHz}$. With the three ports of the antenna three different scenarios can be perfectly covered, whereby the switching capability is implemented into the RF-chip. In order to select the appropriate feed port, a reflection coefficient detector should be developed within the RF-chip.
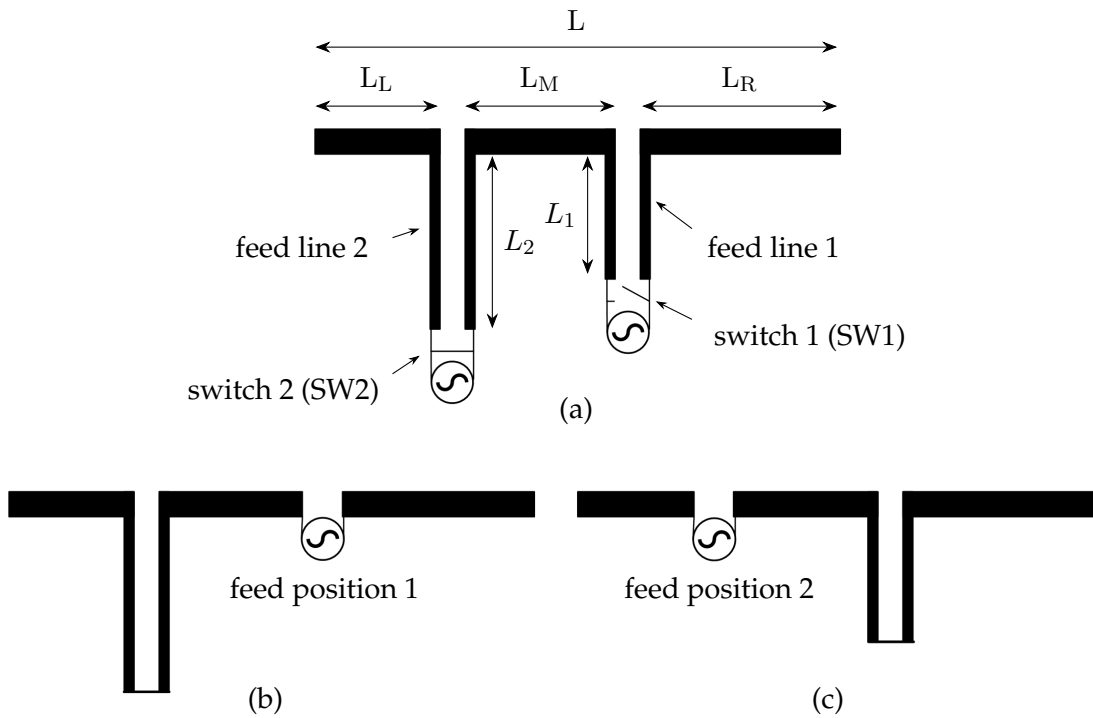
FIGURE 4.2: Double-fed dipole [153]. (a) Dipole with feed lines and switches. (b) Fed at feed-port 1, the feed line 1 is not part of the radiating structure. (c) Fed at feed-port 2.

4.2.2.1   Concept of the Antenna

For a decent bandwidth, a dipole-like structure (single-layer metal) is chosen. The antenna shall provide $100\,\Omega$ balanced feeds to the chip. Largely different environments (air, half-space of permittivity of 4 and of 42, respectively) would lead to largely different dipole sizes if three center-fed dipoles are considered. For compactness of the antenna structure, a co-integration of one double-fed dipole with an embraced second dipole is chosen.

A. Double-Fed Dipole

A double-fed dipole antenna is considered (Fig. 4.2 (a)) for the two scenarios with the lowest permittivity, air and butter (this will combine the two physically larger dipoles into a single structure, resulting in a compact device). Two switches (SW1 and SW2) are at the respective ends of feed lines 1,2, optionally short-circuiting source and line. For best feed match, the source 1 or 2 can be selected: Either SW1 is open and

SW2 is closed, or SW1 is closed and SW2 is open. By selecting the right feed-port, the double-fed dipole is resonant at the same frequency for different environments of different permittivity. The structural asymmetry with reference to either feed-port results in an even mode on the corresponding feed line. If the even mode on the feed line is suppressed, then the feedline itself does not radiate and consequently it does not belong to the radiating structure. As described in [218], the even mode can be suppressed by an appropriate load impedance at an arbitrary point along the dipole. The double-fed dipole can be seen, for one chosen feed-port, as an off-centre fed dipole loaded with a conductor stub at the other point. The two possible scenarios are depicted in Fig. 4.2 (b) and Fig. 4.2 (c). Assuming the first scenario is in air (Fig. 4.2 (b)), in which the dipole is fed at feed-port 1, the dipole length is:

$$L_{air} = L_L + 2L_2 + L_M + L_R = 2L_2 + L. \tag{4.1}$$

For the second scenario, the dipole is attached to a half-space of butter. The dipole is fed at feed-port 2 (Fig. 4.2 (c)) and the dipole length is calculated to

$$L_{butter} = L_L + 2L_1 + L_M + L_R = 2L_1 + L. \tag{4.2}$$

The condition of suppressing the even mode on the feed lines can be met as follows: Consider first an ordinary half-wavelength dipole that is fed in the middle has a symmetrical current distribution (Fig. 4.3 (a)). The current distribution is symmetric with reference to the feed point and thus there is no even mode on the feed lines. Consider now a full-wavelength dipole and its current distribution (Fig. 4.3 (b)). A feed point with symmetrical current is found one-quarter wavelength from the dipole end (Fig. 2b). Again, there will be no even mode on the feed line on that particular position, and the feed line can be assumed to not be part of the antenna. More generally, a series reactance placed in-series somewhere along the dipole will eventually modify the current distribution, so by doing so, the point where the current distribution becomes symmetric (and a feed-port with suppressed even mode should be connected) will displace [218].
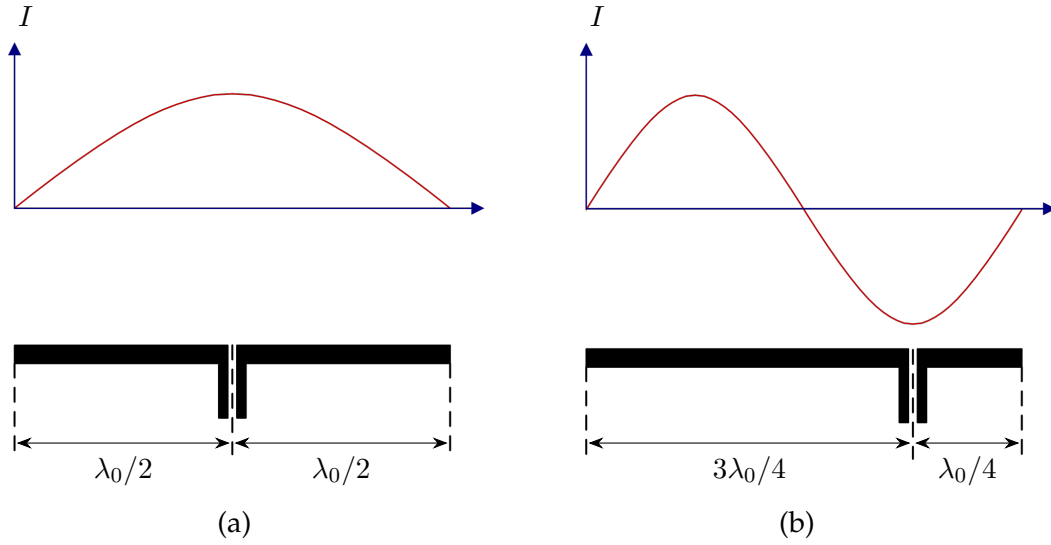
FIGURE 4.3: In order to suppress an even mode on the balanced feed line, the current distribution at the feed-point must be symmetrical. (a) Half-wavelength dipole and its current distribution. (b) a full-wavelength dipole fed at one fourth of the right end and its current distribution [218].

Accordingly, the following applies to the case, when the antenna is placed in air (feed-port 1):

$$L_R = \frac{\lambda_0}{4} \tag{4.3a}$$

$$L_L + 2L_2 + L_M = \frac{3\lambda_0}{4}. \tag{4.3b}$$

For the other case (antenna is place on a half-space of butter),

$$L_L = \frac{\lambda_0}{4\sqrt{\epsilon_{r,\text{eff,butter}}}} \tag{4.4a}$$

$$L_R + 2L_1 + L_M = \frac{3\lambda_0}{4\sqrt{\epsilon_{r,\text{eff,butter}}}}. \tag{4.4b}$$

Solving Eqs. (4.3) and (4.4) gives:

$$L_1 = \frac{1}{2} \left(\frac{\lambda_0}{\sqrt{\epsilon_{r,\text{eff,butter}}}} - L \right) \tag{4.5a}$$

$$L_2 = \frac{1}{2} \left(\lambda_0 - L \right). \tag{4.5b}$$

From this result it is obvious that the value of $\epsilon_{\text{r,eff,butter}}$ should be close enough to the dielectric constant of air that L_1 stays positive.

B. Separated Dipole

Since a triple-fed dipole antenna is too involved to design with the same approach presented in the previous section, the third scenario is covered by a third, separated dipole. As the third scenario belongs to the highest permittivity environment, this dipole is small. For overall compactness, this dipole is placed very close to the double-fed dipole and therefore strongly field coupled. Thus, field simulations optimize the shape of the separated dipole. Similar to the double-fed dipole, this dipole also features an on-chip switch, which is short-circuiting the feed line when not in use.

4.2.2.2 Standalone Prototype

Prior to the antenna simulation and design, the dielectric properties of the chosen dielectrics, butter and minced meat, are determined. The materials are placed into a section of rectangular waveguide (WR159) and reflection/transmission parameters are measured. Fig. 4.4 illustrates the procedure. In addition, an air-filled section is measured. All measurements are modelled in field simulation software and fitting simulations to measurements find the material dielectric parameters in the frequency range between $5\,\text{GHz}$ and $6\,\text{GHz}$. The extracted material properties are listed in Table 4.1.

Table 4.2 lists the geometries the balanced feed lines, attached onto blocks of the dielectric. The real part of the line characteristic impedance is chosen $100\,\Omega$, whereas the imaginary part is small (imaginary part of characteristic impedance for line-on-butter is $1.1\,\Omega$ and for line-on-meat $2.2\,\Omega$).

TABLE 4.1: Measured/extracted properties of the dielectric materials.

Parameters	Air	Butter	Minced meat
Dielectric constant	1	3.95	42
Loss tangent	0	0.05	0.37
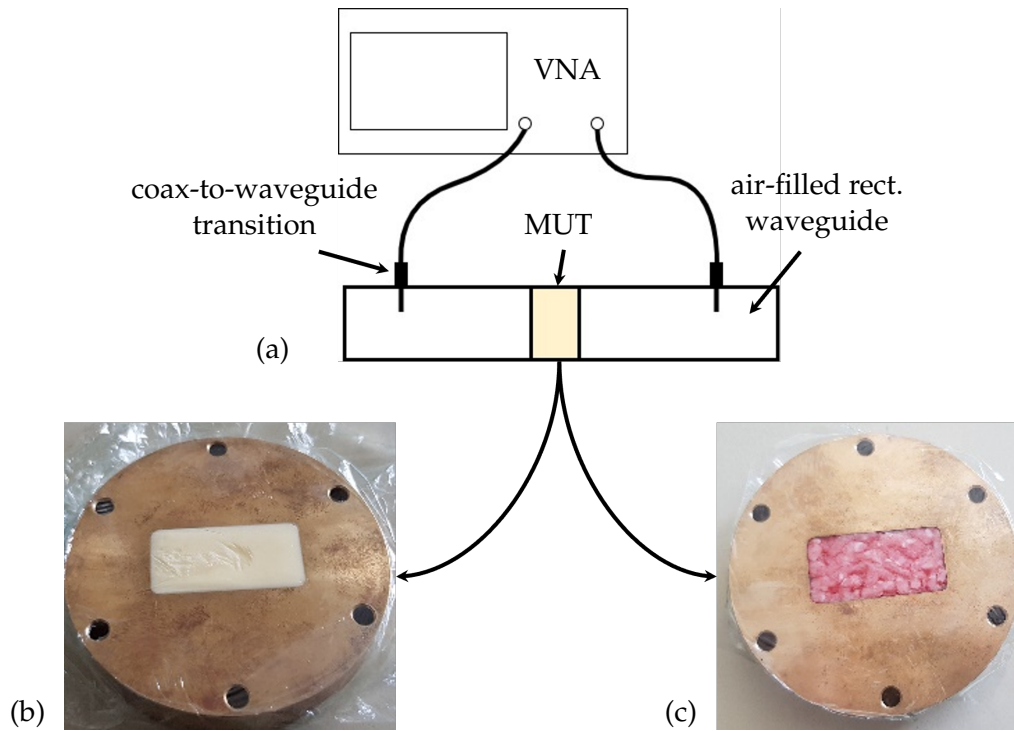
FIGURE 4.4: Measurement concept for dielectric material-under-test (MUT) [153]. WR159 waveguide. MUT section length $16.3\,\text{mm}$. (a) Schematic of the setup. (b) Butter-filled MUT section. (c) Minced meat-filled MUT section.

TABLE 4.2: Dimensions of $100\,\Omega$ differential lines (in foil) placed on top of dielectric block (half-space).

	Gap between strips g [µm]	Strip width w [µm]
Air	30	380
Butter	70	380
Butter	100	175

The dimensions from Eqs. (4.3), (4.4) and (4.5) give the starting point for the antenna design. Additionally, the length of the separated dipole is chosen to be half a wavelength at $5.5\,\text{GHz}$ in an effective medium with permittivity of $\epsilon_{\text{r,eff,meat}}$. The effective dielectric constant for the operation scenarios for butter and meat (note that these are dielectric half-spaces seen by the dipoles) is approximated by

$$\epsilon_{\text{r,eff,butter,meat}} = \frac{1 + \epsilon_{\text{r,butter,meat}}}{2}. \tag{4.6}$$
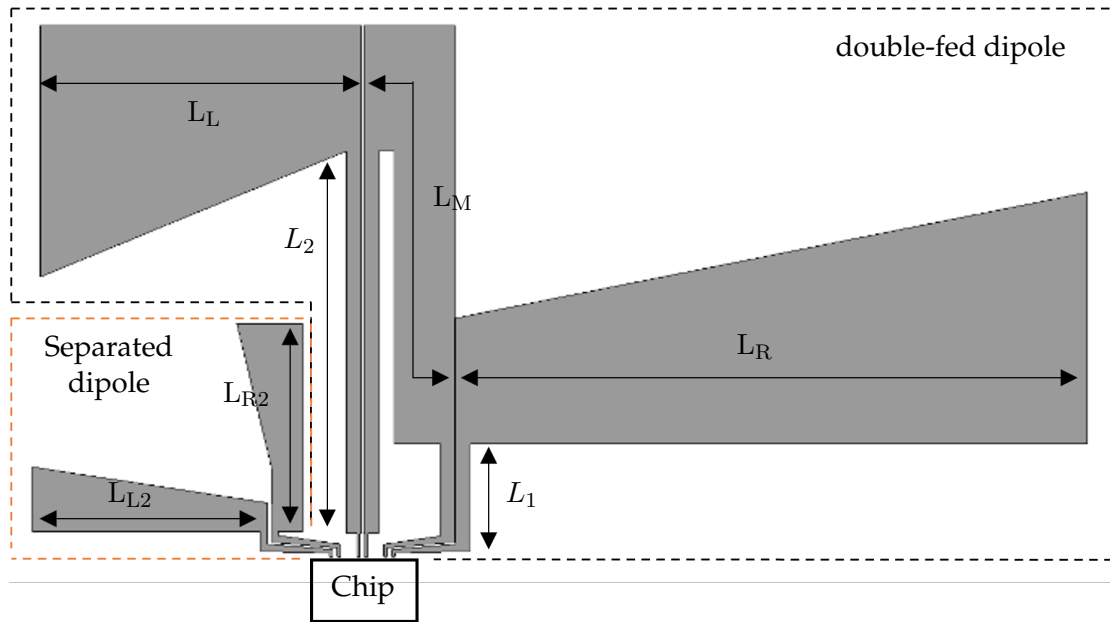
FIGURE 4.5: The layout of the complete dipole-based antenna structure[153].

The respective measured dielectric constant is indicated by $\epsilon_{\text{r,butter}}$. Note that L_M can be chosen freely (within limits) to obtain a compact antenna. The different antenna trace widths are adjusted so that the feed-point impedances (for all materials) take a value of $100\,\Omega$ as well. Consequently, assuming a $100\,\Omega$ differential source/load (that is, the interface of the RF chip), impedance matching is achieved.

Starting with these theoretically calculated dimensions and the topology shown in Fig. 4.5, an optimization by field simulation is executed. This is necessary, because the theoretical approach does not consider any coupling effects and measures to increase the bandwidth (tapered antenna arms). Table 4.3 lists the theoretical values of all dimensions together with the final values after optimization.

Fig. 4.5 shows the layout of the proposed antenna. The double-fed dipole and the separated dipole are marked. The layout shows somehow bent and intertwined features in order to make the overall area small. The dimensions of the circumferential rectangle of the overall antenna are $28 \times 15\,\text{mm}^2$. Well-defined balanced feed lines pass from the dipole feed-ports to the chip. The chip shall provide the switching functionality. The feed-ports are on a straight line, distanced by $0.7\,\text{mm}$.

TABLE 4.3: Dimensions of the dipole-based antenna structure after Fig. 4.5.

Dimensions [mm]	Calculated	After optimization
L_1	1.19	0.75
L_2	11.10	10.35
L_L	8.67	7.85
L_R	13.63	15.12
L_{air}	54.54	52.78
L_{butter}	34.67	33.58
L_M	chosen to be 10	9.11
L_{L2}	-	6.02
L_{R2}	-	5.95

A prototype of the antenna is manufactured for standalone (without RF-chip) measurement. Therefore, three different versions of the antenna board (for different environment: air, butter, minced meat) are produced. They are identical except for the corresponding $100\,\Omega$ differential feed line. The other feed lines are short-circuited at the locations, where the switches would be in the chip. The feed line is extended to the edge of the foil. There, the line traces become wider and the gap between the traces larger (see Fig. 4.6). This wide line on the antenna foil substrate is easily connected to a similarly wide line on thin printed circuit board (PCB) by overlap and simple mechanical pressure. Pressure is applied by two pieces of electromagnetic transparency material (Rohacell foam) that are clamped together with two plastic screws. On the side of the PCB, the wide differential line is continued for half a wavelength, until each trace ends in a $50\,\Omega$ microstrip line. Then, a balanced-to-unbalanced (BalUn) transition is designed, ending in a coax SMA connector for single-port measurement. The simulated - 15 dB matching bandwidth of the BalUn covers the range from $4.5\,\text{GHz}$ to $6.5\,\text{GHz}$. Fig. 4.7 shows the antenna attached to dielectric blocks of butter and meat, respectively, and connected for impedance measurements.

Fig. 4.8 shows the measured reflection coefficient magnitudes, together with simulated results. The antenna is well-matched in all three scenarios. For the cases with attached dielectric blocks, a separate measurement shows that feed match disappears when this particularly fed structure is exposed to free-space (butter and meat removed, curves named "butter-air" and "meat-air", respectively).
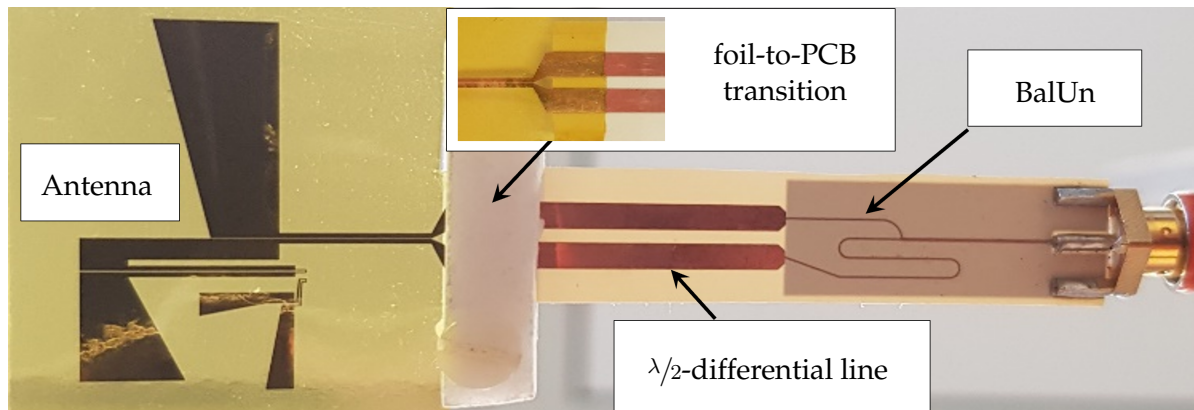
FIGURE 4.6: The measurement setup for measuring the reflection coefficient of the antenna for one given environment (here: air). At the appropriated feed point, the feed line is extended to the edge of the foil. From there it becomes larger to ensure a good handle ability for the pressure-based foil-to-PCB transition. A half-wavelength long differential line accounts for any perturbation. On PCB, a balanced-to-unbalanced (BalUn) transition allows measuring the differential structure with a single-port measurement [153].

4.2.2.3   Prototype with RF-Chip

A prototype of the 3-port antenna connected to an RF-chip[2] is manufactured. A photograph of the RF-chip is given in Fig. 4.9 (a). In Fig. 4.9 (b) the schematic of the RF-chip and the antenna is depicted. The chip comprises a power amplifier and three RF-switches, which are connected to the antenna. Since the respective output port (that is active) and the input port of the antenna are designed to have $100\,\Omega$ differential impedance, power matching between the antenna and the RF-chip is obtained.

A DC bias PCB is developed to conveniently bias and apply the switching functionality to the RF-chip in the foil. To connect the DC PCB with the foil, FFC cables with clamp connectors are used. The RF input line on the foil of the chip is separated and connected to an RF-PCB which includes a foil-to-PCB transition and a BalUn. This is the same as described in subsection 4.2.2.2 (cf. Fig. 4.6). All of these components are then mounted to a holder for radiation pattern measurement. To test the antenna on different materials a material container out of electromagnetic transparent foam (rohacell) is used. A photo is depicted in Fig. 4.10. The inset picture shows the setup and if the material container is filled with minced meat.

---

[2]Designed by Mr. Sefa Özbek, Institute of Electrical and Optical Communications Engineering (INT), University of Stuttgart.
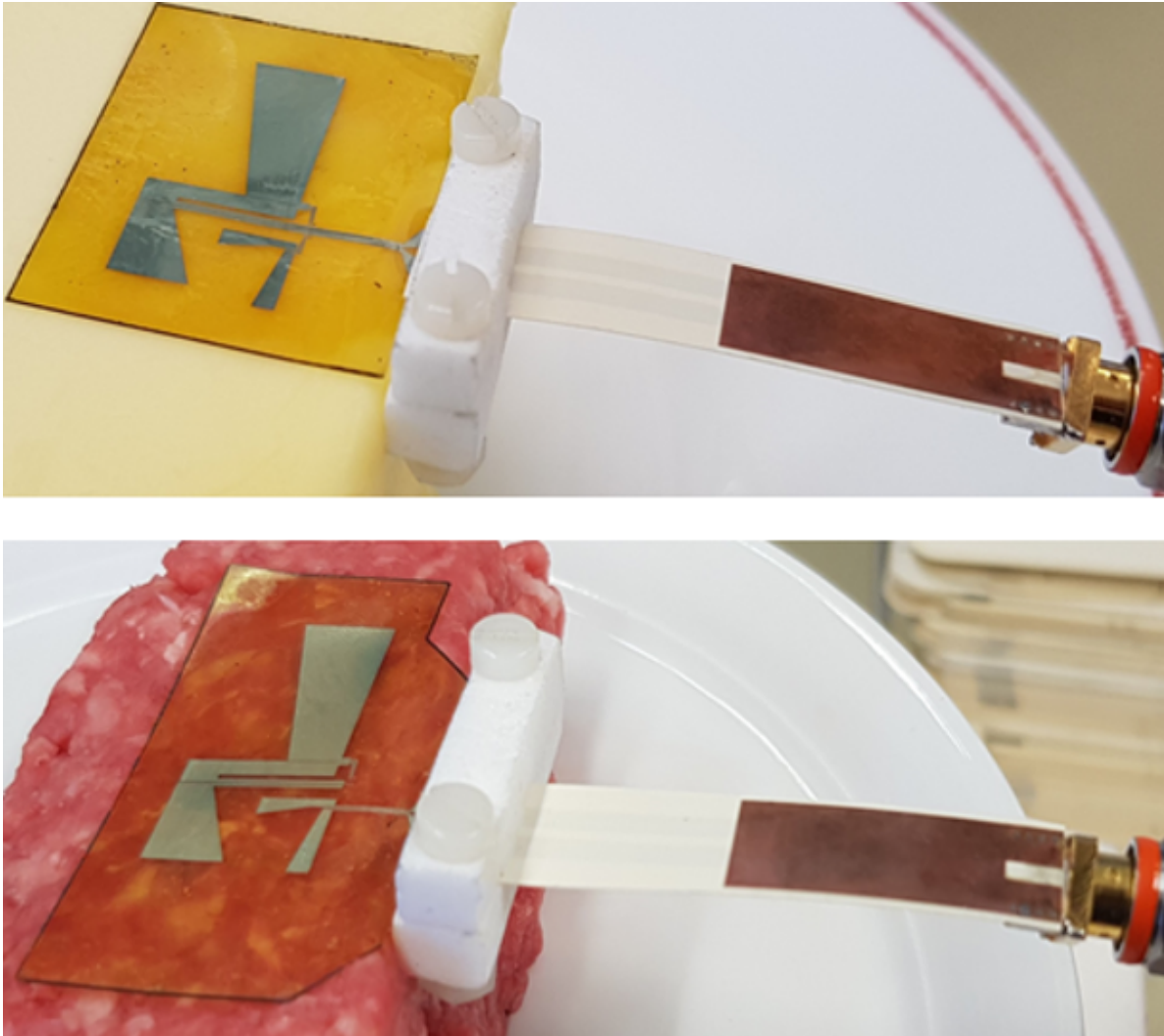
FIGURE 4.7: Photos of the two measurement setups with block of butter (upper photo) and block of minced meat (lower photo) attached to the antenna [153].

The whole system is placed in an anechoic chamber to measure the radiation pattern for the cases of butter and minced meat. The right photograph of Fig. 4.11 shows how the system is mounted in the anechoic chamber. In addition to the DC PCB a second DC board, a so-called RF switch board is developed. On this board, manual switches are implemented for the adjustment of the right output port of the RF chip, which is the input port of the antenna. The DC voltage sources are placed beneath absorbers on the rotating stand so that they can rotate during the measurement. On the left photograph of Fig. 4.11, the foil system attached to the two different materials and the coordinate system to which all the measurement results refer, are shown. It should be
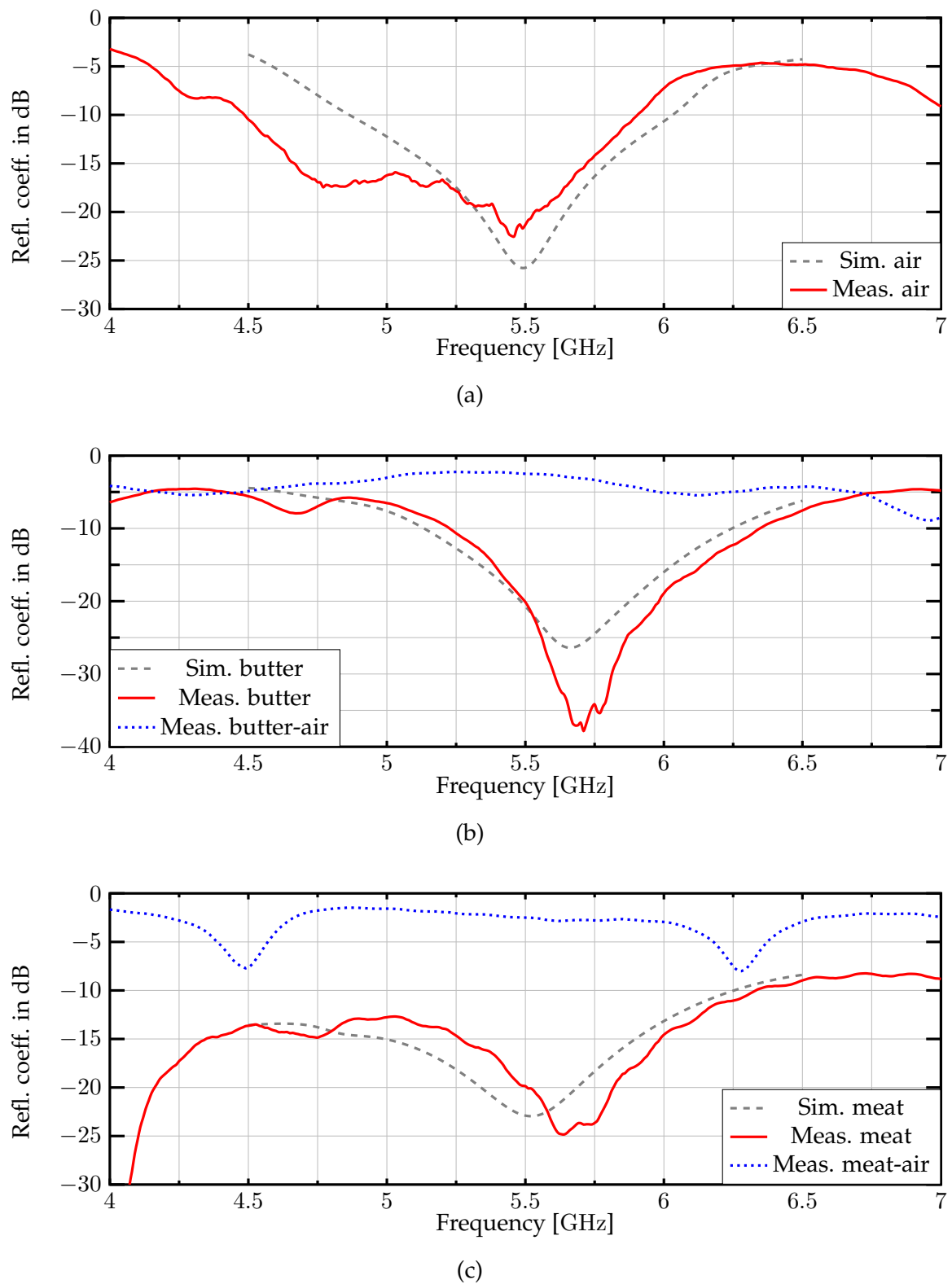
FIGURE 4.8: The simulated and measured reflection coefficient over frequency [153]. (a) all in air. (b) on a block of butter ($\epsilon_r = 3.95$) (c) on a block of minced meat ($\epsilon_r = 42$. For (b) and (c), the blue dotted curve indicates measurement in air, i.e., dielectric block removed.

(a)   (b)
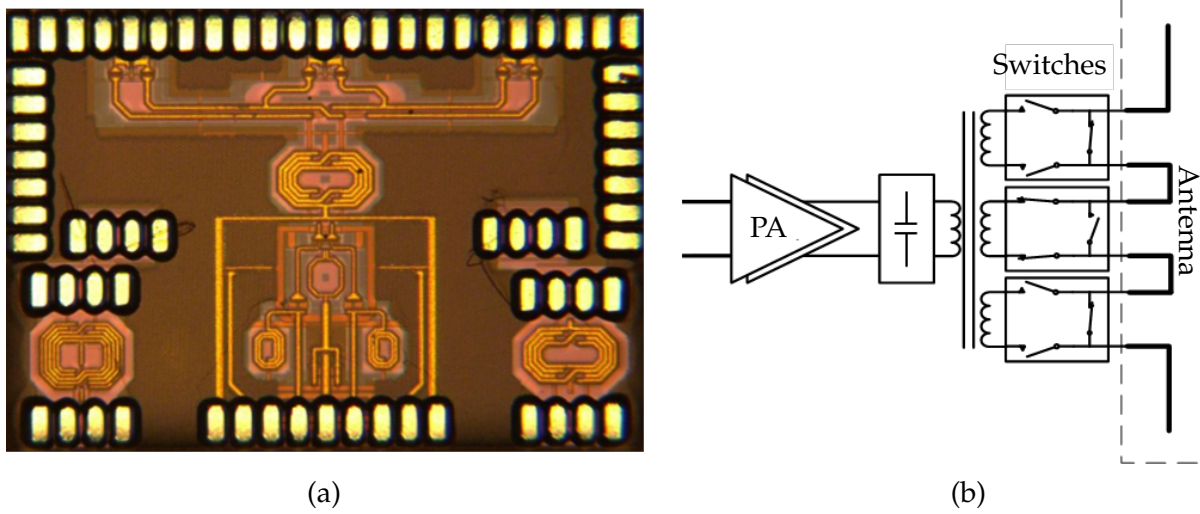
FIGURE 4.9: (a) Photograph of the RF-chip and (b) the schematic of the RF-chip with the antenna [219].
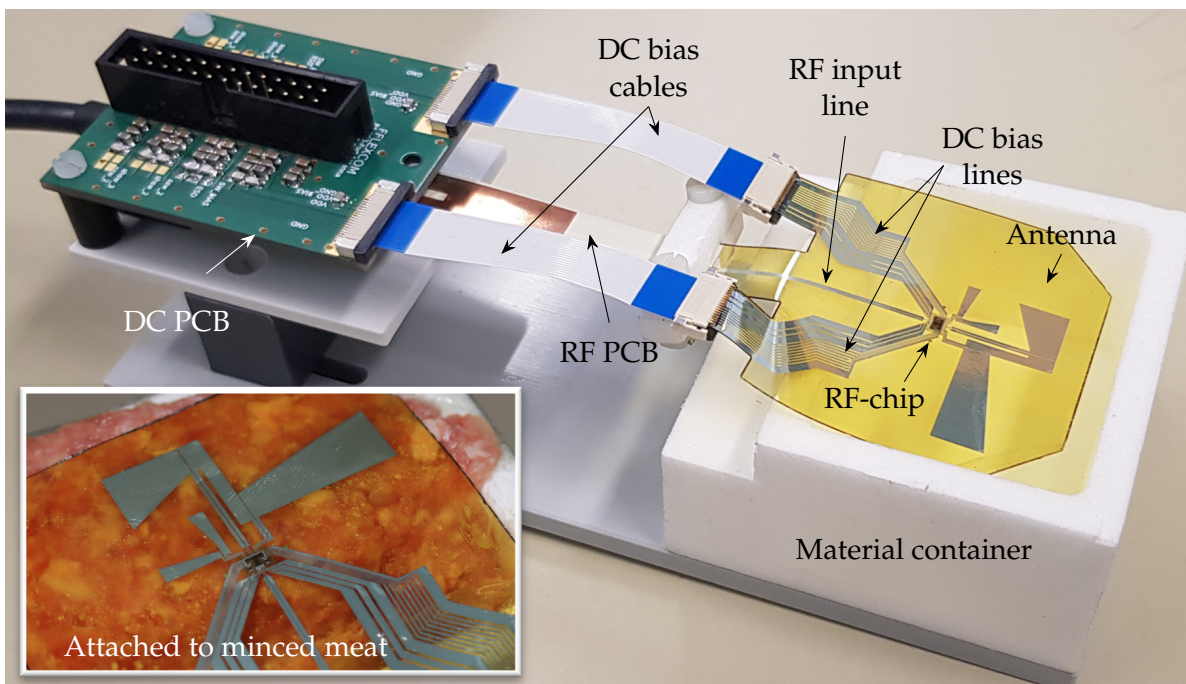
FIGURE 4.10: Photograph of the antenna connected to the RF-chip and embedded into polymer foil. The whole system is mounted on a holder for radiation pattern measurement. The inset picture shows the foil system attached to the minced meat-filled material container.

noted that this radiation pattern measurement serves as a verification of the system communication functionality only. Since the main focus in this antenna design is to reduce the reflection coefficient at different ports for either scenario it is not of interest how the radiation occurs. Beside this, the DC lines and cables as well as the DC PCB will alter the pattern. In Fig. 4.12 some cut planes of the measured (red curve) and simulated (dashed gray curve) radiation pattern are shown. Note, the simulation results shown here are without any surrounding lines or cables or PCB. The light gray areas in sub figures (a)-(d) indicates the angle range, where all the radiated power is dissipated in the absorbers of the rotating arm of the anechoic chamber. Obviously, the measurement results show a similar course when compared with simulations, but ripples are clearly visible in the measurements. This stems from the conductive interference elements (e.g. DC lines and cables) in the vicinity of the antenna.

4.2.3 Discussion

The idea to make a differential, dipole-like structure adaptive to different scenarios (antenna is placed on different half-space filled materials) by choosing different feed positions is pursued. In a practical design, mainly, two challenges must be overcome. Firstly, the unwanted radiation of the feed line and, secondly, the small area, in which, due to the small RF-chip size, the feed positions should be co-located.

An approach for a triple-fed antenna was presented that meets the mentioned challenges. Furthermore, a prototype was made, which in turn shows that the approach leads to the desired goal, which is adaptivity to different scenarios. The antenna shows well-matched feed impedance for 3 different environmental scenarios, that is, when placed in free-space, when attached to a block of permittivity of about 4 and when attached to a block of permittivity of about 42. In all three scenarios, the measured feed match is better than -20 dB at $5.5\,\mathrm{GHz}$. It was also shown that the antenna is functional with a specially made RF-chip incorporated in a thin polymer foil. Thereby, the RF-chip provides the switching capability. Thus, this lays the foundation for a highly flexible wireless transmission system.

The proposed concept can be adapted to other sets of electromagnetic environments.
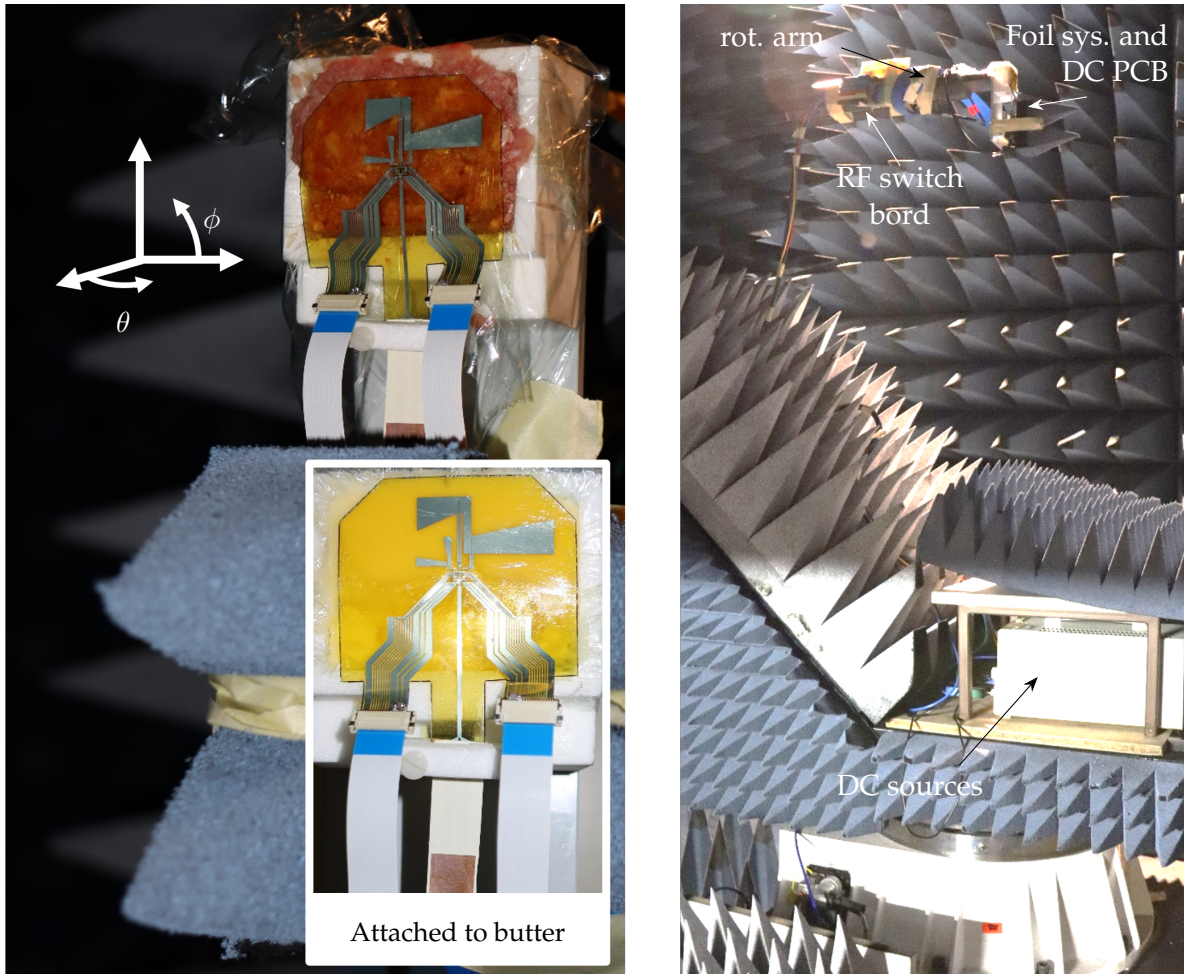
FIGURE 4.11: Photos of the system measurement setup and the coordinate system.

However, more than three scenarios, meaning more than three feeds seems too involved and its feasibility is questionable with the given approach.

4.3 Adaptivity by Switched Load Admittances or Circuits[3]

The most common antenna design method in terms of operating frequencies, bandwidth, polarization, and radiating characteristics is to manipulate the radiating structures' geometry. In many cases impedance-matching networks are used to reduce the

---

[3]Some of the text and pictures presented in this section are extracted (or are modified versions) from [220]. The author is the main contributor to publication [220].

(a) Butter $\phi = 0°$

(b) Meat $\phi = 0°$

(c) Butter $\phi = 90°$

(d) Meat $\phi = 90°$

(e) Butter $\theta = 90°$

(f) Meat $\theta = 90°$
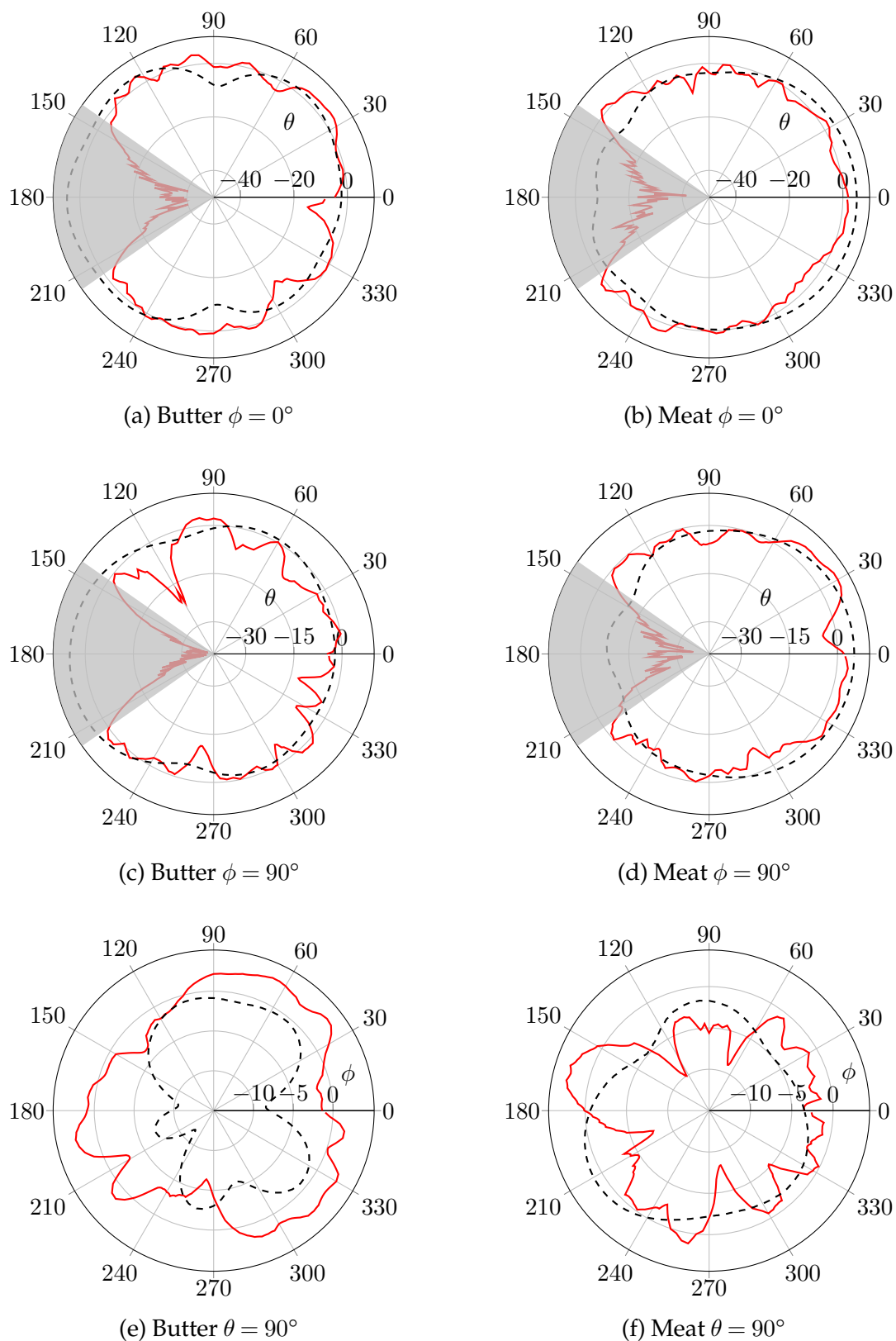
FIGURE 4.12: Polar plots of the specific cut planes (see captions of the sub figures) of the measured (red line) and simulated (gray dashed line) radiation pattern. The light-gray areas in sub figures (a)-(d) indicates the angle range, where all the radiated power is dissipated in the absorbers of the rotating arm of the anechoic chamber.
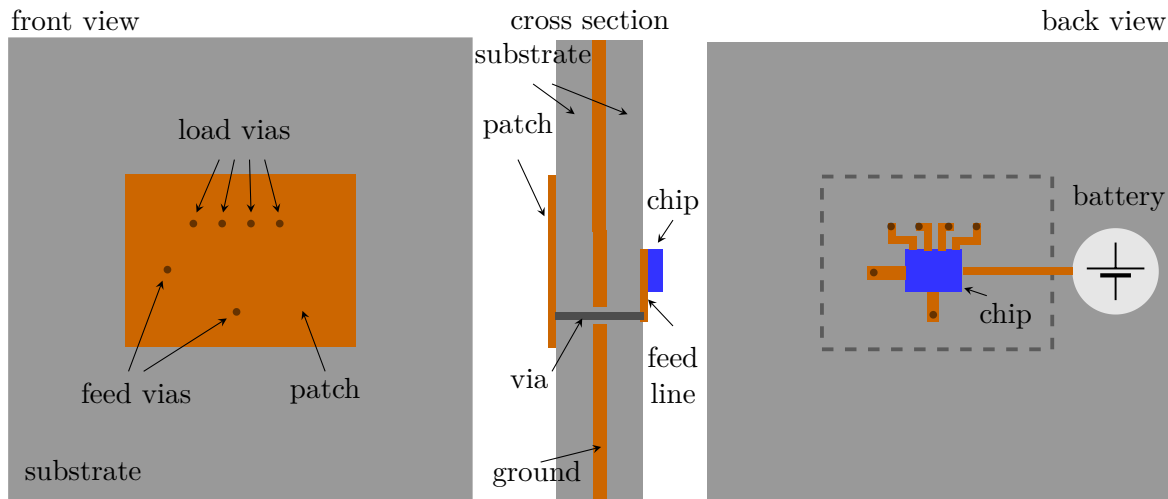
FIGURE 4.13: An RFID tag as a possible application of the presented theory. It comprises a double-fed patch antenna that is loaded with four switchable impedances for reconfiguration. The chip provides both feeding and switching functions [220].

reflection at the input of the antenna. In this section, a theory is developed that allows antenna properties to be altered by external load admittances. Further, these admittances can be switched to obtain reconfiguration. The goal is to achieve impedance matching to the source(s) at one particular frequency or in case of an adaptive (adaptive to the environment) antenna at one particular scenario. Whether the change in frequency is caused by the environment or is self-initiated is irrelevant to the basic theory presented here. For this reason, the frequency reconfiguration is considered below and not the compensation for the frequency change. In Fig. 4.13, a possible application of the following theory is depicted: an RFID tag, comprising a patch antenna with two feed and four load points as well as a chip and a battery. The tag has two substrates separated by a ground plane. The patch is placed on one side, the chip on the other. The chip has two small feed lines and four small load lines that are connected with a via to the patch. As the environment changes, or the operating frequency is required to change, the load impedances are switched such that the desired goal, i.e., impedance matching, is achieved.
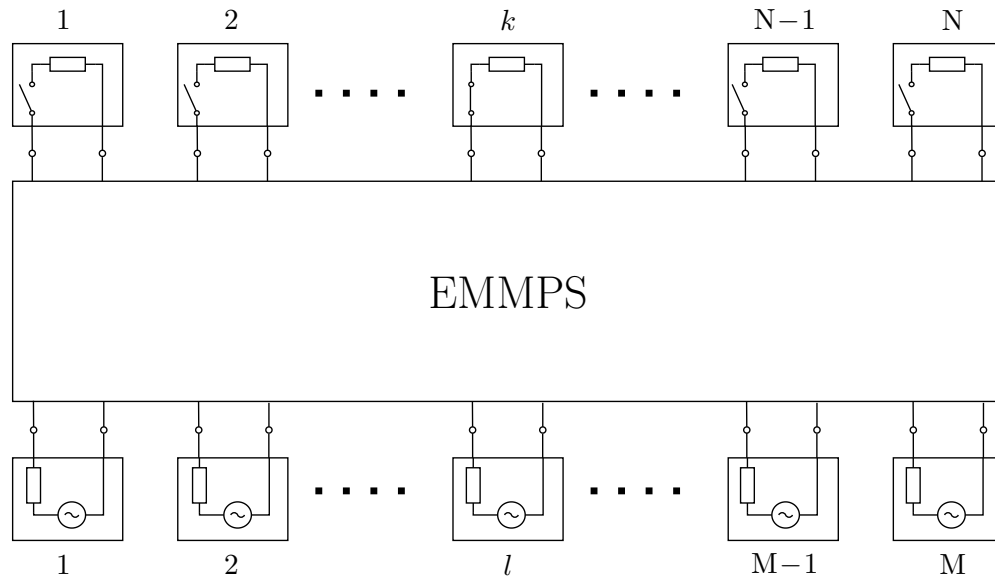
FIGURE 4.14: The principal structure of the considered antenna circuit comprising an electromagnetic multi-port system (EMMPS), N load ports with load admittance and switches, and M source ports with source admittances [220].

4.3.1 Theory

The basic structure of the reconfigurable antenna circuit is separated, as shown in Fig. 4.14, in an electromagnetic multi-port system (EMMPS) and a circuit part comprising sources and switched loads. The EMMPS is assumed to be known (in this work it is calculated by an electromagnetic field solver) and is represented by multi-port parameters such as admittance or scattering parameters. The $N + M$ ports are grouped into M sources and N loads (Fig. 4.14). The behavior of the entire structure depends on the states of the switches. Referring to the RFID tag example of Fig. 4.13, the EMMPS comprises patch antenna, vias, and lines, while the chip contains the loads and sources. In this case the EMMPS has six ports: two source ports and four load ports.

The main goal of the proposed concept is to obtain complex conjugate impedance matching at all source ports at one particular frequency, for one set of settings of the switches. Then, for a different frequency or a different electromagnetic environment, the EMMPS changes, and matching at all source ports should be achieved with a different setting of the switches, but with load and source admittances remaining

unchanged. Therefore, for a given EMMPS, the load admittances are the unknown parameters to be determined. In the derivation of the theory, at first, all switches are closed such that all load admittances are contributing to the behavior at the source ports. Later on, the theory is expanded to deal with different settings of the switches. The EMMPS is supposedly known and represented by:

$$
\mathbf{Y} = \begin{bmatrix} \mathbf{Y}_{\mathrm{ll}} & \mathbf{Y}_{\mathrm{ls}} \\ \mathbf{Y}_{\mathrm{sl}} & \mathbf{Y}_{\mathrm{ss}} \end{bmatrix},
\tag{4.7}
$$

where $\mathbf{Y}$ is a complex matrix with size of $(\mathrm{M} + \mathrm{N}) \times (\mathrm{M} + \mathrm{N})$. This matrix is divided into four sub-matrices: $\mathbf{Y}_{\mathrm{ll}} \in \mathbb{C}^{\mathrm{N} \times \mathrm{N}}$, $\mathbf{Y}_{\mathrm{ls}} \in \mathbb{C}^{\mathrm{N} \times \mathrm{M}}$, $\mathbf{Y}_{\mathrm{sl}} \in \mathbb{C}^{\mathrm{M} \times \mathrm{N}}$ and $\mathbf{Y}_{\mathrm{ss}} \in \mathbb{C}^{\mathrm{M} \times \mathrm{M}}$. The index "l" stands for load and "s" for source. Therefore, $\mathbf{Y}_{\mathrm{ll}}$ describes the relationship between the individual load ports through the EMMPS. The sub-matrix $\mathbf{Y}_{\mathrm{ls}}$ describes the relationship between the source and load ports as well as the sub-matrix $\mathbf{Y}_{\mathrm{sl}}$, just vice versa. "$\mathbf{Y}_{\mathrm{ss}}$" gives the relationship between all source ports. Further, a load admittance matrix is defined as:

$$
\mathbf{Y_L} = \mathrm{diag}(Y_{L_1}, Y_{L_2}, \ldots, Y_{L_k}, \ldots, Y_{L_N}),
\tag{4.8}
$$

where Y_{L_k} is the load admittance at the k-th load port. At the source port, a source port matrix is defined that represents the known source admittances:

$$
\mathbf{Y_S} = \mathrm{diag}\left(Y_{\mathrm{S}_1}, Y_{\mathrm{S}_2}, \ldots, Y_{\mathrm{S}_l}, \ldots, Y_{\mathrm{S}_M}\right).
\tag{4.9}
$$

Y_{S_l} is the source admittance at the l-th source port. The following conversions are performed in order to find a form, which separates the known and the unknown, i.e., load admittances. According to the definition of the admittance parameters, the currents in all load ports are calculated as:

$$
\vec{\mathrm{I_l}} = \mathbf{Y_{ll}} \vec{\mathrm{V}}_l + \mathbf{Y_{ls}} \vec{\mathrm{V}}_s
\tag{4.10}
$$

and the currents into all source ports to:

$$\vec{I_s} = \mathbf{Y_{sl}}\vec{V_l} + \mathbf{Y_{ss}}\vec{V_s}. \tag{4.11}$$

$\vec{I_l}$ and $\vec{V_l}$ are vectors whose k-th entry gives the current and voltage of the k-th load port. $\vec{I_s}$ and $\vec{V_s}$ are vectors whose entries are the currents and voltages of the source ports. The load port currents and voltages are related by the load admittances as follow:

$$\vec{I_l} = -\mathbf{Y_L}\vec{V_l}. \tag{4.12}$$

The minus sign originates from the definition of port currents, which always pointing towards the ports. Inserting (4.12) into (4.10) and solving for $\vec{V_l}$ leads to:

$$\vec{V_l} = -\left(\mathbf{Y_{ll}} + \mathbf{Y_L}\right)^{-1}\mathbf{Y_{ls}}\vec{V_s}. \tag{4.13}$$

$\left(\mathbf{Y_{ll}} + \mathbf{Y_L}\right)^{-1}$ denotes the inverse matrix of matrix $\left(\mathbf{Y_{ll}} + \mathbf{Y_L}\right)$. When inserting (4.13) into (4.11), the following equation for the current at the source ports are obtained:

$$\vec{I_s} = \left(\mathbf{Y_{ss}} - \mathbf{Y_{sl}}\left(\mathbf{Y_{ll}} + \mathbf{Y_L}\right)^{-1}\mathbf{Y_{ls}}\right)\vec{V_s}. \tag{4.14}$$

Considering the source port, for example, for the l-th source port in Fig. 4.15, the following relation holds:

$$\vec{I_s} = \mathbf{Y_S}\vec{V_0} - \mathbf{Y_S}\vec{V_s}. \tag{4.15}$$

Here, the $\vec{V_0}$ vector includes all source voltages at the respective source ports. Furthermore, a voltage divider between the source and the source-port voltage is applied and expressed with matrices at all source ports:

$$\vec{V_s} = \left(\mathbf{Y_S} + \mathbf{Y_{in}}\right)^{-1}\mathbf{Y_S}\vec{V_0} = \mathbf{M_{vr}}\vec{V_0}. \tag{4.16}$$

Here,

$$\mathbf{Y_{in}} = \mathrm{diag}\left(Y_{in_1}, Y_{in_2}, \ldots, Y_{in_l}, \ldots, Y_{in_M}\right) \tag{4.17}$$
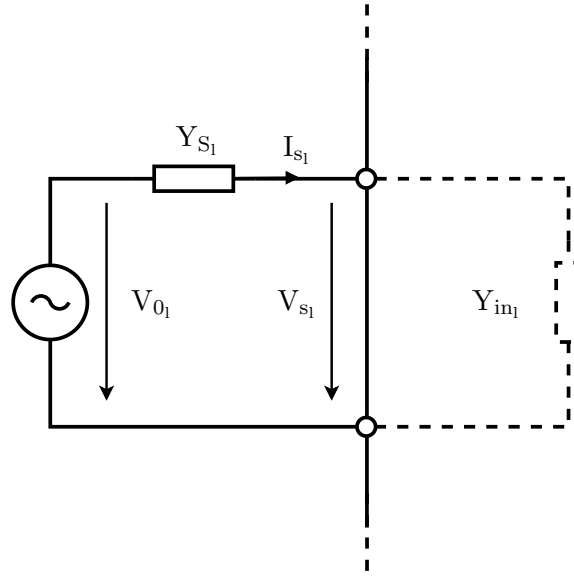
FIGURE 4.15: Current, voltage and admittance labeling at the l-th source port.

is a diagonal matrix with the input admittances (active admittances) at the respective source port, and $\mathbf{M_{vr}}$ is a diagonal matrix, named voltage ratio matrix. Mutual substitution of equations (4.14)-(4.16) results in

$$\mathbf{Y_s}\left(\mathbf{I_M} - \mathbf{M_{vr}}\right)\vec{V}_0 = \left(\mathbf{Y_{ss}} - \mathbf{Y_{sl}}\left(\mathbf{Y_{ll}} + \mathbf{Y_L}\right)^{-1}\mathbf{Y_{ls}}\right)\mathbf{M_{vr}}\vec{V}_0, \qquad (4.18)$$

with the identity matrix $\mathbf{I_M}$ of size M. The matching condition at the source ports is:

$$\mathbf{Y_{in}} = \overline{\mathbf{Y_S}} = \mathrm{diag}\left(Y^*_{S_1}, Y^*_{S_2}, \ldots, Y^*_{S_l}, \ldots, Y^*_{S_M}\right). \qquad (4.19)$$

Here, $\overline{\mathbf{Y_S}}$ denotes the complex conjugate matrix of $\mathbf{Y_S}$ and $Y^*_{S_l}$ the complex conjugate of Y_{S_l}. In (4.18), $\mathbf{M_{vr}}$ is the only one matrix, dependent on $\mathbf{Y_{in}}$, therefore

$$\mathbf{M_{vr}} = \left(\mathbf{Y_S} + \overline{\mathbf{Y_S}}\right)^{-1}\mathbf{Y_S} = \frac{1}{2}\,\mathrm{Re}\{\mathbf{Y_S}\}^{-1}\mathbf{Y_S} = \frac{1}{2}\left(\mathbf{I_M} + \mathrm{j}\,\mathrm{Re}\{\mathbf{Y_S}\}^{-1}\,\mathrm{Im}\{\mathbf{Y_S}\}\right) \qquad (4.20)$$

and $\mathbf{I_M} - \mathbf{M_{vr}} = {}^1\!/{}_2\left(\mathbf{I_M} - \mathrm{j}\,\mathrm{Re}\{\mathbf{Y_S}\}^{-1}\,\mathrm{Im}\{\mathbf{Y_S}\}\right)$ with j as the imaginary unit. If the source admittances only have a real part, the voltage ratio matrix becomes the identity matrix multiplied by $1/2$. With the relation $\mathbf{A}^{-1} = {}^{\mathrm{adj}\,(\mathbf{A})}\!/{}_{\det\,(\mathbf{A})}$ for an invertible square matrix $\mathbf{A}$, the expression of (4.18) changes to:

$$\det\left(\mathbf{Y_{ll}} + \mathbf{Y_L}\right)\mathbf{Y_s}\left(\mathbf{I_M} - \mathbf{M_{vr}}\right)\vec{V}_0 =$$
$$\left(\det\left(\mathbf{Y_{ll}} + \mathbf{Y_L}\right)\mathbf{Y_{ss}} - \mathbf{Y_{sl}}\,\mathrm{adj}\left(\mathbf{Y_{ll}} + \mathbf{Y_L}\right)\mathbf{Y_{ls}}\right)\mathbf{M_{vr}}\vec{V}_0. \tag{4.21}$$

Here, $\mathrm{adj}\left(\mathbf{A}\right)$ indicates the adjugate matrix of $\mathbf{A}$. Still, the goal is to separate the knowns from the unknowns. Therefore, the following relations (from section 5 of [221]) are applied

$$\det\left(\mathbf{Y_{ll}} + \mathbf{Y_L}\right) = \sum_{j=0}^{2^{\mathrm{N}}-1} \det\left(\mathbf{P}_{\mathbf{S(j)}}^{\mathbf{T}}\mathbf{Y_{ll}}\mathbf{P}_{\mathbf{S(j)}}\right) \prod_{i \in \mathrm{S}(j)} Y_{L_i} \tag{4.22}$$

$$\mathrm{adj}\left(\mathbf{Y_{ll}} + \mathbf{Y_L}\right) = \sum_{j=0}^{2^{\mathrm{N}}-1} \mathbf{P}_{\mathbf{S(j)}}\,\mathrm{adj}\left(\mathbf{P}_{\mathbf{S(j)}}^{\mathbf{T}}\mathbf{Y_{ll}}\mathbf{P}_{\mathbf{S(j)}}\right)\mathbf{P}_{\mathbf{S(j)}}^{\mathbf{T}} \prod_{i \in \mathrm{S}(j)} Y_{L_i} \tag{4.23}$$

Where S is an index set of all possible combinations out of $\{1, \ldots, \mathrm{N}\}$ without repetition and in lexicographical order. For example, if $\mathrm{N} = 3$, then

$$\mathrm{S} := \{\{\}, \{1\}, \{2\}, \{3\}, \{1,2\}, \{1,3\}, \{2,3\}, \{1,2,3\}\}$$

with entry $\mathrm{S}(0) = \varnothing$ (the empty element) and entry $\mathrm{S}(4) = \{1,2\}$. Further, $\mathbf{P}_{\mathbf{S(j)}}$ denotes the identity matrix of size N, in which the columns indexed by the set $\mathrm{S}(j)$ are removed. Inserting this relation into (4.21) results in

$$\sum_{j=1}^{2^{\mathrm{N}}-1} \vec{k}_j \prod_{i \in \mathrm{S}(j)} Y_{L_i} = \vec{r} \tag{4.24}$$

with

$$\vec{k}_j = \left(\left(\mathbf{Y_{ss}} + \mathbf{Y_S}\right)\mathbf{M_{vr}} - \mathbf{Y_S}\right)\det\left(\mathbf{P}_{\mathbf{S(j)}}^{\mathbf{T}}\mathbf{Y_{ll}}\mathbf{P}_{\mathbf{S(j)}}\right)\vec{V}_0 -$$
$$\mathbf{Y_{sl}}\mathbf{P}_{\mathbf{S(j)}}\,\mathrm{adj}\left(\mathbf{P}_{\mathbf{S(j)}}^{\mathbf{T}}\mathbf{Y_{ll}}\mathbf{P}_{\mathbf{S(j)}}\right)\mathbf{P}_{\mathbf{S(j)}}^{\mathbf{T}}\mathbf{Y_{ls}}\mathbf{M_{vr}}\vec{V}_0$$

and

$$\vec{r} = \det\left(\mathbf{Y_{ll}}\right)\left(\mathbf{Y_S} - \left(\mathbf{Y_{ss}} + \mathbf{Y_S}\right)\mathbf{M_{vr}}\right)\vec{V}_0 + \mathbf{Y_{sl}}\,\mathrm{adj}\left(\mathbf{Y_{ll}}\right)\mathbf{Y_{ls}}\mathbf{M_{vr}}\vec{V}_0.$$
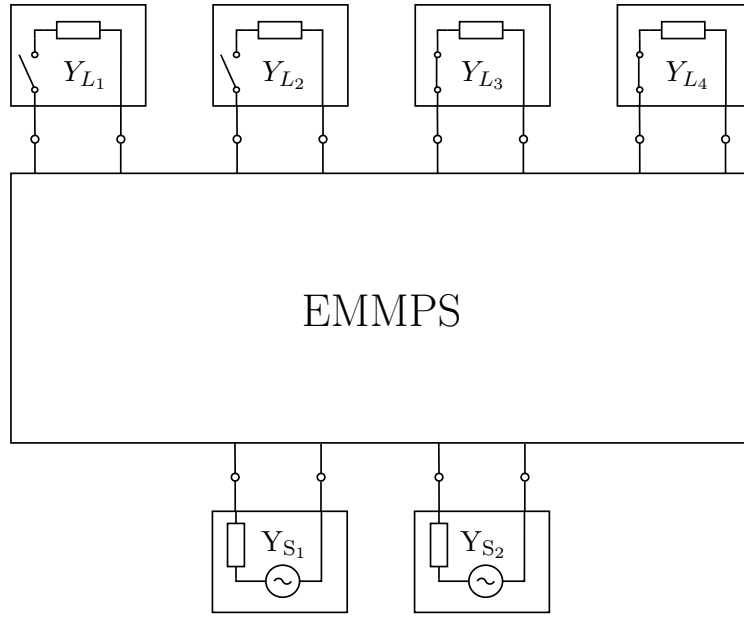
FIGURE 4.16: The principle structure of the considered example with $N = 4$ load admittances and $M = 2$ sources [220].

Equation (4.24) can be expressed in matrix form to:

$$\mathbf{K}\vec{v}_l = \vec{r} \tag{4.25}$$

with matrix

$$\mathbf{K} = \left(\vec{k_1}, \ldots, \vec{k_j}, \ldots \tilde{k}_{(2^N - 1)} \right)$$

and the load vector

$$\vec{v}_l = \left(Y_{L_1}, \ldots, Y_{L_N}, Y_{L_1} Y_{L_2}, \ldots, Y_{L_{N-1}} Y_{L_N}, \ldots, \ldots, Y_{L_1} Y_{L_2} \cdots Y_{L_{N-1}} Y_{L_N} \right)^{\mathrm{T}},$$

where the entries are the lexicographically ordered combinations out of all load admittances without repetitions. Here, $\mathbf{K} \in \mathbb{C}^{M \times 2^N - 1}$, $\vec{v}_l \in \mathbb{C}^{2^N - 1 \times 1}$ and $\vec{r} \in \mathbb{C}^{M \times 1}$. Equation (4.25) is a non-linear equation system. $\vec{v}_l$ is to be found, such that (4.25) is fulfilled, thereby matching all source ports for the considered case.

4.3.1.1 Applying the idea of switching load admittances

Now, as a theory for an EMMPS with loads and sources has been derived the concept of switched load admittances will be presented. For the sake of simplicity, the example above of Fig. 4.13 will be used to illustrate the idea. The principle structure is depicted in Fig. 4.16. Obviously, there are two sources and four load admittances, thus $N = 4$ and $M = 2$. For one particular frequency and if all switches are closed, (4.25) has the following form:

$$
\begin{bmatrix} k_{11} & k_{12} & \cdots & k_{1(15)} \\ k_{21} & k_{22} & \cdots & k_{2(15)} \end{bmatrix}
\begin{pmatrix}
Y_{L_1} \\
Y_{L_2} \\
Y_{L_3} \\
Y_{L_4} \\
Y_{L_1}Y_{L_2} \\
Y_{L_1}Y_{L_3} \\
Y_{L_1}Y_{L_4} \\
Y_{L_2}Y_{L_3} \\
Y_{L_2}Y_{L_4} \\
Y_{L_3}Y_{L_4} \\
Y_{L_1}Y_{L_2}Y_{L_3} \\
Y_{L_1}Y_{L_2}Y_{L_4} \\
Y_{L_1}Y_{L_3}Y_{L_4} \\
Y_{L_2}Y_{L_3}Y_{L_4} \\
Y_{L_1}Y_{L_2}Y_{L_3}Y_{L_4}
\end{pmatrix}
= \begin{pmatrix} r_1 \\ r_2 \end{pmatrix}
\tag{4.26}
$$

This equation system now has four unknowns in two equations, which is underdetermined. To fulfill the two equations, it might be sufficient to use only two unknowns. Therefore, the switches of load admittances Y_{L_3} and Y_{L_4} are put in open state. In an ideal theoretical approach, $Y_{L_3} = Y_{L_4} = 0$. Equation (4.26) simplifies then to

$$
\begin{bmatrix} k_{11} & k_{12} & k_{15} \\ k_{21} & k_{22} & k_{25} \end{bmatrix}
\begin{pmatrix} Y_{L_1} \\ Y_{L_2} \\ Y_{L_1}Y_{L_2} \end{pmatrix}
= \begin{pmatrix} r_1 \\ r_2 \end{pmatrix},
\tag{4.27}
$$

for which a solution can be found. A change of frequency or of the environment of the antenna will alter the EMMPS, i.e., the matrix $\mathbf{K}$ and vector $\vec{r}$, but the source should be staying matched. Therefore, the switches of load admittances Y_{L_3} and Y_{L_4} are closed and Y_{L_1} and Y_{L_2} are opened. Consequently, $Y_{L_1} = Y_{L_2} = 0$ and

$$
\begin{bmatrix} k'_{13} & k'_{14} & k'_{1(10)} \\ k'_{23} & k'_{24} & k'_{2(10)} \end{bmatrix} \begin{pmatrix} Y_{L_3} \\ Y_{L_4} \\ Y_{L_3}Y_{L_4} \end{pmatrix} = \begin{pmatrix} r'_1 \\ r'_2 \end{pmatrix}. \tag{4.28}
$$

The apostrophe of matrix $\mathbf{K}$ and vector $\vec{r}$ indicates the change of the EMMPS. It should be noted that even if the switches are not perfect (e.g. $Y_{L_1} = Y_{L_2} \neq 0$) but known, the equation system can be rearranged to obtain the same form as in (4.27) and (4.28). Another approach could be to switch multiple load admittances at the same port, leading to the same form of equations. Throughout the following examples, possible applications of the presented theory is given.

4.3.2 Examples

4.3.2.1 A doubly- and simultaneously fed square patch

The first example shows how the theory can be used in antenna design. The object of the investigation is exclusively the calculation of the load admittances of a doubly edge-fed square patch antenna without considering the switching option. The structure is depicted in Fig. 4.17. The square patch ($70 \times 70\,\mathrm{mm}^2$) on FR4 substrate is fed with two orthogonal $50\,\Omega$-feed line ending at the edges of the patch. Since the edge impedance of the patch is different ($\approx (50 + \mathrm{j}60)\Omega$) in comparison to the source impedance, which is $50\,\Omega$ at the considered frequency of $1\,\mathrm{GHz}$, there is no inherent impedance matching. It is also clear that if the two sources are matched, their powers are combined within the square patch. To avoid losses in the load admittances, the real parts are set to zero. Then (4.25) can be rewritten in a purely real equation system:

$$
\mathrm{Re}\{\mathbf{K}\}\,\mathrm{Re}\{\vec{v}_l\} - \mathrm{Im}\{\mathbf{K}\}\,\mathrm{Im}\{\vec{v}_l\} = \mathrm{Re}\{\vec{r}\} \tag{4.29a}
$$
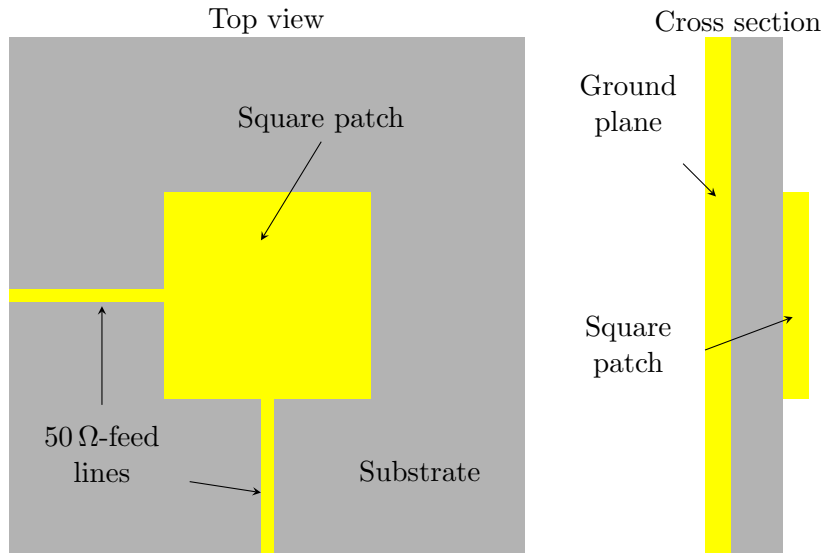
FIGURE 4.17: The structure of a doubly edge-fed square patch [220].

$$\mathrm{Re}\{\mathbf{K}\}\,\mathrm{Im}\{\vec{v_l}\} + \mathrm{Im}\{\mathbf{K}\}\,\mathrm{Re}\{\vec{v_l}\} = \mathrm{Im}\{\vec{r}\}. \tag{4.29b}$$

Naturally, this has doubled the number of equations. In this example, for lossless matching, there are four equations, for which four load admittances, i.e., load susceptances, are required. This leads to a $\mathbf{K}$ matrix of size (2×15) and a $\vec{r}$ vector of size (2×1). The question is how and where these loads should be inserted. In Fig. 4.18 (a) and (b), the load structure is depicted. From the patch (orange colored), a via is connected to a small circular disc on the bottom, which is then connected over a surface-mounted device (SMD), e.g., a capacitor or inductor to the ground plane. Since the positions of the load ports are always a degree of freedom, it is interesting to investigate how the load suceptances behave by varying these locations. Therefore, the loads positions are parameterized in polar coordinates according to Fig. 4.18 (c) to:

$$\mathrm{x}_{i+1} = \mathrm{R}\cos\left(\alpha + \mathrm{i}\frac{\pi}{2}\right) \tag{4.30a}$$

$$\mathrm{y}_{i+1} = \mathrm{R}\sin\left(\alpha + \mathrm{i}\frac{\pi}{2}\right), \tag{4.30b}$$

where $\mathrm{i} = 0, 1, 2, 3$. At the position $(\mathrm{x}_{i+1}, \mathrm{y}_{i+1})$, the susceptance B_{i+1} with $Y_{L_{1+i}} = \mathrm{j}B_{i+1}$ is inserted. The following steps are performed to find all the loads:

(a)   (b)
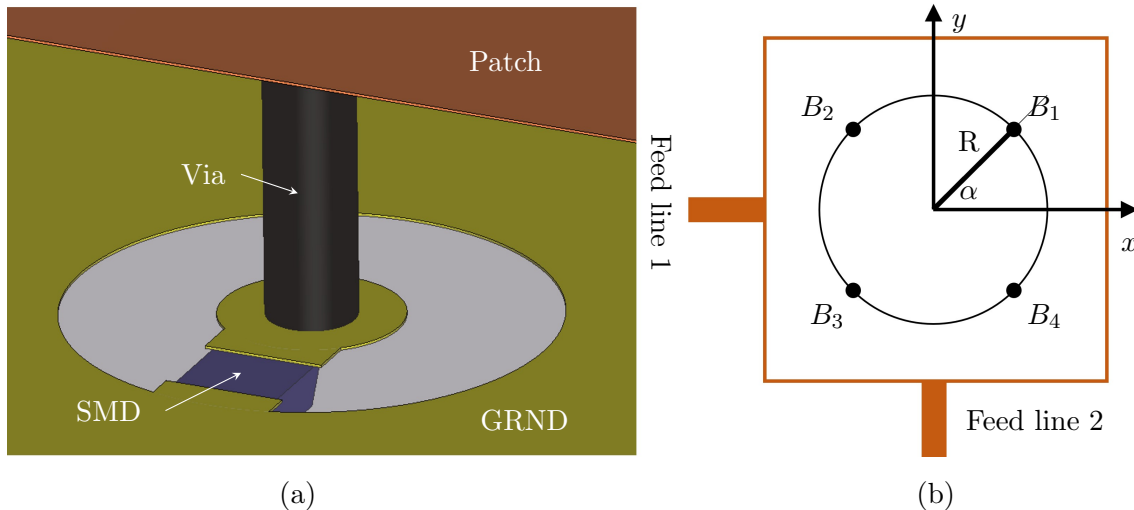
FIGURE 4.18: Insertion of load susceptances in the patch antenna circuit of Fig. 4.17. (a) via with surface-mount (SMD) shunt susceptance on the board backside (dielectric set transparent); (b) symmetrical positions of four shunt susceptances (denoted B_1, B_2, B_3, B_4) at positions, which are defined by parameters R and α [220].

- Computer-aided design (CAD) of the antenna including the feed and load structure.

- S-parameters simulation at $1\,\text{GHz}$ in *CST Microwave Studio* of the design, where all feeds and loads are represented by ports (six in total).

- Export of the six port S-parameters from *CST* and import in *MATLAB*.

- Calculation of the load susceptances:

    1. S to Y parameters conversion.

    2. Calculation of **K** matrix and vector $\vec{r}$ after (4.24).

    3. Setting up non-linear equation system as in (4.25).

    4. Solving it numerically.

These steps are done for varying values of R and α and the susceptances are calculated at $1\,\text{GHz}$. From the susceptances, the component values can be found, for either a capacitor (positive susceptance) or an inductor (negative susceptance). In Fig. 4.19 the calculated load susceptances for various angles (see graphs (a) to (d)) over the radius

R and various radii (see graphs (e) to (f)) over angle α are depicted. The markers indicate the simulation and calculations points. All legends apply to all graphs and can be used interchangeably. It should be noted that an exact solution cannot be found for every position. Some points show an error, but which is in worst case still less than 1×10^{-7} with $\mathrm{error} = \max(|\mathbf{K}\vec{v_l} - \vec{r}|))$. It is by no means clear that a solution can be found for every arbitrary EMMPS. On the other hand, there can also be multiple solutions. Considering graphs (a) to (d) of Fig. 4.19, all the values of these graphs reflects the mirror symmetry of the diagonal from the lower left to the upper right corner of the structure, as shown in Fig. 4.18 (c). In (a), where $\alpha = 0°$, the values of B_1 are equal to the ones of B_2. Also the values of B_3 are equal to the values of B_4. Sub figure (d) can be obtained from (b) by interchanging B_2 and B_4. Susceptances B_1 and B_3 remain untouched. This comes from the fact that if the structure of $\alpha = 22.5°$ is mirrored along the diagonal from the lower left to the upper right corner, the structure of $\alpha = 67.5°$ is replicated. For $\alpha = 45°$, which is (c), B_1 and B_3 are located on the diagonal. The behaviour of these two values over R deviates but shows a similar course. In Fig. 4.19 (e) the susceptances over the angle α for the radius R $= 5\,\mathrm{mm}$ and in (f) for R $= 30\,\mathrm{mm}$ are depicted.

In addition, the frequency behaviour of the load susceptances with $\alpha = 45°$ are shown in Fig. 4.20 for different radii of R. As expected, B_2 and B_4 show same values over frequency ((b) equals (d)). Also, the behaviour of B_1 and B_3 is similar (cf. Fig. 4.19 (c)). The curves of all susceptances for R $= 5\,\mathrm{mm}$ and $17\,\mathrm{mm}$ show points of discontinuities.

The input impedance Z_{in_1} at source port one and Z_{in_2} at source port two, when the EMMPS is loaded with the calculated respective susceptances, is depicted in Fig. 4.22. The behaviour of the resistance (a) and the reactance (b) of the input impedances over the frequency for three different values of the radius R ($5\,\mathrm{mm}$, $17\,\mathrm{mm}$ and $30\,\mathrm{mm}$) and for $\alpha = 45°$ is shown. Here, the sources are simultaneously exciting the EMMPS. Here again, the structural symmetry is reflected in the values of Z_{in_1} and Z_{in_2}, which are the same. The plots of Fig. 4.22, each show two orthogonal dashed lines. Where these lines cross, the EMMPS with the respective loads fulfils (4.25). At these locations, the variation of the impedances over frequency deviates, even if the variation of the load
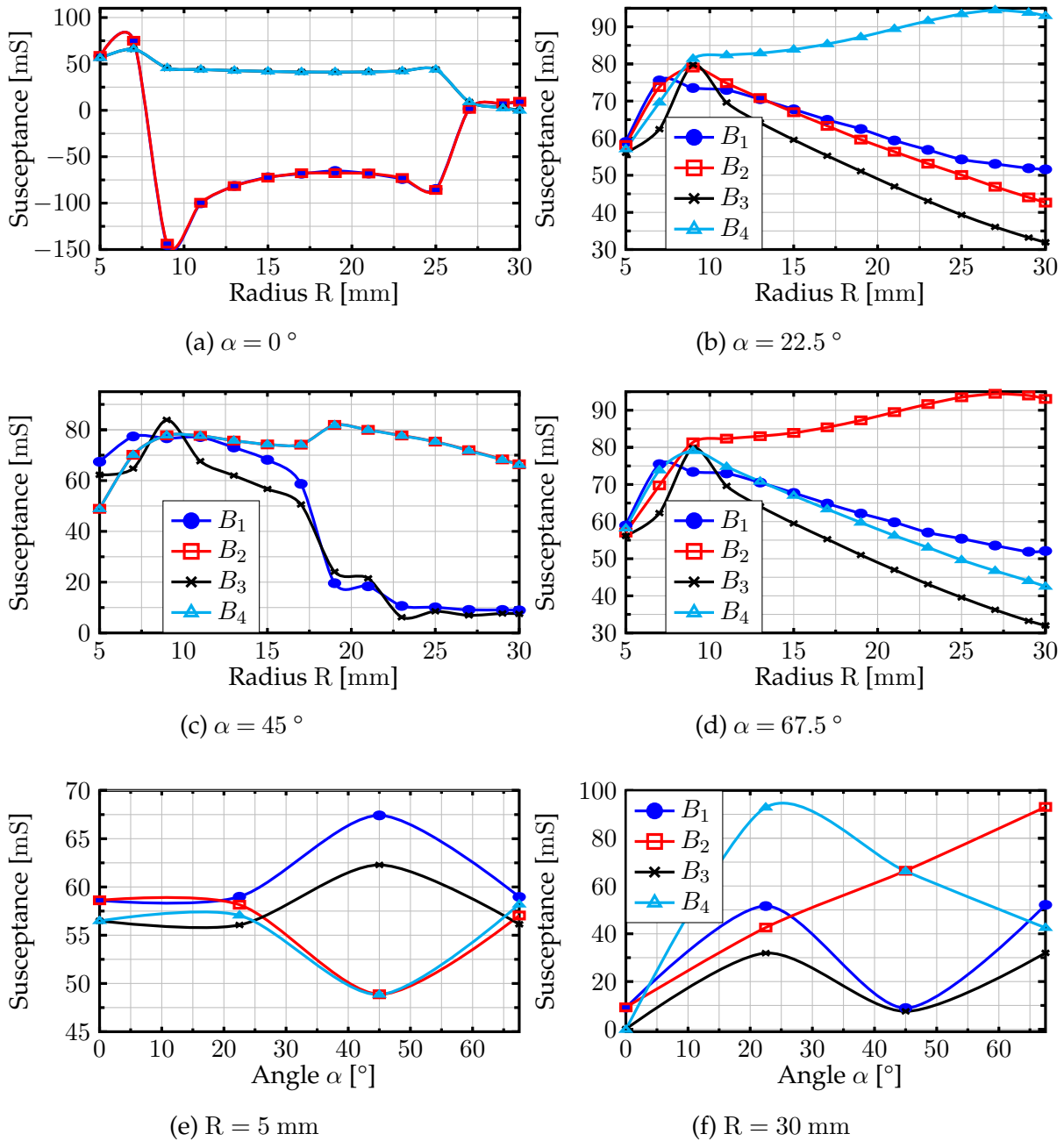
FIGURE 4.19: The calculated load susceptances at 1 GHz for various angle (a)-(d) over the radius R and various radii (e)-(f) over angle α [220].
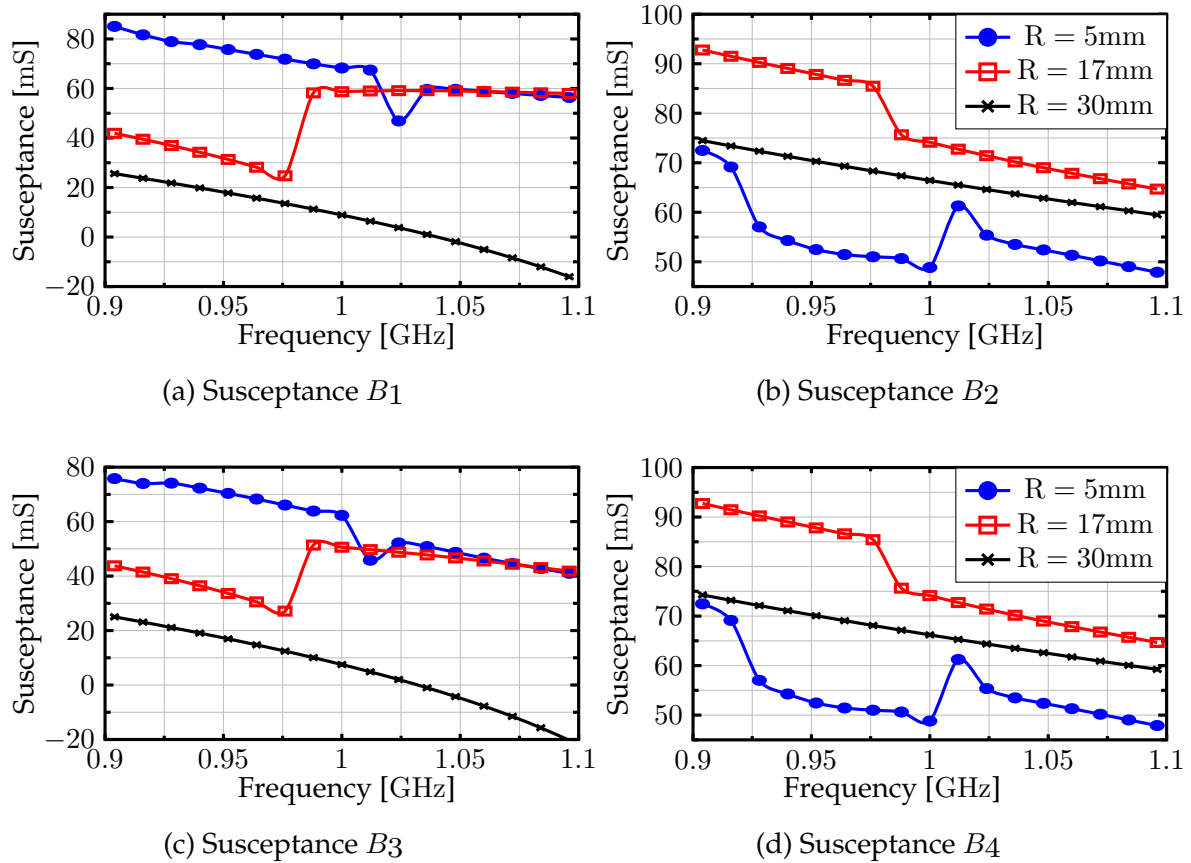
FIGURE 4.20: The four susceptances over the frequency for three different values of R with $\alpha = 45°$. The legends of all graphs are same as in (b) and (d)[220].

susceptances over frequency show similar slopes (cf. Fig. 4.20).

It is also worth evaluating the solutions in terms of the field parameters, such as the surface current. Therefore, the calculated susceptances (here: capacitors) are included in the field simulation. In Fig. 4.21 the surface current at $1\,\mathrm{GHz}$ on the square patch for (a) $\mathrm{R} = 5\,\mathrm{mm}$, (b) $17\,\mathrm{mm}$ and (c) $30\,\mathrm{mm}$ at a value of α of $45°$ is depicted. Clearly, there is an increased current density around the load locations, resulting in a current distribution much different from that in the case without loads.

4.3.2.2 Loaded Patch Study

In this example a single edge-fed rectangular patch antenna is considered, as shown in Fig. 4.23. The patch is fed by a $50\,\Omega$ microstrip transmission line (MTL) directly at the edge. A load impedance is inserted in the same way as in the previous example

(a) R $= 5\,\mathrm{mm}$ (b) R $= 17\,\mathrm{mm}$ (c) R $= 30\,\mathrm{mm}$
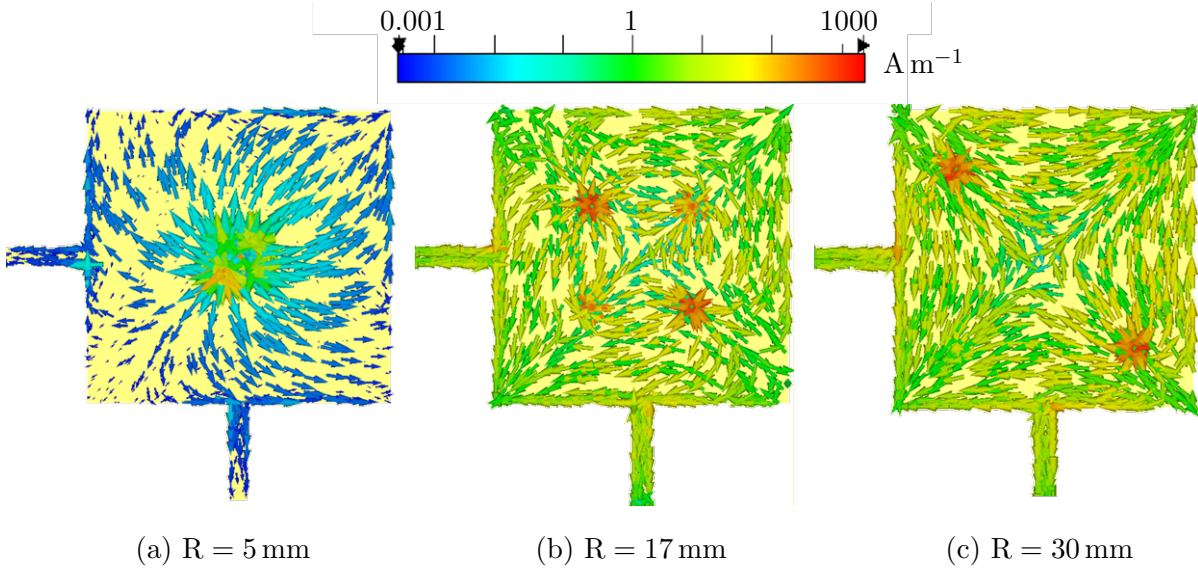
FIGURE 4.21: The surface current on the square patch for $\alpha = 45°$ and various radii of R [220].

(cf. Fig. 4.18 (a)-(b)) in order to match the antenna at $1\,\mathrm{GHz}$. Here, the idea is to see the behaviour of the load impedance, dependent on the load position over the whole patch. Since the value of the load impedance as it would be in a real scenario is not the focus here, all conductors are classified as perfect electric conductors (PEC) and the FR4 ($\epsilon_r = 4.3$) substrate is lossless as well. The substrate thickness is $2\,\mathrm{mm}$ and the length of the patch is L $= \lambda/2 = \lambda_0/2\sqrt{\epsilon_r} = 72.34\,\mathrm{mm}$, where λ_0 is the wavelength in free space. All other dimensions are shown in Fig. 4.23.

For an EMMPS with only one source and one load, (4.25) is easily solved after the load admittance to:

$$Y_L = \frac{r_1}{k_{11}} = \frac{Y_{sl}Y_{ls}}{Y_{ss} - Y_0} - Y_{ll}, \tag{4.31}$$

with the source admittance of $Y_0 = 20\,\mathrm{mS}$. The formula shows that, if the patch is inherently matched, which means $Y_{ss} = Y_0$ (real values), the load admittance approaches infinity, meaning a short circuit at the load port. For each point in the xy-plane on the patch, this formula is evaluated, thereby using the symmetry to the xz-plane. The coordinate system is given in Fig. 4.23. Then, the load impedance is calculated at $1\,\mathrm{GHz}$ and the result is plotted in Fig. 4.24, where (a) shows the real and (b) the imaginary part of the load impedance. Additionally, the black lines in the plots
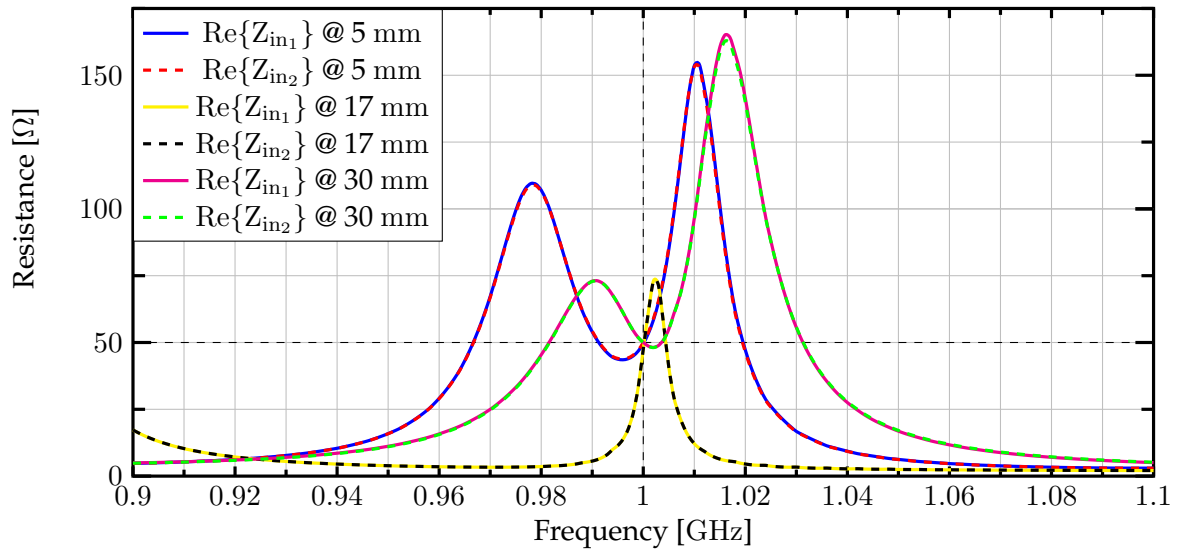
(a) Real part of the input impedances
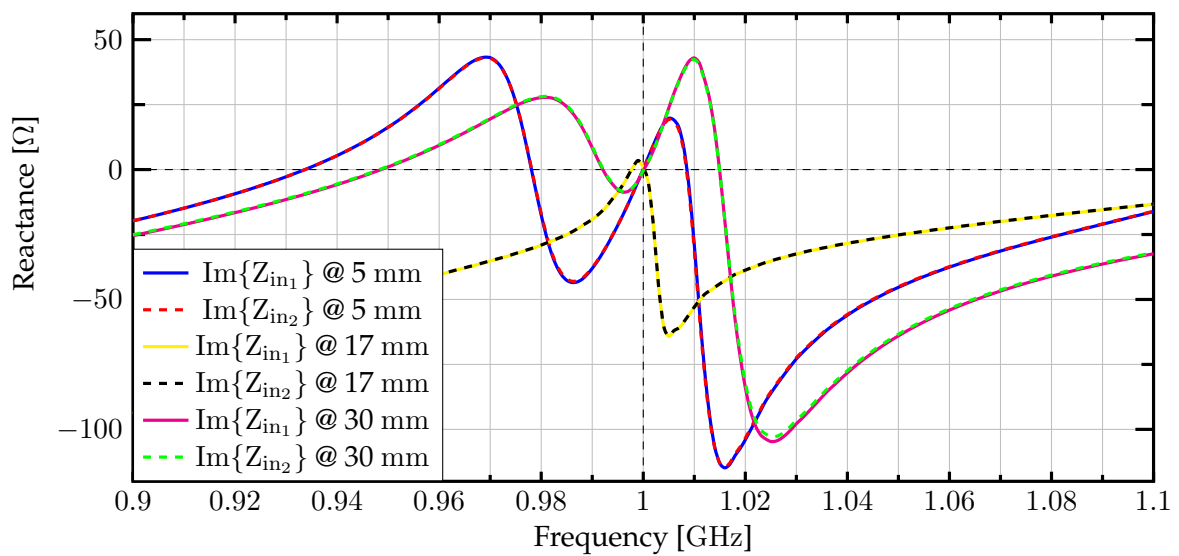
(b) Imaginary part of the input impedances

FIGURE 4.22: The input impedances Z_{in_1} and Z_{in_2} at both source ports (simultaneous feed) for different values of R over frequency [220].
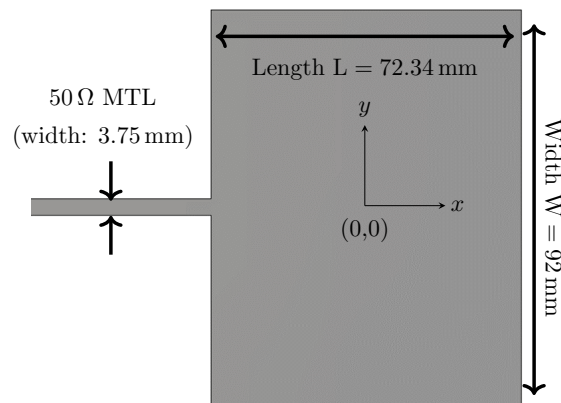
FIGURE 4.23: Layout and coordinate system of an edge-fed rectangular patch antenna[220].

indicate the patch antenna.

In Fig. 4.25 the load regions are shown. The white lines indicate at which locations the imaginary part of the load impedance becomes zero. At the same time, they mark the transition from one region to the other. Capacitive region means that in this region a capacitor must be used. Similarly, in the inductive region an inductor must be used. The dotted black lines show the locations where the real part of the load impedance becomes zero. Along these lines, lossless impedance matching is possible.

Fig. 4.26 depicts the surface current on the patch and the radiation characteristic in dBi in the xy-plane for two different locations. Both locations are chosen according to the load region plot, (Fig. 4.25) so that the real part of the load impedance is zero. Two very different locations are used, (a) at at the edge and (b) in the middle of the patch. As can be seen, the surface current distribution is much different between these two cases, also leading to two different radiation characteristics. In (b) it is interesting to mention that much of the power is radiated along the ground plane and not perpendicular to it, unlike a conventional patch antenna. The corresponding reflection coefficient over frequency of the case in (b) can be seen in the graph of Fig. 4.27 (blue curve, labeled with "1"). This curve shows a very narrow band behaviour since there are no losses.

Additionally for comparison, in Table 4.4 the load impedances along the line $y = 0$ are listed. The respective reflection coefficients are shown in Fig. 4.27. The labels in the legend are the same as is in the table. Table 4.4 also specifies the radiation efficiency for the particular load positions. The degradation of radiation efficiency is solely due

(a) Real part
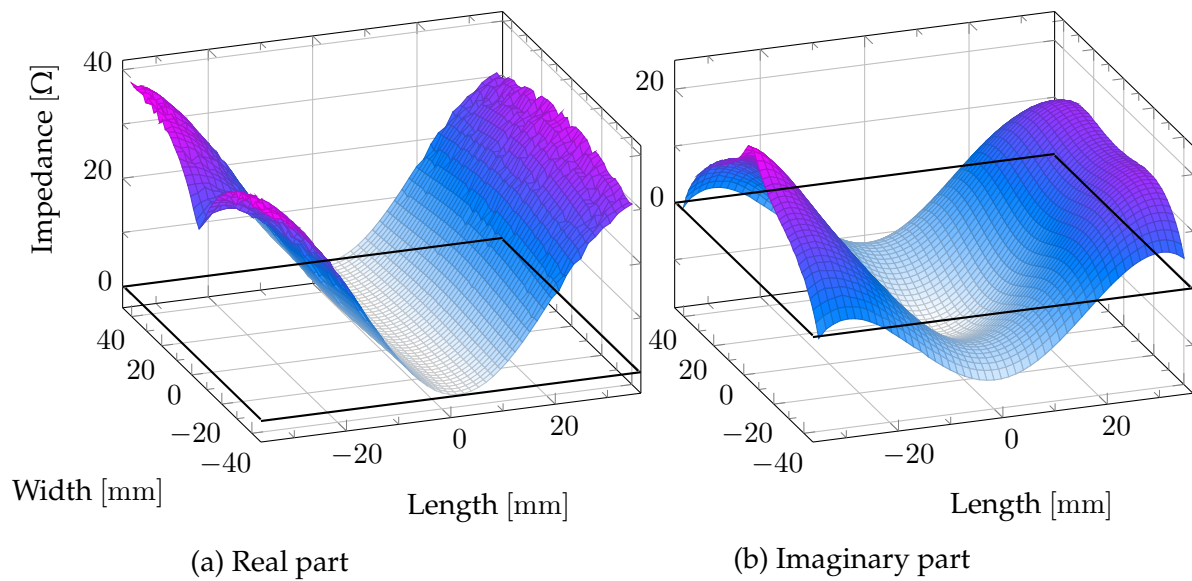
(b) Imaginary part

FIGURE 4.24: The real (a) and imaginary (b) part of the load impedance over its position within the rectangular patch [220].

TABLE 4.4: The calculated load impedances at different locations and the respective efficiencies of the rectangular patch antenna at $1\,\mathrm{GHz}$.

Label	Location (x, y)	Load impedance	Rad. efficiency
1	$(0.62\,\mathrm{mm}, 0\,\mathrm{mm})$	$-\mathrm{j}14.829\,\Omega$	$100\,\%$
2	$(7\,\mathrm{mm}, 0\,\mathrm{mm})$	$(2.144 - \mathrm{j}12.255)\Omega$	$18\,\%$
3	$(14\,\mathrm{mm}, 0\,\mathrm{mm})$	$(9.703 - \mathrm{j}5.204)\Omega$	$16\,\%$
4	$(21\,\mathrm{mm}, 0\,\mathrm{mm})$	$(19.36 + \mathrm{j}3.701)\Omega$	$15.5\,\%$
5	$(28\,\mathrm{mm}, 0\,\mathrm{mm})$	$(28.170 + \mathrm{j}11.067)\Omega$	$15.2\,\%$
6	$(35\,\mathrm{mm}, 0\,\mathrm{mm})$	$(34.74 + \mathrm{j}13.206)\Omega$	$14.9\,\%$

to the resistance in the load impedance since no losses are included in the simulation. These losses are also reflected in the bandwidth behaviour of the reflection coefficients in Fig. 4.27, which is much wider than in the case ("1"), where the resistance of the load impedance is zero.

4.3.2.3 Frequency Reconfiguration by Load Admittances of a Patch Antenna

In this example an edge-fed rectangular patch antenna after Fig. 4.23 is considered. To be able to reconfigure two different resonant frequencies, the patch is loaded with four susceptances. The loads are incorporated into the antenna as in the previous
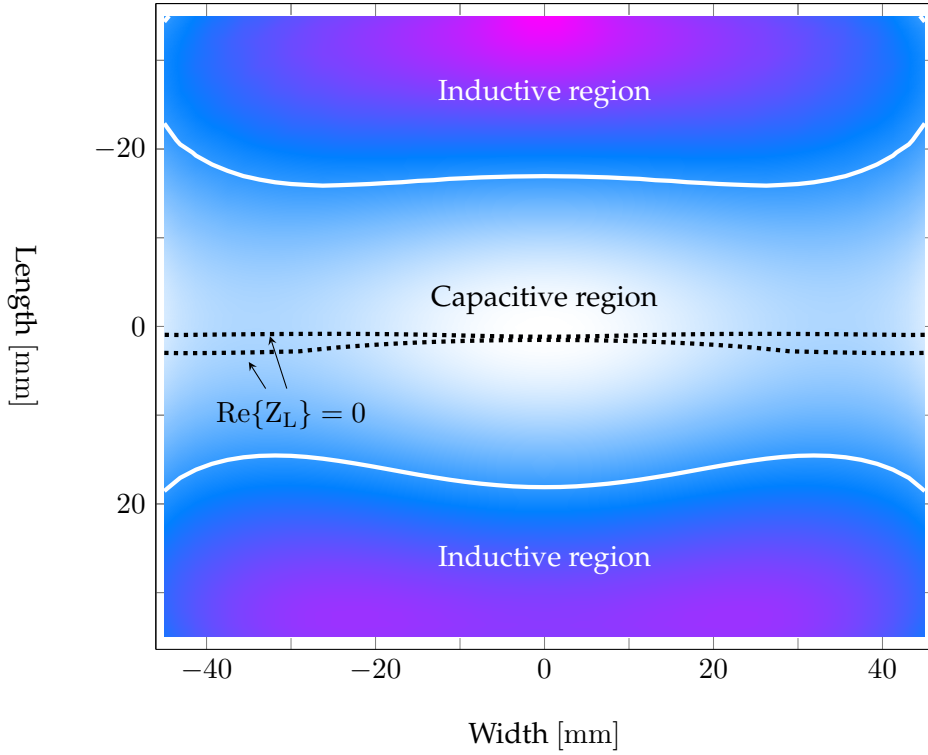
FIGURE 4.25: Load regions of the rectangular patch antenna. The white lines are indicating where the imaginary part and the black dotted lines where the real part of the load impedances become zero [220].

examples (cf. Fig. 4.18). The aim is purely lossless matching, which is the reason why four instead of two loads are required, leading to an $N = 4$, $M = 1$ EMMPS. For the first frequency $f_1 = 0.98\,\mathrm{GHz}$, the susceptances B_{L_1} and B_{L_2} should be active, while the others are open circuited ($B_{L_3} = B_{L_2} = 0$). For $f_2 = 0.98\,\mathrm{GHz}$, it is the other way around, and B_{L_1} and B_{L_2} are open circuited. According to (4.25), the following equations can be stated:

$$\mathrm{k}_{11}^{f_1} j B_{L_1} + \mathrm{k}_{12}^{f_1} j B_{L_2} - \mathrm{k}_{15}^{f_1} B_{L_1} B_{L_2} = \mathrm{r}_1^{f_1} \tag{4.32a}$$

$$\mathrm{k}_{13}^{f_2} j B_{L_3} + \mathrm{k}_{14}^{f_2} j B_{L_4} - \mathrm{k}_{1(10)}^{f_2} B_{L_3} B_{L_4} = \mathrm{r}_1^{f_2}. \tag{4.32b}$$

The superscripts indicate at which frequency (f_1 or f_2) the **K** matrix and the r̃ vector are evaluated. Obviously, these equations are independent of each other and each one is, in turn, fully determined when rewritten in a purely real valued equation system. Then:

$$\mathrm{Re}\{\mathrm{r}_1^{f_1}\} + \mathrm{Im}\{\mathrm{k}_{11}^{f_1}\} B_{L_1} + \mathrm{Im}\{\mathrm{k}_{12}^{f_1}\} B_{L_2} + \mathrm{Re}\{\mathrm{k}_{15}^{f_1}\} B_{L_1} B_{L_2} = 0 \tag{4.33a}$$
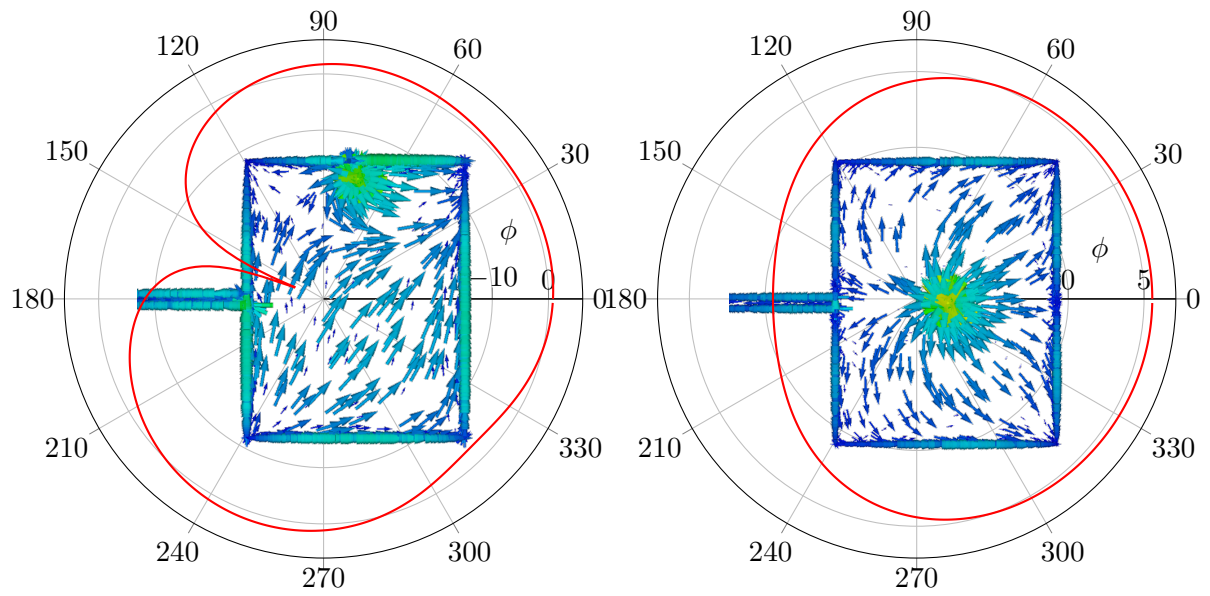
(a) Load location: ($x = 0.72\,\text{mm}, y = 40\,\text{mm}$)   (b) Load location: ($x = 0.62\,\text{mm}, y = 0\,\text{mm}$)

FIGURE 4.26: The gain in dBi in the xy-plane of the patch and the corresponding surface current on the patch for two different locations of load impedances [220].
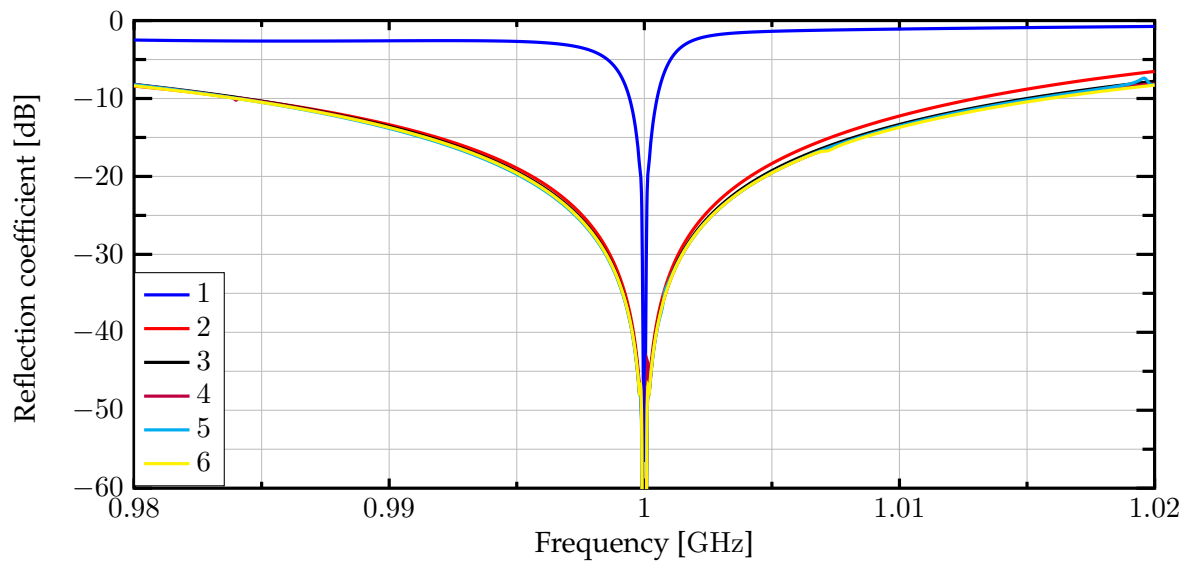
FIGURE 4.27: The reflection coefficient in dB over frequency for different locations of the load impedance after Table 4.4 [220].

$$\text{Im}\{r_1^{f_1}\} - \text{Re}\{k_{11}^{f_1}\}B_{L_1} - \text{Re}\{k_{12}^{f_1}\}B_{L_2} + \text{Im}\{k_{15}^{f_1}\}B_{L_1}B_{L_2} = 0 \tag{4.33b}$$

$$\text{Re}\{r_1^{f_2}\} + \text{Im}\{k_{13}^{f_2}\}B_{L_3} + \text{Im}\{k_{14}^{f_2}\}B_{L_4} + \text{Re}\{k_{1(10)}^{f_2}\}B_{L_3}B_{L_4} = 0 \tag{4.33c}$$

$$\text{Im}\{r_1^{f_2}\} - \text{Re}\{k_{13}^{f_2}\}B_{L_3} - \text{Re}\{k_{14}^{f_2}\}B_{L_4} + \text{Im}\{k_{1(10)}^{f_2}\}B_{L_3}B_{L_4} = 0 \tag{4.33d}$$

Finally, the analytic results are:

$$B_{L_1} = \frac{\text{Im}\{k_{11}^{f_1}(k_{12}^{f_1})^*\} + \text{Im}\{r_1^{f_1}(k_{15}^{f_1})^*\} \pm \sqrt{A}}{2\,\text{Re}\{k_{11}^{f_1}(k_{15}^{f_1})^*\}} \tag{4.34a}$$

$$B_{L_2} = \frac{\text{Im}\{(k_{11}^{f_1})^*k_{12}^{f_1}\} + \text{Im}\{r_1^{f_1}(k_{15}^{f_1})^*\} \mp \sqrt{A}}{2\,\text{Re}\{k_{12}^{f_1}(k_{15}^{f_1})^*\}} \tag{4.34b}$$

$$B_{L_3} = \frac{\text{Im}\{k_{13}^{f_2}(k_{14}^{f_2})^*\} + \text{Im}\{r_1^{f_2}(k_{1(10)}^{f_2})^*\} \pm \sqrt{B}}{2\,\text{Re}\{k_{13}^{f_2}(k_{1(10)}^{f_2})^*\}} \tag{4.34c}$$

$$B_{L_4} = \frac{\text{Im}\{(k_{13}^{f_2})^*k_{14}^{f_2}\} + \text{Im}\{r_1^{f_2}(k_{1(10)}^{f_2})^*\} \mp \sqrt{B}}{2\,\text{Re}\{k_{14}^{f_2}(k_{1(10)}^{f_2})^*\}} \tag{4.34d}$$

with:

$$A = \text{Im}\{k_{11}^{f_1}(k_{12}^{f_1})^*\}^2 + \text{Im}\{r_1^{f_1}(k_{15}^{f_1})^*\}^2$$
$$+ 2\,\text{Re}\{r_1^{f_1}(k_{11}^{f_1})^*\}\,\text{Re}\{k_{12}^{f_1}(k_{15}^{f_1})^*\} + 2\,\text{Re}\{r_1^{f_1}(k_{12}^{f_1})^*\}\,\text{Re}\{k_{11}^{f_1}(k_{15}^{f_1})^*\},$$

$$B = \text{Im}\{k_{13}^{f_2}(k_{14}^{f_2})^*\}^2 + \text{Im}\{r_1^{f_2}(k_{1(10)}^{f_2})^*\}^2$$
$$+ 2\,\text{Re}\{r_1^{f_2}(k_{13}^{f_2})^*\}\,\text{Re}\{k_{14}^{f_2}(k_{1(10)}^{f_2})^*\} + 2\,\text{Re}\{r_1^{f_2}(k_{14}^{f_2})^*\}\,\text{Re}\{k_{13}^{f_2}(k_{1(10)}^{f_2})^*\}.$$

As can be seen, if $A < 0$ then there are no solutions for B_{L_1} and B_{L_2}. The same applies to B, B_{L_3} and B_{L_4}. In Fig. 4.28, for each case the first solution of the load susceptances over frequency is depicted. In addition, the coloured areas indidcate the frequency ranges, with $A < 0$ and $B < 0$. Obviously, there are continuous solutions from $0.9\,\text{GHz}$ to $1.1\,\text{GHz}$. For f_1 and f_2 all susceptances are positive, meaning all loads are capacitors. In Table 4.5, the load locations, the theoretical capacitances and the ones that can be found off the shelf are listed. These values are inserted in the simulation to determine the reflection coefficients, which are given in Fig. 4.29. The dashed curves (blue for f_1 and cyan for f_2) show the reflection coefficients when the theoretical calculated capacitances are applied, while the solid curves show them when real available values

are used.

A prototype is manufactured as shown in the photograph of Fig. 4.30. The values of the load capacitors are chosen according to the real available values. In Fig. 4.30 (a) the top view of the whole patch is depicted, while (b) shows a zoom-in view on the load via area. (c) and (d) show the two cases, f_1 and f_2. To cover both scenarios, two PCB are manufactured, which differ only by load capacitors and their locations. In this way, the switching mechanism is conceptionally approximated. The measured reflection coefficient for the cases, f_1 and f_2 are shown in Fig. 4.29. A deviation from the simulation is evident but is still a reasonable measure since the whole structure has very narrow bandwidth. At this point, one critical issue should be mentioned: the dimensions of the load ports will understandably have significant impact on the load admittance values. Consequently, when the multi-port parameters are determined one should keep in mind to precisely define the port dimensions, especially if there is a narrow-band structure. In this work, the edge length of the load ports is set to $0.6\,\mathrm{mm}$ and the capacitor package is 0402, which has a width of about $0.5\,\mathrm{mm}$. In addition, the capacitances have a deviation in value of about $\pm 5\,\%$.

TABLE 4.5: The locations, the theoretical, and off the shelf values of the calculated load capacitors.

Cap.	Loc. (x, y) [mm]	Theo. val. [pF]	off the shelf val. [pF]
C_1	$(25, 15)$	9.7926	10
C_2	$(25, 5)$	19.4519	18
C_3	$(25, -5)$	5.9838	5.6
C_4	$(25, -15)$	24.7821	27

4.3.3 Discussion

The main outcome of the theory presented in this paper is a non-linear equation system, where, the solution variables are the load admittances of a multi port antenna with an arbitrary number of feed and load ports. If this equation system is fulfilled, complex conjugate impedance matching at all feed ports at one particular frequency is obtained. Further, it has been shown how this equation system simplifies when some
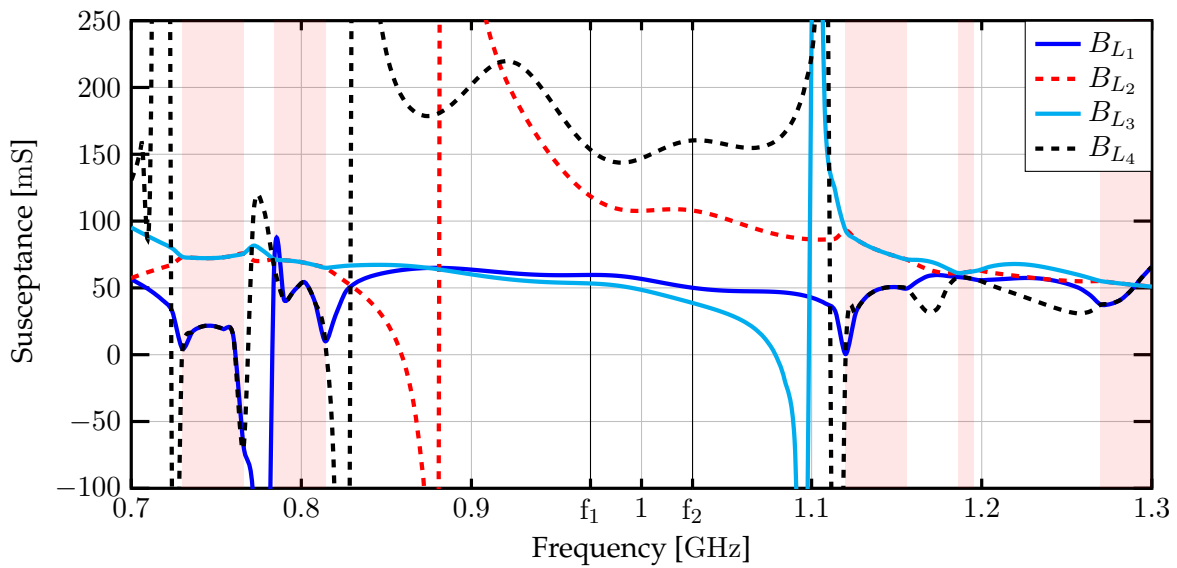
FIGURE 4.28: In each case the first solution of the load susceptances over frequency. The coloured areas are indicating the frequency range where, $A < 0$ and $B < 0$, therefore, in this range no valid solution is available [220].
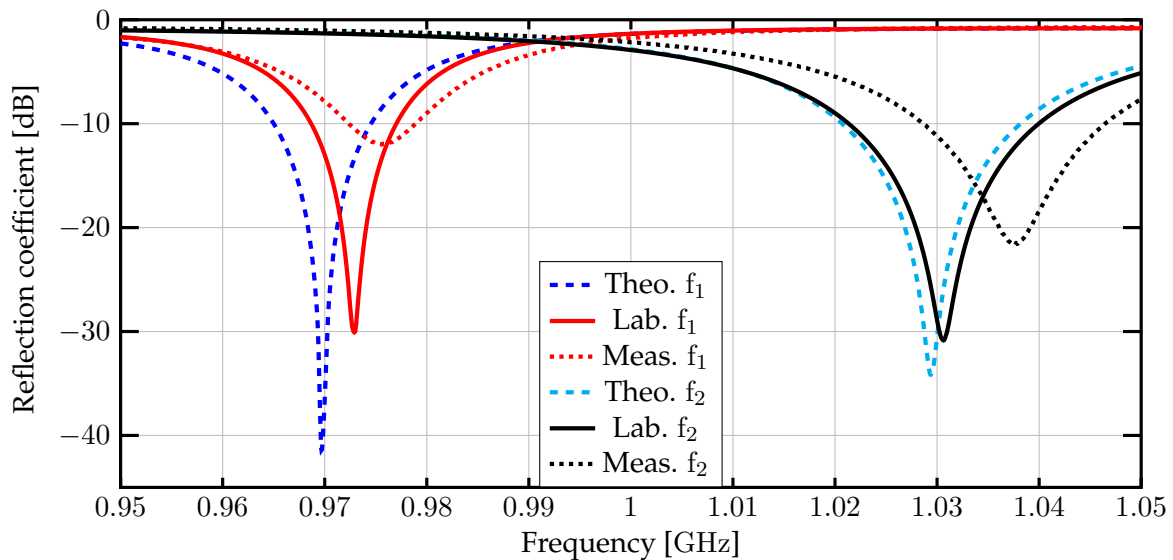
FIGURE 4.29: The reflection coefficient over frequency in dB, when the loads, according to Table 4.5 are inserted [220].
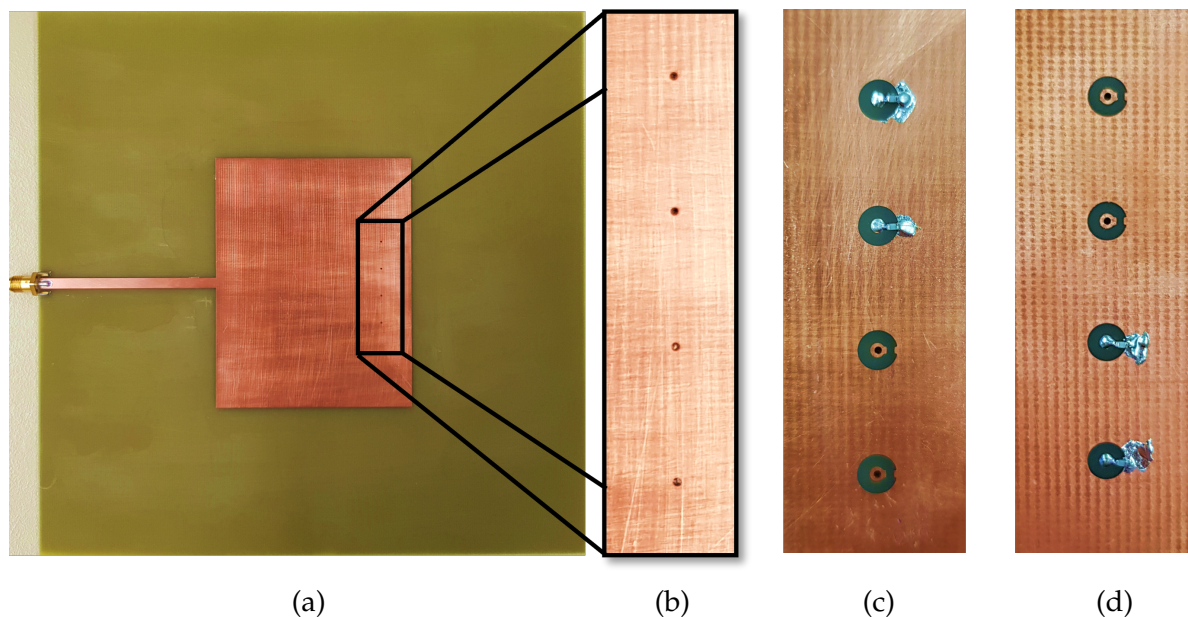
FIGURE 4.30: Photograph of the prototype; (a) top view, (b) top view with zoom into the load vias area, (c) the soldered capacitors for "f_1" and (d) the ones for "f_2" [220].

of the loads are switched off. One obvious finding is that two reactive components per feed port are required to realize lossless matching.

To verify the theory, three examples are presented. The first is a square patch antenna with two feed and four load ports. It is shown that with the four load components, which are calculated with the theory, both feed ports are losslessly matched. It is also shown how the loads change with location and over frequency. The second example deals with a single-fed rectangular patch antenna with only one load, for which the load impedance distribution over the whole structure is analytically determined. Regions are computed, in which the load is capacitive, and for other regions, inductive. Furthermore, two curves on the patch are found, on which the real part of the load is zero, meaning that at these locations, lossless matching with only one component is possible. In the third example, a single-fed rectangular patch antenna with four loads is considered, whereby two different frequencies should be reconfigurable. Therefore, for each frequency, two load components should serve, while the respective other two are excluded. Analytical formulae for the load admittances are given and verified by simulations and by measurements of prototypes.

This theory can be applied in many other antenna structures. Broadband structures in

which small changes, such as deviations in material parameters, component values, and production dimensions are within the bandwidth, are very promising. As well, further work should include the switching capability. The behaviour of these switches at the design frequency can be determined and included as known load admittances in the theory.

Chapter 5

Conclusion and Outlook

5.1 Conclusion

This thesis deals with the question of how an antenna can be made robust, adaptive, and immune or unaffected by environmental changes in its close vicinity. These changes impact antenna properties, such as antenna input impedance, radiation characteristic, polarization, and efficiency. The performance of a system depending on an antenna will reduce significantly over time. If the antenna input impedance changes, part of the power provided by the source (e.g. RF-chip) is reflected back. In a wireless transmission system, the alteration of the radiation pattern and polarization can potentially cause an interruption of the connection, since the power is wrongly directed. The deterioration of the antenna efficiency worsens the system efficiency as well. In this work, impedance mismatch due to environmental changes is considered. Two main threads are pursued: passive antennas and antennas loaded with active components.

Passive: The first approach is the resonant mode matching (RMM), while the second is a passive power divider network (PDN).

- Resonant mode matching: In this approach different resonant antennas are merged into a single structure. The merged structure shows as many resonant modes as the number of merged antennas, thereby each mode should cover one particular scenario. By geometric manipulation of the merged structure, the resonant frequency of each mode can be matched accordingly.

  A prototype is presented that uses the mode matching method for two scenarios,

namely, when the antenna is placed in free space and when it is placed close to a metal surface. Here, a coplanar patch antenna and a dipole slot antenna are merged to one single structure. The mode of the slot antenna covers the free space scenario, while the coplanar patch mode appears when the antenna is placed close to a metal surface. This prototype also covers the transition between the two scenarios, meaning the antenna can be place of any distance to the metal surface (from $4\,\mathrm{mm}$ to infinity). Measurements show that if the distance to the metal is greater than $4\,\mathrm{mm}$, the feed match remains better than -12 dB at a frequency of $4.85\,\mathrm{GHz}$. The far-field measurements show a dipole-like behaviour (omnidirectional) for the case of free space and a patch-like characteristic for the metal case, which verifies the feasibility of the resonant mode matching approach. This method is not a universal approach, since not all antenna types are mergeable. As well, for each mode the merged structure may show a worse performance compared to the corresponding single antenna.

The procedures reported in the literature which discuss using ground planes as insulator from the metal surface have disadvantages in comparison to the presented approach. Firstly, they have two layers and, secondly, the size of the ground plane determines the insulation from the metal surface. The larger the ground area, the smaller the influence of the surface. This leads to complex design processes (miniaturization) and/or large antenna structures. Other state-of-the-art approaches (e.g. high-input impedance or wide-band antennas) make antennas robust against the metal surface but do not cover the two extreme scenarios (on metal surface and in free space) perfectly.

- Power divider network: Two feed points of an antenna that each have very different input impedances for two different environments, so-called scenarios, are combined within a passive power divider network (PDN). This PDN is designed in such a way that for either scenario impedance matching at the PDN input is obtained. The idea is to control the power flow. In the first scenario, most of the power flows into the first antenna port, while for the second scenario, most of it flows into the second antenna port. The amount of the maximum power flow is dependent on the values of the antenna input impedances.

Analytical formulae for the PDN for arbitrary antenna input impedances are presented in this thesis. A prototype is designed, which combines the feeds of two mono poles of largely different lengths located very close to each other (strongly-coupled). Due to the PDN, this antenna radiates in free space, but also when the mono poles are completely immersed in butter, while being perfectly impedance matched to the source. Reflection coefficient measurements at the input of the PDN for either scenario show a value less than - 25 dB.

Theoretically, more feed points can be chosen to cover more than two scenarios. However, the structure then becomes very large, making the realization largely impractical.

An advantage over state-of-the-art approaches is that the PDN is independent of the radiating structure. Disadvantages of conventional antennas can be avoided in this way. For example, antennas with a ground plane or with spacer materials do not have to be used. In this way, the size and cost of the antenna can be reduced.

Active: The first approach is a differential antenna (DA) with different feed positions, while the second uses switched load admittances (SLA).

- Changing feed positions: This makes use of the fact that at different feed positions of a multiple fed differential antenna, the input impedance shows different values. Placing the antenna on top of a half-space of different materials (scenarios), will change the input impedances. Consequently, for each scenario a location of the feed can be found where the antenna is impedance matched to the source. Depending on the scenario, the feed position is changed by switches so that the antenna remains impedance matched for all the scenarios.

  Two challenges appear that are solved by the approach presented here. Firstly, the unwanted radiation of the differential feed line and, secondly, the small area on which, due to the small RF-chip size, the feed positions should be co-located. Three different scenarios (1. free space, 2. half-space filled with butter, and 3. half-space filled with minced meat) are covered by a triple-fed dipole-like antenna structure. The measured reflection coefficients of a stand-alone (without RF-chip) prototype for all three scenarios at $5.5\,\mathrm{GHz}$ show values less than - 20 dB. It is also

shown that the antenna is functional when connected to an RF-chip incorporated into a thin polymer foil, laying the base for a highly flexible wireless transmission system. The proposed concept can be adapted to other sets of scenarios.

However, more than three scenarios, meaning more than three feeds seems too involved and possibly unfeasible.

Several advantages over state-of-the-art approaches to multiple feed antennas are found. The presented design has three feed points close to each other, from which each of which the point covers one environmental scenario perfectly. This small feed area allows the antenna to be connected to an RF chip. Furthermore, the antenna is very flexible and consists of only one layer. This enables a large bandwidth, which in turn makes the antenna robust against bending (impedance variation within the bandwidth).

- Switched load admittances: A general theory is given that allows to calculation of load admittances of an arbitrary radiation structure in order to obtain impedance matching at all feed ports. The locations of the feed and load ports can be freely chosen. Upon an environmental change in the vicinity of the structure (scenario), load admittances can be switched to keep the feed ports matched. In the same way it is possible to alter the resonant frequency.

  A non-linear equation system is derived, in which the solution variables are the load admittances of the radiating structure. If this equation system is satisfied, a complex conjugate match at all feed ports is obtained. It is also shown how lossless matching (no losses in the loads) can be realized, if, each feed port has two reactive load admittances. A few examples are given showing some of many possible applications.

  The load admittances may lead to a high-density surface current at some specific locations, which degrades the performance in terms of bandwidth and efficiency. The equation system that is derived, in which the solution variables are the load admittances has been newly developed here and open up the possibility to enhance existing antenna design processes for reconfigurable antennas like pixel antennas. For a multiple-loaded reconfigurable antenna with two closed

switches (two load admittances are active) an analytical solution is presented for the first time.

Compared to active antennas, passive antennas have the advantage of being very reliable since no active components can cause failures. The absence of any components ensures easy production and simulation. No soldering or additional DC-biasing structure are required. In addition, the simulation is more trustworthy because there are no active components to consider. On the other hand, active antennas are not as limited as passive ones in terms of scenario coverage. Table 5.1 lists some pros and cons of each approach.

In conclusion, this work presents approaches for designing antennas for IoT sensors. The proposed designs are not only versatile and adaptable, but also highly effective in their ability to respond to changes in their environment. By implementing complex-conjugate impedance adaptation, the antenna is able to maintain optimal performance in a variety of different environments, making it an ideal choice for a wide range of IoT applications.

5.2 Outlook

The resonant mode matching method, the power divider network and the wire antenna with switched feeds are limited in the kind and number of scenarios where they may be used. Investigations can be pursued to apply the concepts to multiple scenarios and some practical limits of feasibility can be worked out. As well, the cons shown in Table 5.1 can be improved. The case of the single-layer antenna of the resonant mode matching method, techniques describe in the literature could serve to widen the bandwidth. Different solutions for reducing the PDN area might be found. This is possible because the theory does not provide only one solution.

A number of further investigations can be carried out with regards to the presented theory of switched-load admittances. A genetic algorithm can be applied in order to find the best solution in terms of the bandwidth. Such an algorithm can also be applied when the number of loads becomes very large, making the non-linear equation system

difficult to solve.

Ultimately, the theory also offers a lot of potential for other applications such as antenna arrays and tunable filters.

TABLE 5.1: Pros and cons of each of the four approaches.

	Pros	Cons
RMM	- Only one single layer. - Reliable antenna. - Easy to manufacture.	- Many simulation runs required. - Can cover only two scenarios. - Narrow bandwidth.
PDN	- Easy design process, since formulae are available. - Easy to manufacture. - Reliable antenna.	- Adds additional structure. - Can cover only two scenarios. - Adds losses.
DA	- Can cover more scenarios. - Straightforward approach. - Small occupied area. - Single-layer structure	- Several simulation runs required. - Manufacture is more complicated. - Soldering and bonding decrease the accuracy of the simulation. - DC-bias circuits.
SLA	- Can cover more scenarios. - May be applicable to other applications. - Straightforward approach by using formulae. - Less simulation effort. - Arbitrary antenna structure.	- Degradation of the performance possible. - Multiple possible solutions. - Manufacture is more complicated. - Soldering and bonding decrease the accuracy of the simulation. - DC- bias circuits.

Bibliography

[1] I. Analytics, *Internet of Things (IoT) and non-IoT active device connections worldwide from 2010 to 2025 (in billions). Statista.*, accessed: Mar. 15, 2022. ed., Statista Inc., 2020. [Online]. Available: https://www.statista.com/statistics/1101442/iot-number-of-connected-devices-worldwide/

[2] L. Chettri and R. Bera, "A comprehensive survey on internet of things (IoT) toward 5g wireless systems," *IEEE Internet of Things Journal*, vol. 7, no. 1, pp. 16–32, Jan. 2020. doi: 10.1109/jiot.2019.2948888

[3] A. Čolaković and M. Hadžialić, "Internet of things (IoT): A review of enabling technologies, challenges, and open research issues," *Computer Networks*, vol. 144, pp. 17–39, Oct. 2018. doi: 10.1016/j.comnet.2018.07.017

[4] D. Ferreira, P. Pires, R. Rodrigues, and R. F. S. Caldeirinha, "Wearable textile antennas: Examining the effect of bending on their performance." *IEEE Antennas and Propagation Magazine*, vol. 59, pp. 54–59, 2017. doi: 10.1109/map.2017.2686093

[5] L. Song and Y. Rahmat-Samii, "A systematic investigation of rectangular patch antenna bending effects for wearable applications," *IEEE Transactions on Antennas and Propagation*, vol. 66, pp. 2219–2228, 2018. doi: 10.1109/tap.2018.2809469

[6] S. Sankaralingam and B. Gupta, "Effects of bending on impedance and radiation characteristics of rectangular wearable antenna utilizing smart clothes," *Microwave and Optical Technology Letters*, vol. 54, no. 6, pp. 1508–1511, Mar. 2012. doi: 10.1002/mop.26849

[7] F. Boeykens, L. Vallozzi, and H. Rogier, "Cylindrical bending of deformable textile rectangular patch antennas," *International Journal of Antennas and Propagation*, vol. 2012, pp. 1–11, 2012. doi: 10.1155/2012/170420

[8] Q. Bai and R. Langley, "Textile antenna bending and crumpling," in *Proceedings of the Fourth European Conference on Antennas and Propagation*, 2010, 2010, pp. 1–4.

[9] P. Salonen, M. Keskilammi, and Y. Rahmat-Samii, "Textile antennas: Effect of antenna bending on radiation pattern and efficiency," in *2008 IEEE Antennas and Propagation Society International Symposium*, Jul. 2008. doi: 10.1109/aps.2008.4619343

[10] N. Amaro, C. Mendes, and P. Pinho, "Bending effects on a textile microstrip antenna," in *2011 IEEE International Symposium on Antennas and Propagation (APSURSI)*, Jul. 2011. doi: 10.1109/aps.2011.5996697

[11] H. P. Phan, T.-P. Vuong, P. Benech, P. Xavier, and P. Borel, "Study of bending effects of a wideband paper-based printed microstrip-fed antenna," *Microwave and Optical Technology Letters*, vol. 62, no. 4, pp. 1785–1794, Jan. 2020. doi: 10.1002/mop.32233

[12] E. B. Daculan, "Bending the dipole," in *2014 5th International Conference on Intelligent Systems, Modelling and Simulation*, Jan. 2014. doi: 10.1109/isms.2014.124

[13] S. Dey, N. Saha, and S. Biswas, "Design and performance analysis of uwb circular disc monopole textile antenna and bending consequences," in *Proceedings of the 5th European Conference on Antennas and Propagation (EUCAP)*, 2011, 2011, pp. 1129–1133.

[14] H.-L. Kao, C.-L. Cho, X. Y. Zhang, L.-C. Chang, B.-H. Wei, X. Dai, and H.-C. Chiu, "Bending effect of an inkjet-printed series-fed two-dipole antenna on a liquid crystal polymer substrate," *IEEE Antennas and Wireless Propagation Letters*, vol. 13, pp. 1172–1175, Jan. 2014. doi: 10.1109/LAWP.2014.2330819

[15] L. Jianying, D. Fang, Z. Yichen, Y. Xin, C. Lulu, Z. Panpan, and W. Mengjun, "Bending effects on a flexible yagi-uda antenna for wireless body area network," in *2016 Asia-Pacific International Symposium on Electromagnetic Compatibility (APEMC)*, May 2016. doi: 10.1109/apemc.2016.7522928

[16] J. Siden, P. Jonsson, T. Olsson, and G. Wang, "Performance degradation of RFID system due to the distortion in RFID tag antenna," in *11th International Conference 'Microwave and Telecommunication Technology'. Conference Proceedings (IEEE Cat. No.01EX487)*, 2001. doi: 10.1109/crmico.2001.961592

[17] M. E. Bakkali, M. Martinez-Estrada, R. Fernandez-Garcia, I. Gil, and O. E. Mrabet, "Effect of bending on a textile UHF-RFID tag antenna," in *2020 14th European Conference on Antennas and Propagation (EuCAP)*, Mar. 2020. doi: 10.23919/eu-cap48036.2020.9135331

[18] M. Haerinia and S. Noghanian, "Study of bending effects on a dual-band implantable antenna," in *2019 IEEE International Symposium on Antennas and Propagation and USNC-URSI Radio Science Meeting*, Jul. 2019. doi: 10.1109/apusncursinrsm.2019.8888320

[19] A. Mersani, L. Osman, and J.-M. Ribero, "Effect of bending on the characteristics of a coplanar textile antenna," in *2018 18th Mediterranean Microwave Symposium (MMS)*, Oct. 2018. doi: 10.1109/mms.2018.8612049

[20] H. A. Mashaghba, H. A. Rahim, P. J. Soh, M. Abdulmalek, I. Adam, M. Jusoh, T. Sabapathy, M. N. M. Yasin, and K. N. A. Rani, "Bending assessment of dual-band split ring-shaped and bar slotted all-textile antenna for off-body WBAN/WLAN and 5g applications," in *2020 2nd International Conference on Broadband Communications, Wireless Sensors and Powering (BCWSP)*, Sep. 2020. doi: 10.1109/bcwsp50066.2020.9249403

[21] M. Kubo, X. Li, C. Kim, M. Hashimoto, B. J. Wiley, D. Ham, and G. M. Whitesides, "Stretchable microfluidic radiofrequency antennas," *Advanced Materials*, vol. 22, no. 25, pp. 2749–2752, Apr. 2010. doi: 10.1002/adma.200904201

[22] S. J. Mazlouman, X. J. Jiang, A. Mahanfar, C. Menon, and R. G. Vaughan, "A reconfigurable patch antenna using liquid metal embedded in a silicone substrate," *IEEE Transactions on Antennas and Propagation*, vol. 59, no. 12, pp. 4406–4412, Dec. 2011. doi: 10.1109/tap.2011.2165501

[23] S. Masihi, M. Panahi, D. Maddipatla, A. K. Bose, X. Zhang, A. J. Hanson, B. B. Narakathu, B. J. Bazuin, and M. Z. Atashbar, "Development of a flexible tunable and compact microstrip antenna via laser assisted patterning of copper film," *IEEE Sensors Journal*, vol. 20, no. 14, pp. 7579–7587, Jul. 2020. doi: 10.1109/jsen.2020.2987318

[24] T. Rashid, S. Noghanian, R. Fazel-Rezai, and P. de Leon, "Stretching effect on textile antenna for spacesuit," in *2016 IEEE International Symposium on Antennas and Propagation (APSURSI)*, Jun. 2016. doi: 10.1109/aps.2016.7696206

[25] H. Saghlatoon, M. M. Honari, R. Mirzavand, P. Mousavi, A. Kumar, T. G. La, and H.-J. Chung, "A novel investigation on printed stretchable WLAN antennas," in *2017 IEEE International Symposium on Antennas and Propagation & USNC/URSI National Radio Science Meeting*, Jul. 2017. doi: 10.1109/apusncursinrsm.2017.8073311

[26] J.-H. So, J. Thelen, A. Qusba, G. J. Hayes, G. Lazzi, and M. D. Dickey, "Reversibly deformable and mechanically tunable fluidic antennas," *Advanced Functional Materials*, vol. 19, no. 22, pp. 3632–3637, Nov. 2009. doi: 10.1002/adfm.200900604

[27] Q. Liu, K. L. Ford, R. Langley, A. Robinson, and S. Lacour, "Stretchable antennas," in *2012 6th European Conference on Antennas and Propagation (EUCAP)*, Mar. 2012. doi: 10.1109/eucap.2012.6206109

[28] X. Chen, A. Liu, Z. Wei, L. Ukkonen, and J. Virkki, "Experimental study on strain reliability of embroidered passive UHF RFID textile tag antennas and interconnections," *Journal of Engineering*, vol. 2017, pp. 1–7, 2017. doi: 10.1155/2017/8493405

[29] T. Bjorninen, J. Virkki, L. Sydanheimo, and L. Ukkonen, "Impact of recurrent stretching on the performance of electro-textile UHF RFID tags," in *Proceedings of the 5th Electronics System-integration Technology Conference (ESTC)*, Sep. 2014. doi: 10.1109/estc.2014.6962807

[30] X. D. Zhang, M. H. Yang, J. Virkki, T. Bjorninen, S. Merilampi, L. Sydanheimo, Y.-C. Chan, and L. Ukkonen, "Impact of antenna-fiber alignment and recurrent

stretching on the performance of passive UHF RFID tags based on textile antennas," in *2014 IEEE MTT-S International Microwave Workshop Series on RF and Wireless Technologies for Biomedical and Healthcare Applications (IMWS-Bio2014)*, Dec. 2014. doi: 10.1109/imws-bio.2014.7032384

[31] T. Jang, C. Zhang, H. Youn, J. Zhou, and L. J. Guo, "Semitransparent and flexible mechanically reconfigurable electrically small antennas based on tortuous metallic micromesh," *IEEE Transactions on Antennas and Propagation*, vol. 65, no. 1, pp. 150–158, Jan. 2017. doi: 10.1109/tap.2016.2623479

[32] G. Diotallevi, C. Miozzi, M. Cirelli, P. P. Valentini, and G. Marrocco, "Radio-mechanical model of epidermal antenna stretching during human gestures," in *2019 IEEE International Conference on Flexible and Printable Sensors and Systems (FLEPS)*, Jul. 2019. doi: 10.1109/fleps.2019.8792315

[33] S. J. Mazlouman, C. Menon, R. G. Vaughan, and A. Mahanfar, "Stretchable antennas: An overview," in *2013 IEEE Antennas and Propagation Society International Symposium (APSURSI)*, Jul. 2013. doi: 10.1109/aps.2013.6711291

[34] Z. Xie, R. Avila, Y. Huang, and J. A. Rogers, "Flexible and stretchable antennas for biointegrated electronics," *Advanced Materials*, vol. 32, no. 15, p. 1902767, Sep. 2019. doi: 10.1002/adma.201902767

[35] G. Pedersen, K. Olesen, and S. Larsen, "Bodyloss for handheld phones," in *49th Vehicular Technology Conference*, 1999. doi: 10.1109/vetec.1999.780654

[36] K. R. Boyle, Y. Yuan, and L. P. Ligthart, "Analysis of mobile phone antenna impedance variations with user proximity," *IEEE Transactions on Antennas and Propagation*, vol. 55, no. 2, pp. 364–372, Feb. 2007. doi: 10.1109/tap.2006.889834

[37] M. Okoniewski and M. Stuchly, "A study of the handset antenna and human body interaction," *IEEE Transactions on Microwave Theory and Techniques*, vol. 44, no. 10, pp. 1855–1864, 1996. doi: 10.1109/22.539944

[38] P. Foster, "Antenna problems in RFID systems," in *IEE Colloquium. RFID Technology*, 1999. doi: 10.1049/ic:19990676

[39] D. Dobkin and S. Weigand, "Environmental effects on RFID tag antennas," in *IEEE MTT-S International Microwave Symposium Digest, 2005.*, 2005. doi: 10.1109/mwsym.2005.1516541

[40] G. Smith, "Directive properties of antennas for transmission into a material half-space," *IEEE Transactions on Antennas and Propagation*, vol. 32, no. 3, pp. 232–246, Mar. 1984. doi: 10.1109/tap.1984.1143307

[41] C. Warren, N. Chiwaridzo, and A. Giannopoulos, "Radiation characteristics of a high-frequency antenna in different dielectric environments," in *Proceedings of the 15th International Conference on Ground Penetrating Radar*, Jun. 2014. doi: 10.1109/icgpr.2014.6970529

[42] Y. Ziyuan, H. Xiaoxiang, Y. Yang, and T. Liu, "UHF RFID tag antenna performance on various dielectric-background," in *2016 IEEE International Workshop on Electromagnetics: Applications and Student Innovation Competition (iWEM)*, May 2016. doi: 10.1109/iwem.2016.7504964

[43] S. K. Behera and N. C. Karmakar, "Wearable chipless radio-frequency identification tags for biomedical applications: A review [antenna applications corner]," *IEEE Antennas and Propagation Magazine*, vol. 62, no. 3, pp. 94–104, Jun. 2020. doi: 10.1109/map.2020.2983978

[44] J. D. Griffin, G. D. Durgin, A. Haldi, and B. Kippelen, "RF tag antenna performance on various materials using radio link budgets," *IEEE Antennas and Wireless Propagation Letters*, vol. 5, pp. 247–250, 2006. doi: 10.1109/lawp.2006.874072

[45] B. Ivsic, G. Golemac, and D. Bonefacic, "Performance of wearable antenna exposed to adverse environmental conditions," in *ICECom 2013*, Oct. 2013. doi: 10.1109/icecom.2013.6684727

[46] J. Lilja, P. Salonen, T. Kaija, and P. de Maagt, "Design and manufacturing of robust textile antennas for harsh environments," *IEEE Transactions on Antennas and Propagation*, vol. 60, no. 9, pp. 4130–4140, Sep. 2012. doi: 10.1109/tap.2012.2207035

[47] I. Bahl, P. Bhartia, and S. Stuchly, "Design of microstrip antennas covered with a dielectric layer," *IEEE Transactions on Antennas and Propagation*, vol. 30, no. 2, pp. 314–318, Mar. 1982. doi: 10.1109/tap.1982.1142766

[48] R. Shavit, "Dielectric cover effect on rectangular microstrip antenna array," *IEEE Transactions on Antennas and Propagation*, vol. 42, no. 8, pp. 1180–1184, 1994. doi: 10.1109/8.310012

[49] D. Rano, M. A. Chaudhary, and M. S. Hashmi, "A new model to determine effective permittivity and resonant frequency of patch antenna covered with multiple dielectric layers," *IEEE Access*, vol. 8, pp. 34 418–34 430, 2020. doi: 10.1109/access.2020.2974912

[50] A. Soares, S. Fonseca, and A. Giarola, "The effect of a dielectric cover on the current distribution and input impedance of printed dipoles," *IEEE Transactions on Antennas and Propagation*, vol. 32, no. 11, pp. 1149–1153, Nov. 1984. doi: 10.1109/tap.1984.1143241

[51] M. Bailey, "Design of dielectric-covered resonant slots in a rectangular waveguide," *IEEE Transactions on Antennas and Propagation*, vol. 15, no. 5, pp. 594–598, Sep. 1967. doi: 10.1109/tap.1967.1139023

[52] M. Bailey and C. Swift, "Input admittance of a circular waveguide aperture covered by a dielectric slab," *IEEE Transactions on Antennas and Propagation*, vol. 16, no. 4, pp. 386–391, Jul. 1968. doi: 10.1109/tap.1968.1139207

[53] M. Bailey, "The impedance properties of dielectric-covered narrow radiating slots in the broad face of a rectangular waveguide," *IEEE Transactions on Antennas and Propagation*, vol. 18, no. 5, pp. 596–603, Sep. 1970. doi: 10.1109/tap.1970.1139761

[54] F. Casado, A. Arriolar, E. Arruti, J. Parron, I. Ortego, and I. Sancho, "2.45 GHz printed IFA on metallic environments: Clearance distance and retuning considerations," in *2012 6th European Conference on Antennas and Propagation (EUCAP)*, Mar. 2012. doi: 10.1109/eucap.2012.6205978

[55] P. Raumonen, L. Sydanheimo, L. Ukkonen, M. Keskilammi, and M. Kivikoski, "Folded dipole antenna near metal plate," in *IEEE Antennas and Propagation Society International Symposium. Digest. Held in conjunction with: USNC/C-NC/URSI North American Radio Sci. Meeting (Cat. No.03CH37450)*, 2003. doi: 10.1109/aps.2003.1217593

[56] J. Prothro, G. Durgin, and J. Griffin, "The effects of a metal ground plane on RFID tag antennas," in *2006 IEEE Antennas and Propagation Society International Symposium*, 2006. doi: 10.1109/aps.2006.1711302

[57] N. Ghannay, M. B. B. Salah, F. Romdhani, and A. Samet, "Effects of metal plate to RFID tag antenna parameters," in *2009 Mediterrannean Microwave Symposium (MMS)*, Nov. 2009. doi: 10.1109/mms.2009.5409801

[58] J. Ruyle, "Investigation on placement sensitivity of meandered dipole performance for RFID systems," in *Proceedings of the 2012 IEEE International Symposium on Antennas and Propagation*, Jul. 2012. doi: 10.1109/aps.2012.6349261

[59] L. Mo and H. Zhang, "RFID antenna near the surface of metal," in *2007 International Symposium on Microwave, Antenna, Propagation and EMC Technologies for Wireless Communications*, Aug. 2007. doi: 10.1109/mape.2007.4393746

[60] L. Mo, H. Zhang, and H. Zhou, "Analysis of dipole-like ultra high frequency RFID tags close to metallic surfaces," *Journal of Zhejiang University-SCIENCE A*, vol. 10, no. 8, pp. 1217–1222, Aug. 2009. doi: 10.1631/jzus.a0820495

[61] X. Qing and Z. N. Chen, "Proximity effects of metallic environments on high frequency RFID reader antenna: Study and applications," *IEEE Transactions on Antennas and Propagation*, vol. 55, no. 11, pp. 3105–3111, Nov. 2007. doi: 10.1109/tap.2007.908575

[62] J.-K. Kim, I.-Y. Oh, T.-W. Koo, J.-C. Kim, D.-S. Kim, and J.-G. Yook, "Effects of a metal plane on a meandered slot antenna for UHF RFID applications," *Journal of electromagnetic engineering and science*, vol. 12, no. 2, pp. 176–184, Jun. 2012. doi: 10.5515/jkiees.2012.12.2.176

[63] B. Hu, G.-P. Gao, L.-L. He, X.-D. Cong, and J.-N. Zhao, "Bending and on-arm effects on a wearable antenna for 2.45 ghz body area network," *IEEE Antennas and Wireless Propagation Letters*, vol. 15, pp. 378–381, 2016. doi: 10.1109/lawp.2015.2446512

[64] S. Cheng, Z. Wu, P. Hallbjorner, K. Hjort, and A. Rydberg, "Foldable and stretchable liquid metal planar inverted cone antenna," *IEEE Transactions on Antennas and Propagation*, vol. 57, no. 12, pp. 3765–3771, Dec. 2009. doi: 10.1109/tap.2009.2024560

[65] S. Cheng, A. Rydberg, K. Hjort, and Z. Wu, "Liquid metal stretchable unbalanced loop antenna," *Applied Physics Letters*, vol. 94, no. 14, p. 144103, Apr. 2009. doi: 10.1063/1.3114381

[66] A. M. Hussain, F. A. Ghaffar, S. I. Park, J. A. Rogers, A. Shamim, and M. M. Hussain, "Metal/polymer based stretchable antenna for constant frequency far-field communication in wearable electronics," *Advanced Functional Materials*, vol. 25, no. 42, pp. 6565–6575, Oct. 2015. doi: 10.1002/adfm.201503277

[67] F.-X. Liu, Z. Xu, D. C. Ranasinghe, and C. Fumeaux, "Textile folded half-mode substrate-integrated cavity antenna," *IEEE Antennas and Wireless Propagation Letters*, vol. 15, pp. 1693–1697, 2016. doi: 10.1109/lawp.2016.2524458

[68] T. Dissanayake, K. Esselle, and M. Yuce, "Dielectric loaded impedance matching for wideband implanted antennas," *IEEE Transactions on Microwave Theory and Techniques*, vol. 57, no. 10, pp. 2480–2487, Oct. 2009. doi: 10.1109/tmtt.2009.2029664

[69] P. Soontornpipit, C. Furse, and Y. Chung, "Design of implantable microstrip antenna for communication with medical implants," *IEEE Transactions on Microwave Theory and Techniques*, vol. 52, no. 8, pp. 1944–1951, Aug. 2004. doi: 10.1109/tmtt.2004.831976

[70] T. Deleruyelle, P. Pannier, M. Egels, and E. Bergeret, "An RFID tag antenna tolerant to mounting on materials," *IEEE Antennas and Propagation Magazine*, vol. 52, no. 4, pp. 14–19, Aug. 2010. doi: 10.1109/map.2010.5638229

[71] R. Luomaniemi, P. Yla-Oijala, A. Lehtovuori, and V. Viikari, "Designing hand-immune handset antennas with adaptive excitation and characteristic modes," *IEEE Transactions on Antennas and Propagation*, vol. 69, no. 7, pp. 3829–3839, Jul. 2021. doi: 10.1109/tap.2020.3044640

[72] J.-M. Hannula, J. Holopainen, and V. Viikari, "Concept for frequency-reconfigurable antenna based on distributed transceivers," *IEEE Antennas and Wireless Propagation Letters*, vol. 16, pp. 764–767, 2017. doi: 10.1109/lawp.2016.2602006

[73] J.-M. Hannula, T. Saarinen, J. Holopainen, and V. Viikari, "Frequency reconfigurable multiband handset antenna based on a multichannel transceiver," *IEEE Transactions on Antennas and Propagation*, vol. 65, no. 9, pp. 4452–4460, Sep. 2017. doi: 10.1109/tap.2017.2725384

[74] S. B. Fischer and J. Hesselbarth, "Power divider network for dual-fed adaptive antenna," *International Journal of Microwave and Wireless Technologies*, pp. 1–8, Mar. 2022. doi: 10.1017/s175907872200040x

[75] T. Bjorninen, L. Sydanheimo, L. Ukkonen, and Y. Rahmat-Samii, "Advances in antenna designs for UHF RFID tags mountable on conductive items," *IEEE Antennas and Propagation Magazine*, vol. 56, no. 1, pp. 79–103, Feb. 2014. doi: 10.1109/map.2014.6821761

[76] Y. J. Zhang, D. Wang, and M. S. Tong, "An adjustable quarter-wavelength meandered dipole antenna with slotted ground for metallically and airily mounted RFID tag," *IEEE Transactions on Antennas and Propagation*, vol. 65, no. 6, pp. 2890–2898, Jun. 2017. doi: 10.1109/tap.2017.2690535

[77] S. R. Best, "Improving the performance properties of a dipole element closely spaced to a PEC ground plane," *IEEE Antennas and Wireless Propagation Letters*, vol. 3, pp. 359–363, 2004. doi: 10.1109/lawp.2004.840722

[78] M. Polivka, M. Svanda, and P. Cerny, "Multiple-arm folded monopole antenna operating extremely close to a conductive plane," in *2008 14th Conference on Microwave Techniques*, Apr. 2008. doi: 10.1109/comite.2008.4569894

[79] Y. Nakagawa, S. Tanaka, T. Toba, K. Matsushita, and H. Morishita, "Near-metal-insensitive antenna for closed space wireless communications," *IEICE Communications Express*, vol. 6, no. 11, pp. 621–626, 2017. doi: 10.1587/comex.2017xbl0117

[80] S. B. Fischer and J. Hesselbarth, "A single-layer planar antenna unaffected by a possibly close-by metal surface," in *14th European Conference on Antennas and Propagation (EuCAP)*, Mar. 2020, Mar. 2020, pp. 1–5. doi: 10.23919/eucap48036.2020.9136072

[81] K. Karthika and K. Kavitha, "Reconfigurable antennas for advanced wireless communications: A review," *Wireless Personal Communications*, vol. 120, no. 4, pp. 2711–2771, May 2021. doi: 10.1007/s11277-021-08555-4

[82] M. Srivastava and A. Kumar, "A review paper on reconfigurable antenna technique and methodology," in *Emerging Technologies in Data Mining and Information Security*. Springer Singapore, 2021, pp. 605–615.

[83] C. G. Christodoulou, Y. Tawk, S. A. Lane, and S. R. Erwin, "Reconfigurable antennas for wireless and space applications," *Proceedings of the IEEE*, vol. 100, no. 7, pp. 2250–2261, Jul. 2012. doi: 10.1109/jproc.2012.2188249

[84] J. Costantine, Y. Tawk, S. E. Barbin, and C. G. Christodoulou, "Reconfigurable antennas: Design and applications," *Proceedings of the IEEE*, vol. 103, no. 3, pp. 424–437, Mar. 2015. doi: 10.1109/jproc.2015.2396000

[85] G. Oliveri, D. H. Werner, and A. Massa, "Reconfigurable electromagnetics through metamaterials—a review," *Proceedings of the IEEE*, vol. 103, no. 7, pp. 1034–1056, Jul. 2015. doi: 10.1109/jproc.2015.2394292

[86] R. L. Haupt and M. Lanagan, "Reconfigurable antennas," *IEEE Antennas and Propagation Magazine*, vol. 55, no. 1, pp. 49–61, Feb. 2013. doi: 10.1109/map.2013.6474484

[87] H. Rajagopalan, J. M. Kovitz, and Y. Rahmat-Samii, "MEMS reconfigurable optimized e-shaped patch antenna design for cognitive radio," *IEEE Transactions on Antennas and Propagation*, vol. 62, no. 3, pp. 1056–1064, Mar. 2014. doi: 10.1109/tap.2013.2292531

[88] G. Srivastava, A. Mohan, and A. Chakrabarty, "Compact reconfigurable UWB slot antenna for cognitive radio applications," *IEEE Antennas and Wireless Propagation Letters*, vol. 16, pp. 1139–1142, 2017. doi: 10.1109/lawp.2016.2624736

[89] R. Venkatesan and S. Raghavan, "A compact metamaterial inspired triple band antenna for reconfigurable WLAN/WiMAX applications," *AEU - International Journal of Electronics and Communications*, vol. 69, no. 1, pp. 274–280, Jan. 2015. doi: 10.1016/j.aeue.2014.09.012

[90] X. Zhao, S. Riaz, and S. Geng, "A reconfigurable MIMO/UWB MIMO antenna for cognitive radio applications," *IEEE Access*, vol. 7, pp. 46 739–46 747, 2019. doi: 10.1109/access.2019.2909810

[91] H. F. Abutarboush, R. Nilavalan, S. W. Cheung, K. M. Nasr, T. Peter, D. Budimir, and H. Al-Raweshidy, "A reconfigurable wideband and multiband antenna using dual-patch elements for compact wireless devices," *IEEE Transactions on Antennas and Propagation*, vol. 60, no. 1, pp. 36–43, Jan. 2012. doi: 10.1109/tap.2011.2167925

[92] N. AL-Fadhali, H. A. Majid, R. Omar, S. H. Dahlan, A. Y. I. Ashyap, S. M. Shah, M. K. A. Rahim, and B. A. F. Esmail, "Substrate integrated waveguide cavity backed frequency reconfigurable antenna for cognitive radio applies to internet of things applications," *International Journal of RF and Microwave Computer-Aided Engineering*, vol. 30, no. 1, Oct. 2019. doi: 10.1002/mmce.22020

[93] M. Al-Husseini, A. Ramadan, A. El-Hajj, K. Y. Kabalan, Y. Tawk, and C. G. Christodoulou, "Design based on complementary split-ring resonators of an

antenna with controllable band notches for UWB cognitive radio applications," in *2011 IEEE International Symposium on Antennas and Propagation (APSURSI)*, Jul. 2011. doi: 10.1109/aps.2011.5996479

[94] Y. Li, W. Li, and Q. Ye, "A reconfigurable triple-notch-band antenna integrated with defected microstrip structure band-stop filter for ultra-wideband cognitive radio applications," *International Journal of Antennas and Propagation*, vol. 2013, pp. 1–13, 2013. doi: 10.1155/2013/472645

[95] E. Erfani, J. Nourinia, C. Ghobadi, M. Niroo-Jazi, and T. A. Denidni, "Design and implementation of an integrated UWB/reconfigurable-slot antenna for cognitive radio applications," *IEEE Antennas and Wireless Propagation Letters*, vol. 11, pp. 77–80, 2012. doi: 10.1109/lawp.2011.2182631

[96] L. Ge and K. M. Luk, "Band-reconfigurable unidirectional antenna: A simple, efficient magneto-electric antenna for cognitive radio applications." *IEEE Antennas and Propagation Magazine*, vol. 58, no. 2, pp. 18–27, Apr. 2016. doi: 10.1109/map.2016.2520302

[97] E. Ebrahimi, J. R. Kelly, and P. S. Hall, "Integrated wide-narrowband antenna for multi-standard radio," *IEEE Transactions on Antennas and Propagation*, vol. 59, no. 7, pp. 2628–2635, Jul. 2011. doi: 10.1109/tap.2011.2152353

[98] M. Al-Husseini, A. El-Hajj, Y. Tawk, K. Y. Kabalan, and C. G. Christodoulou, "A simple dual-port antenna system for cognitive radio applications," in *2010 International Conference on High Performance Computing & Simulation*, Jun. 2010. doi: 10.1109/hpcs.2010.5547078

[99] Y. Cai, Y. J. Guo, and A. R. Weily, "A frequency-reconfigurable quasi-yagi dipole antenna," *IEEE Antennas and Wireless Propagation Letters*, vol. 9, pp. 883–886, 2010. doi: 10.1109/lawp.2010.2073436

[100] S. Riaz, X. Zhao, and S. Geng, "A frequency reconfigurable MIMO antenna with agile feedline for cognitive radio applications," *International Journal of*

RF and Microwave Computer-Aided Engineering, vol. 30, no. 3, Dec. 2019. doi: 10.1002/mmce.22100

[101] R. Hussain, A. Raza, M. U. Khan, A. Shammim, and M. S. Sharawi, "Miniaturized frequency reconfigurable pentagonal MIMO slot antenna for interweave CR applications," *International Journal of RF and Microwave Computer-Aided Engineering*, vol. 29, no. 9, Apr. 2019. doi: 10.1002/mmce.21811

[102] S. F. Jilani, A. Rahimian, Y. Alfadhl, and A. Alomainy, "Low-profile flexible frequency-reconfigurable millimetre-wave antenna for 5g applications," *Flexible and Printed Electronics*, vol. 3, no. 3, p. 035003, Aug. 2018. doi: 10.1088/2058-8585/aad392

[103] Y. Chen, L. Ye, J. Zhuo, Y. Liu, L. Zhang, M. Zhang, and Q. H. Liu, "Frequency reconfigurable circular patch antenna with an arc-shaped slot ground controlled by PIN diodes," *International Journal of Antennas and Propagation*, vol. 2017, pp. 1–7, 2017. doi: 10.1155/2017/7081978

[104] L. Pazin and Y. Leviatan, "Reconfigurable rotated-t slot antenna for cognitive radio systems," *IEEE Transactions on Antennas and Propagation*, vol. 62, no. 5, pp. 2382–2387, May 2014. doi: 10.1109/tap.2014.2308539

[105] Y. Cao, S. W. Cheung, X. L. Sun, and T. I. Yuk, "Frequency-reconfigurable monopole antenna with wide tuning range for cognitive radio," *Microwave and Optical Technology Letters*, vol. 56, no. 1, pp. 145–152, Nov. 2013. doi: 10.1002/mop.28070

[106] D. Peroulis, K. Sarabandi, and L. Katehi, "A planar VHF reconfigurable slot antenna," in *IEEE Antennas and Propagation Society International Symposium. 2001 Digest. Held in conjunction with: USNC/URSI National Radio Science Meeting (Cat. No.01CH37229)*, 2001. doi: 10.1109/aps.2001.958815

[107] G. Jin, C. Deng, J. Yang, Y. Xu, and S. Liao, "A new differentially-fed frequency reconfigurable antenna for WLAN and sub-6ghz 5g applications," *IEEE Access*, vol. 7, pp. 56 539–56 546, 2019. doi: 10.1109/access.2019.2901760

[108] R. Yadav and P. N. Patel, "EBG-inspired reconfigurable patch antenna for frequency diversity application," *AEU - International Journal of Electronics and Communications*, vol. 76, pp. 52–59, Jun. 2017. doi: 10.1016/j.aeue.2017.03.022

[109] B. P. Chacko, G. Augustin, and T. A. Denidni, "Electronically reconfigurable uniplanar antenna with polarization diversity for cognitive radio applications," *IEEE Antennas and Wireless Propagation Letters*, vol. 14, pp. 213–216, 2015. doi: 10.1109/lawp.2014.2360353

[110] H. Boudaghi, M. Azarmanesh, and M. Mehranpour, "A frequency-reconfigurable monopole antenna using switchable slotted ground structure," *IEEE Antennas and Wireless Propagation Letters*, vol. 11, pp. 655–658, 2012. doi: 10.1109/lawp.2012.2204030

[111] A. Mansoul, F. Ghanem, M. R. Hamid, and M. Trabelsi, "A selective frequency-reconfigurable antenna for cognitive radio applications," *IEEE Antennas and Wireless Propagation Letters*, vol. 13, pp. 515–518, 2014. doi: 10.1109/lawp.2014.2311114

[112] A. H. Ramadan, J. Costantine, M. Al-Husseini, K. Y. Kabalan, Y. Tawk, and C. G. Christodoulou, "Tunable filter-antennas for cognitive radio applications," *Progress In Electromagnetics Research B*, vol. 57, pp. 253–265, 2014. doi: 10.2528/pierb13112005

[113] I. H. Idris, M. R. Hamid, K. Kamardin, and M. K. A. Rahim, "A multi to wideband frequency reconfigurable antenna," *International Journal of RF and Microwave Computer-Aided Engineering*, vol. 28, no. 4, p. e21216, Dec. 2017. doi: 10.1002/mmce.21216

[114] K. Kandasamy, B. Majumder, J. Mukherjee, and K. Ray, "Design of SRR loaded reconfigurable antenna for UWB and narrow band applications," in *2015 IEEE International Symposium on Antennas and Propagation & USNC/URSI National Radio Science Meeting*, Jul. 2015. doi: 10.1109/aps.2015.7304984

[115] M. Al-Husseini, A. Ramadan, M. Zamudio, C. Christodoulou, A. El-Hajj, and K. Kabalan, "A UWB antenna combined with a reconfigurable band-pass filter for cognitive radio applications," in *2011 IEEE-APS Topical Conference on Antennas and Propagation in Wireless Communications*, Sep. 2011. doi: 10.1109/apwc.2011.6046813

[116] J. Deng, S. Hou, L. Zhao, and L. Guo, "A reconfigurable filtering antenna with integrated bandpass filters for UWB/WLAN applications," *IEEE Transactions on Antennas and Propagation*, vol. 66, no. 1, pp. 401–404, Jan. 2018. doi: 10.1109/tap.2017.2760363

[117] O. E. Maleky and F. B. Abdelouahab, "A UWB antenna with reconfigurable rejection band using split ring resonator for radio cognitive technology," *Procedia Manufacturing*, vol. 32, pp. 694–701, 2019. doi: 10.1016/j.promfg.2019.02.273

[118] M. R. Hamid, P. Gardner, P. S. Hall, and F. Ghanem, "Vivaldi antenna with integrated switchable band pass resonator," *IEEE Transactions on Antennas and Propagation*, vol. 59, no. 11, pp. 4008–4015, Nov. 2011. doi: 10.1109/tap.2011.2164197

[119] M. R. Hamid, P. Gardner, P. S. Hall, and F. Ghanem, "Reconfigurable vivaldi antenna," *Microwave and Optical Technology Letters*, vol. 52, no. 4, pp. 785–787, Feb. 2010. doi: 10.1002/mop.25030

[120] S. Koley, D. Bepari, and D. Mitra, "Band-reconfigurable monopole antenna for cognitive radio applications," *IETE Journal of Research*, vol. 61, no. 4, pp. 411–416, Mar. 2015. doi: 10.1080/03772063.2015.1024179

[121] M. Ikram, E. A. Abbas, N. Nguyen-Trong, K. H. Sayidmarie, and A. Abbosh, "Integrated frequency-reconfigurable slot antenna and connected slot antenna array for 4g and 5g mobile handsets," *IEEE Transactions on Antennas and Propagation*, vol. 67, no. 12, pp. 7225–7233, Dec. 2019. doi: 10.1109/tap.2019.2930119

[122] D. Anagnostou, M. Chryssomallis, J. Lyke, and C. Christodoulou, "Reconfigurable sierpinski gasket antenna using RF-MEMS switches," in *IEEE Antennas and Propagation Society International Symposium. Digest. Held in conjunction*

with: USNC/CNC/URSI North American Radio Sci. Meeting (Cat. No.03CH37450), 2003. doi: 10.1109/aps.2003.1217475

[123] D. Anagnostou, G. Zheng, M. Chryssomallis, J. Lyke, G. Ponchak, J. Papapolymerou, and C. Christodoulou, "Design, fabrication, and measurements of an RF-MEMS-based self-similar reconfigurable antenna," *IEEE Transactions on Antennas and Propagation*, vol. 54, no. 2, pp. 422–432, Feb. 2006. doi: 10.1109/tap.2005.863399

[124] C. Christodoulou, "RF-MEMS and its applications to microwave systems, antennas and wireless communications," in *Proceedings of the 2003 SBMO/IEEE MTT-S International Microwave and Optoelectronics Conference - IMOC 2003. (Cat. No.03TH8678)*, 2003. doi: 10.1109/imoc.2003.1244915

[125] R. Saha, S. Maity, and C. T. Bhunia, "Design and characterization of a tunable patch antenna loaded with capacitive MEMS switch using CSRRs structure on the patch," *Alexandria Engineering Journal*, vol. 55, no. 3, pp. 2621–2630, Sep. 2016. doi: 10.1016/j.aej.2016.05.002

[126] R. Simons, D. Chun, and L. Katehi, "Reconfigurable array antenna using microelectromechanical systems (MEMS) actuators," in *IEEE Antennas and Propagation Society International Symposium. 2001 Digest. Held in conjunction with: USNC/URSI National Radio Science Meeting (Cat. No.01CH37229)*, 2001. doi: 10.1109/aps.2001.960186

[127] J. Kiriazi, H. Ghali, H. Ragaie, and H. Haddara, "Reconfigurable dual-band dipole antenna on silicon using series MEMS switches," in *IEEE Antennas and Propagation Society International Symposium. Digest. Held in conjunction with: USNC/CNC/URSI North American Radio Sci. Meeting (Cat. No.03CH37450)*, 2003. doi: 10.1109/aps.2003.1217482

[128] M. D. Wright, W. Baron, J. Miller, J. Tuss, D. Zeppettella, and M. Ali, "MEMS reconfigurable broadband patch antenna for conformal applications," *IEEE Transactions on Antennas and Propagation*, vol. 66, no. 6, pp. 2770–2778, Jun. 2018. doi: 10.1109/tap.2018.2819818

[129] T. Wu, R. L. Li, S. Y. Eom, S. S. Myoung, K. Lim, J. Laskar, S. I. Jeon, and M. M. Tentzeris, "Switchable quad-band antennas for cognitive radio base station applications," *IEEE Transactions on Antennas and Propagation*, vol. 58, no. 5, pp. 1468–1476, May 2010. doi: 10.1109/tap.2010.2044472

[130] V. Reji and C. T. Manimegalai, "Light controlled frequency reconfigurable antenna for wireless applications," *International Journal of Microwave and Wireless Technologies*, pp. 1–7, Feb. 2022. doi: 10.1017/s1759078722000137

[131] A. Daryoush, K. Bontzos, and P. Herczfeld, "Optically tuned patch antenna for phased array applications," in *1986 Antennas and Propagation Society International Symposium*, 1986. doi: 10.1109/aps.1986.1149762

[132] Y. Tawk, A. R. Albrecht, S. Hemmady, G. Balakrishnan, and C. G. Christodoulou, "Optically pumped reconfigurable antenna systems (OPRAS)," in *2010 IEEE Antennas and Propagation Society International Symposium*, Jul. 2010. doi: 10.1109/aps.2010.5560910

[133] D. Zhao, L. Lan, Y. Han, F. Liang, Q. Zhang, and B.-Z. Wang, "Optically controlled reconfigurable band-notched UWB antenna for cognitive radio applications," *IEEE Photonics Technology Letters*, vol. 26, no. 21, pp. 2173–2176, Nov. 2014. doi: 10.1109/lpt.2014.2349961

[134] I. Carrasquillo-Rivera, Z. Popovic, and R. Solis, "Tunable slot antenna using varactors and photodiodes," in *IEEE Antennas and Propagation Society International Symposium. Digest. Held in conjunction with: USNC/CNC/URSI North American Radio Sci. Meeting (Cat. No.03CH37450)*, 2003. doi: 10.1109/aps.2003.1220327

[135] Y. Tawk, S. Hemmady, C. G. Christodoulou, J. Costantine, and G. Balakrishnan, "A cognitive radio antenna design based on optically pumped reconfigurable antenna system (OPRAS)," in *2011 IEEE International Symposium on Antennas and Propagation (APSURSI)*, Jul. 2011. doi: 10.1109/aps.2011.5996478

[136] A. H. Kazemi and A. Mokhtari, "Graphene-based patch antenna tunable in the three atmospheric windows," *Optik*, vol. 142, pp. 475–482, Aug. 2017. doi: 10.1016/j.ijleo.2017.05.113

[137] S. Prakash, S. Dash, and A. Patnaik, "Reconfigurable circular patch THz antenna using graphene stack based SIW technique," in *2018 IEEE Indian Conference on Antennas and Propogation (InCAP)*, Dec. 2018. doi: 10.1109/incap.2018.8770855

[138] S. Dash and A. Patnaik, "Dual band reconfigurable plasmonic antenna using bilayer graphene," in *2017 IEEE International Symposium on Antennas and Propagation & USNC/URSI National Radio Science Meeting*, Jul. 2017. doi: 10.1109/apusncursinrsm.2017.8072503

[139] G. S. Sethi, A. Srivastava, C.-Y. Chiu, V. Chigrinov, and R. D. Murch, "Design of a transparent LC based reconfigurable antenna," in *2016 Asia-Pacific Microwave Conference (APMC)*, Dec. 2016. doi: 10.1109/apmc.2016.7931422

[140] S. Dash and A. Patnaik, "Graphene loaded frequency reconfigurable metal antenna," in *2017 IEEE International Conference on Antenna Innovations & Modern Technologies for Ground, Aircraft and Satellite Applications (iAIM)*, Nov. 2017. doi: 10.1109/iaim.2017.8402579

[141] Y. Tawk, J. Costantine, K. Avery, and C. G. Christodoulou, "Implementation of a cognitive radio front-end using rotatable controlled reconfigurable antennas," *IEEE Transactions on Antennas and Propagation*, vol. 59, no. 5, pp. 1773–1778, May 2011. doi: 10.1109/tap.2011.2122239

[142] P. Tummas, P. Krachodnok, and R. Wongsan, "A frequency reconfigurable antenna design for UWB applications," in *2014 11th International Conference on Electrical Engineering/Electronics, Computer, Telecommunications and Information Technology (ECTI-CON)*, May 2014. doi: 10.1109/ecticon.2014.6839850

[143] Y. Tawk and C. Christodoulou, "A new reconfigurable antenna design for cognitive radio," *IEEE Antennas and Wireless Propagation Letters*, vol. 8, pp. 1378–1381, 2009. doi: 10.1109/lawp.2009.2039461

[144] M. M. A. Kumar, A. Patnaik, and C. G. Christodoulou, "Design and testing of a multifrequency antenna with a reconfigurable feed," *IEEE Antennas and Wireless Propagation Letters*, vol. 13, pp. 730–733, 2014. doi: 10.1109/lawp.2014.2315433

[145] J. Costantine, Y. Tawk, J. Woodland, N. Flaum, and C. G. Christodoulou, "Reconfigurable antenna system with a movable ground plane for cognitive radio," *IET Microwaves, Antennas & Propagation*, vol. 8, no. 11, pp. 858–863, Aug. 2014. doi: 10.1049/iet-map.2013.0605

[146] M. Zhu and L. Sun, "Design of frequency reconfigurable antenna based on metasurface," in *2017 IEEE 2nd Advanced Information Technology, Electronic and Automation Control Conference (IAEAC)*, Mar. 2017. doi: 10.1109/iaeac.2017.8054320

[147] B. Majumder, K. Kandasamy, J. Mukherjee, and K. Ray, "Dual band dual polarized frequency reconfigurable antenna using meta-surface," in *2015 Asia-Pacific Microwave Conference (APMC)*, Dec. 2015. doi: 10.1109/apmc.2015.7411790

[148] B. Majumder, K. Krishnamoorthy, J. Mukherjee, and K. P. Ray, "Frequency-reconfigurable slot antenna enabled by thin anisotropic double layer metasurfaces," *IEEE Transactions on Antennas and Propagation*, vol. 64, no. 4, pp. 1218–1225, Apr. 2016. doi: 10.1109/tap.2016.2526081

[149] J. Costantine, Y. Tawk, and C. G. Christodoulou, "Reconfigurable deployable antennas for space communications," in *2014 International Workshop on Antenna Technology: Small Antennas, Novel EM Structures and Materials, and Applications (iWAT)*, Mar. 2014. doi: 10.1109/iwat.2014.6958623

[150] G. Augustin and T. A. Denidni, "An integrated ultra wideband/narrow band antenna in uniplanar configuration for cognitive radio systems," *IEEE Transactions on Antennas and Propagation*, vol. 60, no. 11, pp. 5479–5484, Nov. 2012. doi: 10.1109/tap.2012.2207688

[151] Y. Li, W. Li, and R. Mittra, "Integrated dual-purpose narrow/ultra-wide band antenna for cognitive radio applications," in *Proceedings of the 2012*

IEEE International Symposium on Antennas and Propagation, Jul. 2012. doi: 10.1109/aps.2012.6348870

[152] O. Yeonjeong, Y. Jin, and J. Choi, "A compact four-port coplanar antenna based on an excitation switching reconfigurable mechanism for cognitive radio applications," *Applied Sciences*, vol. 9, no. 15, p. 3157, Aug. 2019. doi: 10.3390/app9153157

[153] S. B. Fischer, S. Wang, J. Hesselbarth, and J. N. Burghartz, "Flexible and adaptive dipole-based triple-fed antenna for single-chip transceiver," in *2022 16th European Conference on Antennas and Propagation (EuCAP)*, Mar. 2022. doi: 10.23919/eucap53622.2022.9769337

[154] T. Aboufoul, C. Parini, X. Chen, and A. Alomainy, "Pattern-reconfigurable planar circular ultra-wideband monopole antenna," *IEEE Transactions on Antennas and Propagation*, vol. 61, no. 10, pp. 4973–4980, Oct. 2013. doi: 10.1109/tap.2013.2274262

[155] K. Li, Y.-M. Cai, Y. Yin, and W. Hu, "A wideband e-plane pattern reconfigurable antenna with enhanced gain," *International Journal of RF and Microwave Computer-Aided Engineering*, vol. 29, no. 2, p. e21530, Nov. 2018. doi: 10.1002/mmce.21530

[156] J. K. Ji, "Dual-band pattern reconfigurable antenna for wireless MIMO applications," *ICT Express*, vol. 2, no. 4, pp. 199–203, Dec. 2016. doi: 10.1016/j.icte.2016.08.002

[157] A. Mak, C. Rowell, and R. Murch, "Low cost reconfigurable landstorfer planar antenna array," *IEEE Transactions on Antennas and Propagation*, vol. 57, no. 10, pp. 3051–3061, Oct. 2009. doi: 10.1109/tap.2009.2028593

[158] S. Shamsinejad, N. Khalid, F. M. Monavar, S. Shamsadini, R. Mirzavand, G. Moradi, and P. Mousavi, "Pattern reconfigurable cubic slot antenna," *IEEE Access*, vol. 7, pp. 64 401–64 410, 2019. doi: 10.1109/access.2019.2917145

[159] G. A. R. Arroyave, A. Barlabé, L. Pradell, J. L. A. Quijano, B. A. Cetiner, and L. Jofre-Roca, "Design of minimum nonlinear distortion reconfigurable antennas

for next-generation communication systems," *Sensors*, vol. 21, no. 7, p. 2557, Apr. 2021. doi: 10.3390/s21072557

[160] K. J. Vinoy, K. A. Jose, V. K. Varadan, and V. V. Varadan, "Hilbert curve fractal antennas with reconfigurable characteristics," in *2001 IEEE MTT-S International Microwave Sympsoium Digest (Cat. No.01CH37157)*, 2001. doi: 10.1109/mwsym.2001.966911

[161] D. Sievenpiper, J. Schaffner, R. Loo, and G. Tangonan, "Reconfigurable antennas based on electrically tunable impedance surfaces," in *31st European Microwave Conference, 2001*, Oct. 2001. doi: 10.1109/euma.2001.339032

[162] K. Krishnamoorthy, B. Majumder, J. Mukherjee, and K. P. Ray, "Reconfigurable zeroth order and half wave length resonator antenna for pattern reconfiguration using tunable EBG structures," in *2014 16th International Symposium on Antenna Technology and Applied Electromagnetics (ANTEM)*, Jul. 2014. doi: 10.1109/antem.2014.6887748

[163] G. Huff and J. Bernhard, "Integration of packaged RF MEMS switches with radiation pattern reconfigurable square spiral microstrip antennas," *IEEE Transactions on Antennas and Propagation*, vol. 54, no. 2, pp. 464–469, Feb. 2006. doi: 10.1109/tap.2005.863409

[164] H. Lago, Z. Zakaria, M. F. Jamlos, and P. J. Soh, "A wideband reconfigurable folded planar dipole using MEMS and hybrid polymeric substrates," *AEU - International Journal of Electronics and Communications*, vol. 99, pp. 347–353, Feb. 2019. doi: 10.1016/j.aeue.2018.12.011

[165] M. J. Chashmi, P. Rezaei, and N. Kiani, "Reconfigurable graphene-based v-shaped dipole antenna: From quasi-isotropic to directional radiation pattern," *Optik*, vol. 184, pp. 421–427, May 2019. doi: 10.1016/j.ijleo.2019.04.125

[166] P. K. Li, C. J. You, H. F. Yu, and Y. J. Cheng, "Mechanically pattern reconfigurable dual-band antenna with omnidirectional/directional pattern for 2.4/5ghz

WLAN application," *Microwave and Optical Technology Letters*, vol. 59, no. 10, pp. 2526–2531, Jul. 2017. doi: 10.1002/mop.30778

[167] D. Sievenpiper, J. Schaffner, R. Loo, G. Tangonan, S. Ontiveros, and R. Harold, "A tunable impedance surface performing as a reconfigurable beam steering reflector," *IEEE Transactions on Antennas and Propagation*, vol. 50, no. 3, pp. 384–390, Mar. 2002. doi: 10.1109/8.999631

[168] C.-C. Chen, C.-Y.-D. Sim, and H.-L. Lin, "Annular ring slot antenna design with reconfigurable polarization," *International Journal of RF and Microwave Computer-Aided Engineering*, vol. 26, no. 2, pp. 110–120, Oct. 2015. doi: 10.1002/mmce.20944

[169] M. Fries, M. Grani, and R. Vahldieck, "A reconfigurable slot antenna with switch-able polarization," *IEEE Microwave and Wireless Components Letters*, vol. 13, no. 11, pp. 490–492, Nov. 2003. doi: 10.1109/lmwc.2003.817148

[170] H. H. Tran and H. C. Park, "Wideband polarization reconfigurable circularly polarized antenna with omnidirectional radiation pattern," *International Journal of RF and Microwave Computer-Aided Engineering*, vol. 29, no. 6, p. e21708, Mar. 2019. doi: 10.1002/mmce.21708

[171] Q. Chen, J.-Y. Li, G. Yang, B. Cao, and Z. Zhang, "A polarization-reconfigurable high-gain microstrip antenna," *IEEE Transactions on Antennas and Propagation*, vol. 67, no. 5, pp. 3461–3466, May 2019. doi: 10.1109/tap.2019.2902750

[172] Y. Sung, "Dual-band reconfigurable antenna for polarization diversity," *International Journal of Antennas and Propagation*, vol. 2018, pp. 1–7, 2018. doi: 10.1155/2018/6878607

[173] Y. Al-Yasir, A. Abdullah, N. O. Parchin, R. Abd-Alhameed, and J. Noras, "A new polarization-reconfigurable antenna for 5g applications," *Electronics*, vol. 7, no. 11, p. 293, Nov. 2018. doi: 10.3390/electronics7110293

[174] P. Kumar, S. Dwari, R. K. Saini, and M. K. Mandal, "Dual-band dual-sense polarization reconfigurable circularly polarized antenna," *IEEE Antennas and Wireless Propagation Letters*, vol. 18, no. 1, pp. 64–68, Jan. 2019. doi: 10.1109/lawp.2018.2880799

[175] K. Krishnamoorthy, B. Majumder, J. Mukherjee, and K. P. Ray, "A circular polarization reconfigurable antenna based on reconfigurable electromagnetic band-gap structures," in *2014 8th International Congress on Advanced Electromagnetic Materials in Microwaves and Optics*, Aug. 2014. doi: 10.1109/metamaterials.2014.6948628

[176] Z. Wu, H. Liu, and L. Li, "Metasurface-inspired low profile polarization reconfigurable antenna with simple DC controlling circuit," *IEEE Access*, vol. 7, pp. 45 073–45 079, 2019. doi: 10.1109/access.2019.2908928

[177] A. Bhattacharjee, S. Dwari, and M. K. Mandal, "Polarization-reconfigurable compact monopole antenna with wide effective bandwidth," *IEEE Antennas and Wireless Propagation Letters*, vol. 18, no. 5, pp. 1041–1045, May 2019. doi: 10.1109/lawp.2019.2908661

[178] R. Simons, D. Chun, and L. Katehi, "Polarization reconfigurable patch antenna using microelectromechanical systems (MEMS) actuators," in *IEEE Antennas and Propagation Society International Symposium (IEEE Cat. No.02CH37313)*, 2002. doi: 10.1109/aps.2002.1016015

[179] T. Aboufoul, A. Alomainy, and C. Parini, "Polarization reconfigurable ultrawideband antenna for cognitive radio applications," *Microwave and Optical Technology Letters*, vol. 55, no. 3, pp. 501–506, Jan. 2013. doi: 10.1002/mop.27353

[180] B. Anantha, L. Merugu, and P. S. Rao, "A novel single feed frequency and polarization reconfigurable microstrip patch antenna," *AEU - International Journal of Electronics and Communications*, vol. 72, pp. 8–16, Feb. 2017. doi: 10.1016/j.aeue.2016.11.012

[181] A. Bharathi, M. Lakshminarayana, and P. S. Rao, "A quad-polarization and frequency reconfigurable square ring slot loaded microstrip patch antenna for WLAN applications," *AEU - International Journal of Electronics and Communications*, vol. 78, pp. 15–23, Aug. 2017. doi: 10.1016/j.aeue.2017.05.015

[182] F. Yang and Y. Rahmat-Samii, "Patch antenna with switchable slots (PASS): reconfigurable design for wireless communications," in *IEEE Antennas and Propagation Society International Symposium (IEEE Cat. No.02CH37313)*, 2002. doi: 10.1109/aps.2002.1016384

[183] R. Hussain and M. S. Sharawi, "A cognitive radio reconfigurable MIMO and sensing antenna system," *IEEE Antennas and Wireless Propagation Letters*, vol. 14, pp. 257–260, 2015. doi: 10.1109/lawp.2014.2361450

[184] S. Nikolaou, R. Bairavasubramanian, C. Lugo, I. Carrasquillo, D. Thompson, G. Ponchak, J. Papapolymerou, and M. Tentzeris, "Pattern and frequency reconfigurable annular slot antenna using PIN diodes," *IEEE Transactions on Antennas and Propagation*, vol. 54, no. 2, pp. 439–448, Feb. 2006. doi: 10.1109/tap.2005.863398

[185] Y. P. Selvam, M. Kanagasabai, M. G. N. Alsath, S. Velan, S. Kingsly, S. Subbaraj, Y. V. R. Rao, R. Srinivasan, A. K. Varadhan, and M. Karuppiah, "A low-profile frequency- and pattern-reconfigurable antenna," *IEEE Antennas and Wireless Propagation Letters*, vol. 16, pp. 3047–3050, 2017. doi: 10.1109/lawp.2017.2759960

[186] D. Rodrigo and L. Jofre, "Frequency and radiation pattern reconfigurability of a multi-size pixel antenna," *IEEE Transactions on Antennas and Propagation*, vol. 60, no. 5, pp. 2219–2225, May 2012. doi: 10.1109/tap.2012.2189739

[187] J.-C. Langer, J. Zou, C. Liu, and J. Bernhard, "Micromachined reconfigurable out-of-plane microstrip patch antenna using plastic deformation magnetic actuation," *IEEE Microwave and Wireless Components Letters*, vol. 13, no. 3, pp. 120–122, Mar. 2003. doi: 10.1109/lmwc.2003.810123

[188] Y. P. Selvam, M. G. N. Alsath, M. Kanagasabai, L. Elumalai, S. K. Palaniswamy, S. Subbaraj, S. Kingsly, G. Konganathan, and I. Kulandhaisamy, "A patch-slot antenna array with compound reconfiguration," *IEEE Antennas and Wireless Propagation Letters*, vol. 17, no. 3, pp. 525–528, Mar. 2018. doi: 10.1109/lawp.2018.2801124

[189] L. Ge, Y. Li, J. Wang, and C.-Y.-D. Sim, "A low-profile reconfigurable cavity-backed slot antenna with frequency, polarization, and radiation pattern agility," *IEEE Transactions on Antennas and Propagation*, vol. 65, no. 5, pp. 2182–2189, May 2017. doi: 10.1109/tap.2017.2681432

[190] S. Sharma, C. C. Tripathi, and R. Rishi, "A versatile reconfigurable antenna with integrated sensing mechanism," *International Journal of Microwave and Wireless Technologies*, vol. 10, no. 4, pp. 469–478, Dec. 2017. doi: 10.1017/s1759078717001441

[191] D. Rodrigo, B. A. Cetiner, and L. Jofre, "Frequency, radiation pattern and polarization reconfigurable antenna using a parasitic pixel layer," *IEEE Transactions on Antennas and Propagation*, vol. 62, no. 6, pp. 3422–3427, Jun. 2014. doi: 10.1109/tap.2014.2314464

[192] K. Ogawa, T. Takahashi, Y. Koyanagi, and K. Ito, "Automatic impedance matching of an active helical antenna near a human operator," in *33rd European Microwave Conference, 2003*, Oct. 2003. doi: 10.1109/euma.2003.340850

[193] J. deMingo, A. Valdovinos, A. Crespo, D. Navarro, and P. Garcia, "An RF electronically controlled impedance tuning network design and its application to an antenna input impedance automatic matching system," *IEEE Transactions on Microwave Theory and Techniques*, vol. 52, no. 2, pp. 489–497, Feb. 2004. doi: 10.1109/tmtt.2003.821909

[194] L. Huang, "Theoretical and experimental investigation of adaptive antenna impedance matching for multiband mobile phone applications," in *Wideband and Multi-Band Antennas and Arrays*, 2005. doi: 10.1049/ic:20050280

[195] D. Qiao, Y. Zhao, T. Hung, D. Kimball, M. Li, P. Asbeck, D. Choi, and D. Kelly, "Antenna impedance mismatch measurement and correction for adaptive CDMA transceivers," in *IEEE MTT-S International Microwave Symposium Digest, 2005.*, 2005. doi: 10.1109/mwsym.2005.1516730

[196] B. Hur, W. R. Eisenstadt, and K. L. Melde, "Testing and validation of adaptive impedance matching system for broadband antenna," *Electronics*, vol. 8, no. 9, p. 1055, Sep. 2019. doi: 10.3390/electronics8091055

[197] R. Whatley, Z. Zhou, and K. Melde, "Reconfigurable RF impedance tuner for match control in broadband wireless devices," *IEEE Transactions on Antennas and Propagation*, vol. 54, no. 2, pp. 470–478, Feb. 2006. doi: 10.1109/tap.2005.863396

[198] D. Weile and E. Michielssen, "Genetic algorithm optimization applied to electromagnetics: a review," *IEEE Transactions on Antennas and Propagation*, vol. 45, no. 3, pp. 343–353, Mar. 1997. doi: 10.1109/8.558650

[199] L. Pringle, P. Harms, S. Blalock, G. Kiesel, E. Kuster, P. Friederich, R. Prado, J. Morris, and G. Smith, "A reconfigurable aperture antenna based on switched links between electrically small metallic patches," *IEEE Transactions on Antennas and Propagation*, vol. 52, no. 6, pp. 1434–1445, Jun. 2004. doi: 10.1109/tap.2004.825648

[200] S. Soltani, P. Lotfi, and R. D. Murch, "Design and optimization of multiport pixel antennas," *IEEE Transactions on Antennas and Propagation*, vol. 66, no. 4, pp. 2049–2054, Apr. 2018. doi: 10.1109/tap.2018.2800759

[201] P. Lotfi, S. Soltani, and R. D. Murch, "Printed endfire beam-steerable pixel antenna," *IEEE Transactions on Antennas and Propagation*, vol. 65, no. 8, pp. 3913–3923, Aug. 2017. doi: 10.1109/tap.2017.2716399

[202] F. Jiang, C.-Y. Chiu, S. Shen, Q. S. Cheng, and R. Murch, "Pixel antenna optimization using n -port characteristic mode analysis," *IEEE Transactions on Antennas and Propagation*, vol. 68, no. 5, pp. 3336–3347, May 2020. doi: 10.1109/tap.2019.2963588

[203] F. Jiang, S. Shen, C.-Y. Chiu, Z. Zhang, Y. Zhang, Q. S. Cheng, and R. Murch, "Pixel antenna optimization based on perturbation sensitivity analysis," *IEEE Transactions on Antennas and Propagation*, vol. 70, no. 1, pp. 472–486, Jan. 2022. doi: 10.1109/tap.2021.3097104

[204] J. L. A. Quijano and G. Vecchi, "Optimization of an innovative type of compact frequency-reconfigurable antenna," *IEEE Transactions on Antennas and Propagation*, vol. 57, no. 1, pp. 9–18, Jan. 2009. doi: 10.1109/tap.2008.2009649

[205] C. Wu, Z. Yang, Y. Li, Y. Zhang, and Y. Yashchyshyn, "Methodology to reduce the number of switches in frequency reconfigurable antennas with massive switches," *IEEE Access*, vol. 6, pp. 12 187–12 196, 2018. doi: 10.1109/access.2018.2812139

[206] S. Song and R. D. Murch, "An efficient approach for optimizing frequency reconfigurable pixel antennas using genetic algorithms," *IEEE Transactions on Antennas and Propagation*, vol. 62, no. 2, pp. 609–620, Feb. 2014. doi: 10.1109/tap.2013.2293509

[207] K. Li, C. Cheng, T. Matsui, and M. Izutsu, "Coplanar patch antennas: principle, simulation and experiment," in *IEEE Antennas and Propagation Society International Symposium. 2001 Digest. Held in conjunction with: USNC/URSI National Radio Science Meeting (Cat. No.01CH37229)*. doi: 10.1109/aps.2001.960119

[208] D. Pozar, *Microwave Engineering*, 4th ed.   New York: Wiley, 2011, ch. 2, pp. 48–51.

[209] Y. Sun and J. Fidler, "Determination of the impedance matching domain of passive LC ladder networks: Theory and implementation," *Journal of the Franklin Institute*, vol. 333, no. 2, pp. 141–155, Mar. 1996. doi: 10.1016/0016-0032(96)00023-3

[210] S. B. Fischer, S. Özbek, S. Wang, M. Grözing, J. Hesselbarth, M. Berroth, and J. N. Burghartz, "Adaptive triple-fed antenna and thinned rf-chip integration into ultra thin flexible polymer foil," *International Journal of Microwave and Wireless Technologies*, p. 1–8, 2023. doi: 10.1017/S1759078723000818

[211] M. Rasteh and J. Hesselbarth, "Dipole antenna with multiple feeds adapting to the environment," in *2018 IEEE Asia-Pacific Conference on Antennas and Propagation (APCAP)*, Aug. 2018. doi: 10.1109/apcap.2018.8538060

[212] R. King, "Asymmetrically driven antennas and the sleeve dipole," *Proceedings of the IRE*, vol. 38, no. 10, pp. 1154–1164, Oct. 1950. doi: 10.1109/jrproc.1950.233110

[213] S. Özbek, J. Digel, M. Grozing, M. Berroth, G. Alavi, and J. N. Burghartz, "3-path 5-6 GHz 0.25 um SiGe BiCMOS power amplifier on thin substrate," in *2017 13th Conference on Ph.D. Research in Microelectronics and Electronics (PRIME)*, Jun. 2017. doi: 10.1109/prime.2017.7974104

[214] G. Alavi, S. Özbek, M. Rasteh, M. Grözing, M. Berroth, J. Hesselbarth, and J. N.Burghartz, "Embedding and interconnecting of ultra-thin RF chip in combination with flexible wireless hub in polymer foil," in *2018 7th Electronic System-Integration Technology Conference (ESTC)*, Sep. 2018. doi: 10.1109/estc.2018.8546462

[215] S. Özbek, M. Grözing, G. Alavi, J. N. Burghartz, and M. Berroth, "Three-path SiGe BiCMOS LNA on thinned silicon substrate for IoT applications," in *2018 48th European Microwave Conference (EuMC)*, Sep. 2018. doi: 10.23919/eumc.2018.8541760

[216] G. Alavi, S. Özbek, M. Rasteh, M. Grözing, M. Berroth, J. Hesselbarth, and J. N. Burghartz, "Toward a flexible and adaptive wireless hub by embedding power amplifier thinned silicon chip and antenna in a polymer foil," *International Journal of Microwave and Wireless Technologies*, vol. 11, no. 9, pp. 864–871, May 2019. doi: 10.1017/s1759078719000539

[217] S. Özbek, S. Wang, S. B. Fischer, M. Grözing, J. N. Burghartz, J. Hesselbarth, and M. Berroth, "Integrating ultra-thin sige bicmos power amplifier chip in combination with flexible antenna in the polymer foil," in *2022 IEEE International Symposium on Circuits and Systems (ISCAS)*, pp. 1–5.

[218] S. B. Fischer and J. Hesselbarth, "Off-centre fed dipole suppressing the radiation of the feed-line by a load impedance at an arbitrary point," in *2021 15th European*

Conference on Antennas and Propagation (EuCAP), Mar. 2021. doi: 10.23919/eu-cap51087.2021.9411303

[219] S. Özbek, S. B. Fischer, S. Wang, M. Berroth, J. Hesselbarth, and J. Burghartz, "Flexible image sensor with adaptive high-speed wireless connectivity," Inst. of Elect. and Opt. Commun. Eng. (INT) and Inst. of Radio Freq. Technol. (IHF) and Inst. of Nano- and Microelectron. Syst. (INES), Dresden, Germany, research report, presentation, Oct. 2019.

[220] S. B. Fischer-Kennedy and J. Hesselbarth, "Generalized approach to antenna reconfigurability by switching load admittances," *Progress In Electromagnetics Research B*, vol. 102, pp. 151–169, 2023. doi: 10.2528/PIERB23071004

[221] M. Jeeninga, A. J. van der Schaft, and C. D. Persis, "Graph theoretic formulae for the determinant and adjugate of matrices carrying graph structure," *IFAC-PapersOnLine*, vol. 51, no. 23, pp. 259–264, 2018. doi: 10.1016/j.ifacol.2018.12.045

Curriculum Vitae

- Born in 1991 in Buchholz in Nordheide, Germany.

- 1998-2011: Attending and graduating from Rudolf-Steiner-School, Villingen-Schwenningen, Germany with the Abitur.

- 2011-2013: Apprenticeship as nautical officer assistant at Hapag-Lloyd AG.

- 2013-2016: Bachelor of Science in electrical engineering and information technology with focus on communication systems and digital signal processing at the University of Stuttgart, Stuttgart, Germany.

- 2016-2018: Master of Science in electrical engineering and information technology with focus on information and communication technology at the University of Stuttgart, Stuttgart, Germany.

- Dec. 2018 - Aug. 2022: Research associate and PhD student at the institute of Radio Frequency Technology, University of Stuttgart, Stuttgart, Germany.

- Sep. 2022 - present: Research engineer at Robert Bosch GmbH
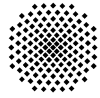
Eigenständigkeitserklärung

Ich versichere, dass ich die vorliegende Arbeit mit dem Titel:

„Antennas With Adaptively Varying Impedance Matching "

selbstständig verfasst und keine anderen als die angegebenen Quellen und Hilfsmittel benutzt habe. Aus fremden Quellen entnommene Passagen und Gedanken sind als solche kenntlich gemacht. Diese Dissertation wurde zu keiner Zeit in derselben oder substantiell ähnlichen Version bei einem anderen Prüfungsamt eingereicht.

Declaration of Authorship

I, hereby certify that the dissertation entitled:

„Antennas With Adaptively Varying Impedance Matching "

is entirely my own work except where indicated otherwise. Passages and ideas from other sources have been clearly indicated. This thesis has never been submitted in the same or substantially similar version to any other examination office.

Serafin Fischer-Kennedy, Stuttgart, 13 November 2023